Abstract

Recent developments in spatial atom interferometry have stimulated new fields in atomic physics and quantum optics, opening up new areas in fundamental research. Moreover, there are ideas for many practical applications for atom interferometry, such as highly sensitive, miniaturized, rotations sensors, accelerometers, and gravitational detectors, based on the Sagnac effect. The small de Broglie wavelength of atoms may improve the sensitivity of atom interferometers by several orders of magnitude compared with optical interferometers. Similar to quantum electronics where electrons are manipulated inside semiconductor structures, in atom optics, atoms may be made to move inside waveguide structures and are manipulated using potentials where at least one dimension is comparable to the de-Broglie wavelength of the atoms. With the use of guided atoms, miniaturized setups for matter wave interferometry with increased stability, large beam separation, and large enclosed areas become possible. The combination of well-established tools for atom cooling and manipulation with state-of-the-art microfabrication technology has led to the development of the atom chip, a micro fabricated, integrated devices in which electric, magnetic and optical fields can confine, control and manipulate cold atoms.

In this work we present a theoretical model for a Sagnac interferometer. The model relies on the analogy between a massive particle travelling in a rotating frame and a charged particle travelling in a ring with a magnetic flux, where atom-atom interactions and impurities in the system have been neglected. The scattering matrix formalism is used to predict the transmission and the sensitivity of revolving atom interferometer, based on double Y beamsplitters. The affect of temperature is analyzed to show that the sensitivity is improved with decreasing momentum bandwidth (an incident particles flux which is partially coherent, with spectral width Δ_k, may be viewed as a statistical mixture of wavepackets), i.e. the the sensitivity improves with decreasing temperature. As the required temperature for a narrow momentum bandwidth is much lower than an experimentally feasible temperature, this work focuses on the large spectral width regime which is experimentally feasible.

In addition to varying temperatures, we also analyze the effect of different finesse regimes. For example, we show that in the low finesse limit, where the particle has a small prob-

ability to complete many cycles inside the interferometer and therefore the accumulated Sagnac phase difference between counterpropagating trajectories is also small, the predicted sensitivity for rotations is lower compared to the high finesse regime. In the latter regime the particle has a high probability to complete many cycles inside the interferometer and therefore the accumulated Sagnac phase difference is large. Relying on these results we obtain the main result of the thesis - an expression for the sensitivity as a function of the finesse. Finally, the sensitivity of interferometers based on semi-X beamsplitters (one of the ports functions as a mirror), is also analyzed. Such a configuration may be experimentally easier to realize relative to the Y beam splitter.

For the double Y interferometer in the low finesse regime, we found the maximal sensitivity to be $\Delta\,\Omega_{max} \approx 10^{-10}\,\frac{rad}{sec}/\sqrt{Hz}$. This sensitivity is of the same order of magnitude as that achieved by present day low finesse freely propagating atom interferometers. For the double Y interferometer in the high finesse regime, we found the maximal sensitivity to be $\Delta\,\Omega_{max} \approx 10^{-12}\,\frac{rad}{sec}/\sqrt{Hz}$. This result is better by two orders of magnitude than any realized rotation sensor, in particular low finesse atom interferometers, and may therefore motivate additional work for the realization of multipass (high finesse) interferometers.

Contents

1. INTRODUCTION

An Interferometer is a physical device that splits single particles or their complementary waves into two different paths, which are then recombined, not before each path accumulates a phase related to the effective length of its trajectory and an optional phase added during the splitting and recombination. A phase difference of an integer product of 2π means constructive interference, where the intensity of the resultant interferometer output beam is higher than the sum of the intensities in the two paths. A phase difference of $(2n+1)\pi$ means destructive interference, where the intensity of the resultant beam is less than the sum of the two intensities. For any other phase difference the intensity is in between these limits.

The wide variety of internal degrees of freedom of an atom opens up new possibilities for interferometry which do not exist in the more traditional types of interferometry using photons, electrons and neutrons. In addition, the large atomic mass gives rise to high sensitivity concerning measures of rotation, acceleration and gravitation. In recent years, several groups reported work on atom interferometers where the atoms freely propagate between the interferometer components (beam splitters) [1]-[5]. Recently, Ketterle and his group [6] realized a trapped atom interferometer where the trapped atoms were coherently split by deforming an optical single-well potential into a double-well potential. Furthermore, Schmiedmayer and his group [7] realized a trapped atom interferometer on a chip, based on a combination of static and radio-frequency magnetic fields. These scientific achievements are in fact making the first steps toward guided atom interferometry, where the motion of the atoms in the interferometer arms will be fully controlled, similar to light interferometers based on optical fibers. Furthermore, multi-pass guided path allows to diminish the size of the interferometer down to micro-meter scale without reducing its sensitivity, as the phase difference between the ports of the interferometer accumulates due to the multi-pass trajectory instead of the large area of the interferometer.

The Sagnac effect is a phase shift which accumulates along the arms of a revolving closed loop

interferometer [8], the shift being directly proportional to the angular velocity of rotation, the area enclosed by the interferometer, and the wave frequency.

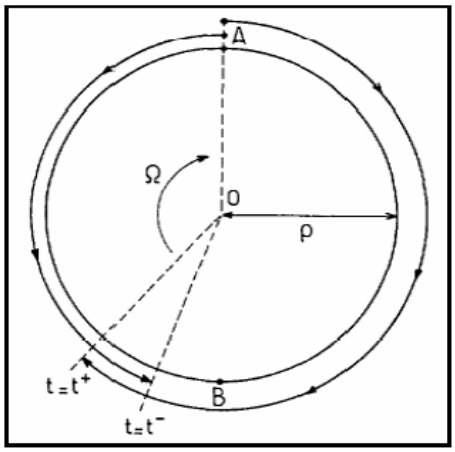

FIG. 1: Rotating circular interferometer. The beam-splitter starts from the point A at time $t = 0$, and rotates at angular frequency Ω. The two waves circulate in opposite senses and reach the Point B at different times t^+ and t^- (represented by the dashed lines). Taken from Ref. [10]

Let us consider the Sagnac effect in a general form, that is for arbitrary waves with phase velocity v_{ph} that propagate in a ring shaped interferometer, as shown in Fig.(1). A wave that enters the interferometer at point A splits into a wave that propagates clockwise and a wave that propagates counter clockwise. In the case where the interferometer does not revolve, the waves arrive at point B in a time

$$\tau = \frac{\pi\rho}{v_{ph}} \ , \tag{1.1}$$

where ρ is the radius of the interferometer. If the interferometer revolves clockwise with rotation rate Ω, the effective segment AB is larger than $\pi\rho$ for the clockwise propagating beam and smaller than $\pi\rho$ for the counter clockwise propagating beam. The expressions for the path length $l^{\pm}$ in a laboratory (stationary) system is given by

$$l^{\pm} = \pi\,\rho \pm \rho\,\Omega\,\tau^{\pm}\ , \tag{1.2}$$

where $\tau^{\pm}$ are the arrival times of the counterpropagating wavefronts at point B. Using the relativistic law of velocity composition we obtain the modified phase velocities

$$v_{ph}^{\pm} = \frac{v_{ph} \pm \rho\,\Omega}{1 \pm v_{ph}\,\rho\,\Omega/c^2}\ , \tag{1.3}$$

where c is the speed of light in vacuum.
Now we can substitute the identity $\tau^{\pm} = l^{\pm}/v_{ph}^{\pm}$ into Eq.(1.2), and solve Eq.(1.2) and Eq.(1.3) for $\tau^{\pm}$

$$\tau^{\pm} = \frac{\pi\,\rho(1 \pm v_{ph}\,\rho\,\Omega/c^2)}{v_{ph}\,(1 - \rho^2\,\Omega^2/c^2)}\ . \tag{1.4}$$

The time difference between counterpropagating waves is found as

$$\Delta\,\tau = \tau^{+} - \tau^{-} = \frac{2\,\pi\,\rho^2\,\Omega}{c^2\,(1 - \rho^2\,\Omega^2/c^2)} = \frac{2\,s\,\Omega}{c^2\,(1 - \rho^2\,\Omega^2/c^2)}\ , \tag{1.5}$$

where s is the area enclosed by the interferometer (note that $\Delta\,\tau$ is independent of the phase velocityies). The Sagnac phase can be calculated from the quantity

$$\Phi = \mathbf{k}\,\mathbf{r} \pm \omega\,t\ , \tag{1.6}$$

where $\mathbf{k} = k_x\mathbf{x} + k_y\mathbf{y} + k_z\mathbf{z}$ is the vector formed by wave numbers k_x, k_y, k_z, $k_i = 2\,\pi/\lambda$, λ is the wavelength; $\mathbf{r} = x\mathbf{x} + y\mathbf{y} + z\mathbf{z}$, $\mathbf{x}$,$\mathbf{y}$,$\mathbf{z}$ are the orthogonal unit vector; t is the time and ω is the wave frequency. Now we transform to the rotating frame of reference. Since the phase Φ is invariant under this transformation the Sagnac phase can still be calculated

in the same way in the new frame of reference. In the rotating frame the length of the interferometer arm is exactly the same for both counterpropagating waves and therefore the time delay is the only source for phase shift between the arms. Multiplying Eq.(1.5) by the wave frequency ω_0, we obtain the phase difference between the two arms,

$$\Delta\phi = \frac{2\,s\,\omega_0\Omega}{c^2\,(1-\rho^2\,\Omega^2/c^2)} \approx \frac{2\,s\,\omega_0\Omega}{c^2}\ , \tag{1.7}$$

where we assume that $\rho^2\,\Omega^2/c^2 \ll 1$. For photons, ω_0 is the photon frequency and for matter wave we substitute its angular frequency

$$\omega_0 = \frac{\sqrt{m^2c^4+p^2c^2}}{\hbar} \approx \frac{m\,c^2}{\hbar}\ , \tag{1.8}$$

where $\hbar$ is Planck constant and m is the particle rest mass, into Eq.(1.7), to obtain the Sagnac phase shift for a massive particle,

$$\Delta\phi_{matter} = \frac{2ms}{\hbar}\Omega \equiv \alpha\Omega\ . \tag{1.9}$$

In chapter 3 we give another derivation which is appropriate only for massive particles. Comparing the phase shift of a massive particle and a photon we obtain[10],

$$\frac{\Delta\phi_{matter}}{\Delta\phi_{photon}} = \frac{\frac{2ms}{\hbar}\Omega}{\frac{2s\omega_0}{c^2}\Omega} = \frac{mc^2}{\hbar\omega_0} \gg 1, \tag{1.10}$$

For a typical atom, the quantity $m\,c^2$ is of the order $\sim 10^{-9}\,J$, while for visible light the quantity $\hbar\omega_0$ is of the order $\sim 10^{-19}\,J$. For an equal interferometer area and similar coherence properties, one can expect a ratio of $\approx 10^{10}$ per particle between a Sagnac phase shift, accumulated in a revolving atom interferometer and one that has been accumulated in a revolving light interferometer. The meaning of this ratio is that the transmission of

an atom interferometer is much more sensitive to small changes in the rotation rate than the transmission of a revolving light interferometer, i.e. atom based rotation sensors would be much more sensitive to rotations. In practice, the sensitivity of a rotation rate sensor depends also on other parameters (see section 3.6) such as the signal to noise ratio, which is better for the photon interferometer due to higher particle flux. Furthermore, the usage of a long optical fiber with multiple windings allows for constructing of effectively large area interferometers, rendering the sensitivities ratio between atom interferometer and light interferometer much smaller.

Many research groups around the world are making progress in the area of guided atom interferometry, but the goal of constructing a guided Sagnac atom interferometer has not been achieved yet and the feasibility of high finesse (many cycles) guided atom interferometry is still unclear. In this work we present a simple theoretical model that describes the behavior of a particle in a Sagnac atom interferometer. The model does not take in account non-linear effects resulting by atom-atom interactions, and magnetic impurities in the atomic waveguide are also neglected. The model is based on the analogy between a massive particle travelling in a rotating frame and a charged particle travelling in a ring with magnetic flux. We make use of scattering matrix formalism in order to obtain the transmission of a revolving atom interferometer. The transmission is a key element in the calculation of the interferometer sensitivity. The model can be applied for many geometries and in this work we investigate three different geometries in different finesse regimes.

The outline of this work is as follows. In chapter 2 we briefly review the latest experiments in the area of atom interferometry and atom ring traps. In chapter 3 we give a theoretical background and introduce the physical model. Then in chapter 4 we explain our calculations and present our results for interferometer transmission and interferometer sensitivity for different geometries. A summary, conclusions and future work are presented in chapter 5.

2. REVIEW OF EXISTING EXPERIMENTS

Matter-wave interference experiments enable us to study matter at its most basic quantum level, and form the basis of high-precision sensors for applications such as inertial and gravitational field sensing. Success in both of these pursuits requires the development of atom-optical elements that can manipulate matter waves while preserving their coherence and phase [7]. In this chapter we will review some of the latest experimental methods related to atom interferometry and its components. The chapter is organized as follows. In section 2.1 we describe a few of the latest experimental methods to split and guide atoms. In addition we describe trapped atom interferometers. In section 2.2 we review the state of the art in the area of atomic ring traps. This element is likely to be a key element in multi-pass atom interferometry. In section 2.3 we review the latest experiments in the area of free space beam-splitters and Sagnac atom interferometry.

2.1. Wave Guides, Beam Splitters and Trapped Atom Interferometers

Wave guides and beam splitters are key elements in optics and its applications. In atom optics beam splitters were, up to the recent years, demonstrated only for atoms moving in free space, interacting either with materials gratings [1], periodic potentials [3], or semi-transparent mirror formed by a sheet of light[5]. In this sub-chapter we will review the most progressive scientific achievements in the area of guiding atoms, beam-splitters and trapped atoms interferometers.

1) Atom Interferometry on a Chip with RF Magnetic Potentials.
J. Schmiedmayer Group, University of Heidelberg, Germany [7, 11–14]

Neutral atoms can be manipulated by means of their interactions with magnetic, electric [11, 12]and optical fields. Similarly to mesoscopic quantum electronics, where electrons move inside semiconductor structures and are manipulated using potentials, neutral atoms can move microns above surfaces, in potentials originating from micro-fabricated charged

and current carrying structures on the surface.

The group of Schmiedmayer from the university of Heidelberg is one of the pioneering groups in theoretical and experimental research of the wide field of microscopic guided atom optics. This group introduced a few traps and guides using micro-fabricated charged and current carrying structures. Surfaces carrying such structures, form the so-called atom chip [13], which may form the basis for a variety of applications and research tools for coherent matter wave optics, similar to what integrated circuits are for electronics. In 2005 this group reported on the first ever coherent splitting of a cloud of atoms, or more precisely of a Bose-Einstein Condensation (BEC), without optical means. By coherent splitting we mean that the phase of the interference pattern is preserved over many experimental repetitions. In the following, we briefly introduce the basic principle of neutral atoms manipulation with electro-magnetic fields following which we describe the experiment.

A particle with total spin $\mathbf{F}$ and magnetic moment $\mu = g_F \mu_B \mathbf{F}$ experience the potential

$$V_{mag} = -\mu \cdot B = -g_F m_F \mu_B B \tag{2.1}$$

where μ_B is the Bhor magneton, g_F the Landé factor of the atomic hyperfine state, and m_F is the magnetic quantum number. In General, the vector product $\mu \cdot B$ results in complicated motion of the atom. However, if the Larmor precession, $\omega_L = \mu_B B/\hbar$, of the magnetic moment is much larger than the apparent change of direction of the magnetic field, an adiabatic approximation can be applied. The magnetic moment then follows the direction of the field adiabatically, m_F is a constant of motion, and atom is moving in a potential proportional to the modulus of the magnetic field $B = |\mathbf{B}|$.

The orientation of μ relative to direction of the static magnetic field distinguishes between two cases (these definitions are reversed for a reversed sign of g_F):

(1) if the magnetic moment is pointing in the same direction as the magnetic field, i.e. $V_{mag} < 0$, the minima of the potential energy are found at maxima of the field and an atom is attracted towards increasing fields. This state called high field seeking state.

(2) if the magnetic moment is pointing in the direction opposite to the magnetic field, i.e. $V_{mag} > 0$, the atom is repelled from region with high magnetic field. It is then in the low field seeking state.

As noted previously, in 2005 a matter wave interferometer in a double well was realized on an atom chip. This of course means also that a scheme for a phase preserving matter-wave beam splitter was realized. This scheme is based on a combination of static and radio-frequency (RF) magnetic fields forming an adiabatic potential. The operation principle of the beam splitter is illustrated in Fig.(2).

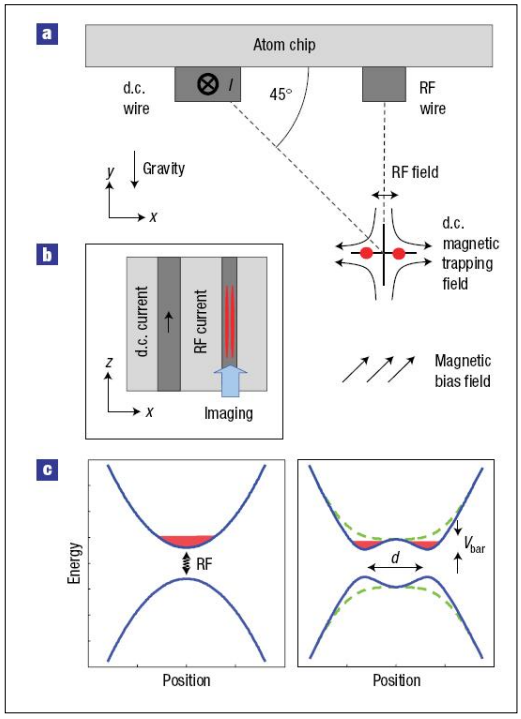

FIG. 2: Operation principle of the beam splitter. (a) A straight wire carrying a static (d.c.) current ($\sim 1A$) is used to trap a BEC on an atom chip directly below a second wire carrying a RF current ($\sim 60mA$ at $500kHz$). The d.c. wire has a width of $50\mu m$, and is separated by $80\mu m$ from the RF wire (width $10\mu m$). Placing the trap $80\mu m$ from the chip surface at the indicated position allows for symmetric horizontal splitting. (b) Top view onto the atom chip: an elongated BEC is transversely split. (c) Left: the RF magnetic field couples different atomic spin states (only two shown for simplicity). Right: the initial d.c. trapping potential is deformed to an effective adiabatic potential under the influence of the RF field with a frequency below the Larmor frequency at the trap minimum ($\sim 1G$). In the vertical (y) direction, the spatially homogeneous RF coupling strength leads to a slight relaxation of the static trap (dashed green line). Along the horizontal (x) direction, the additional effect of local variations of the RF coupling breaks the rotational symmetry of the trap and allows for the formation of a double-well potential with a well separation d and potential barrier height V_{bar} (solid blue line). Taken from Ref. [7].

A standard magnetic micro trap [11] is formed by the combined fields of a current-carrying trapping wire and an external bias field. A static magnetic field minimum is then formed and atoms in low field-seeking states can be trapped. An RF field generated by an independent wire carrying an alternating current couples internal atomic states with different magnetic moments. Owing to the strong gradients in a micro trap, the angle between the RF field and the local static magnetic field varies significantly over short distances, resulting in a corresponding local variation of the RF coupling strength. By slowly changing the parameters of the RF current the adiabatic potentials smoothly change as well and transform a tight magnetic trap into a steep double well, thereby dynamically splitting a BEC without exciting it. The splitting distance may be accurately controlled over a wide range. The potential barrier between the two wells can be raised gradually with high precision, thus enabling access to the tunnelling regime as well as to the regime of entirely isolated wells. The beam splitter is fully integrated on the atom chip, as the manipulating potentials are provided by current-carrying micro fabricated wires. The use of chip-wire structures allows one to create sufficiently strong RF fields with only moderate currents and permits precise control over the orientation of the RF field.

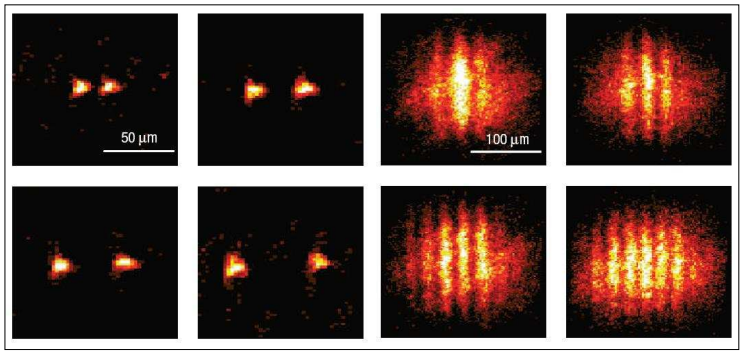

FIG. 3: (left) The cloud separation is derived from in situ absorption images. (right) The interference patterns are obtained after $14ms$ potential-free time-of-flight expansion of the two BECs. Taken from Ref. [7].

After the preparation of BECs of up to $\sim 10^5$ rubidium atoms in the $F = m_F = 2$ hyperfine state the amplitude of the RF field is ramped, in order to smoothly split the BEC confined in a single trap into two (Fig.(3) left). The split clouds recombined together in time-of-flight

expansion after a non-adiabatically fast ($< 50\mu s$) extinction of the double-well potential. Typical matter-wave interference patterns obtained by taking absorption images $14ms$ after releasing the clouds are depicted in Fig.(3) (right). The transverse density profile derived from these images contains information on both the distance d of the BECs in the double well potential and the relative phase ϕ of the two condensates. A cosine function fit with a Gaussian envelope to the measured profiles determines the fringe spacing Δz and the phase ϕ. Fig.(4) shows the results for 40 repetitions of the interference experiment performed directly after the two condensates are separated (Fig.(4)a) and after they have been taken farther apart (Fig.(4)b), respectively. A very narrow phase distribution was found, with a Gaussian width of $\sigma = 13^0$ and $\sigma = 28^0$, respectively. Hence, the splitting process is phase-preserving and the beam splitter is coherent.

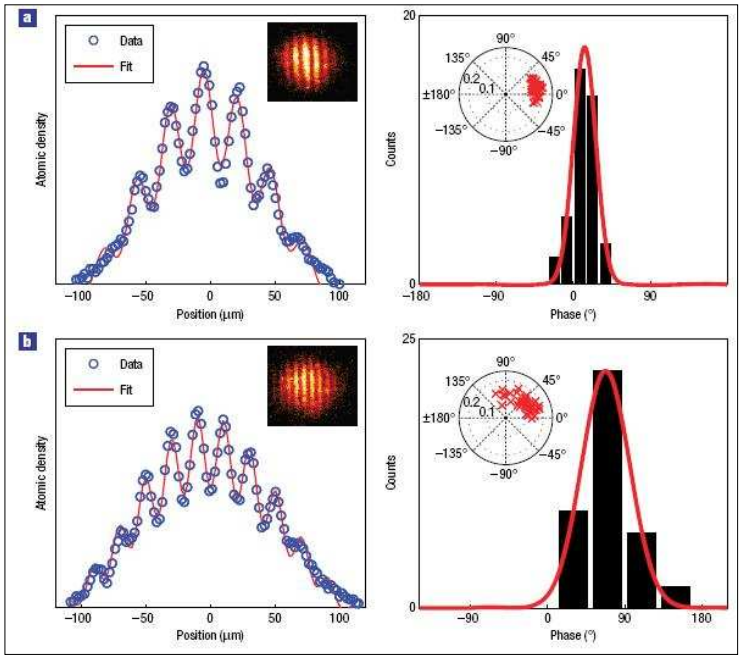

FIG. 4: The coherence of the splitting is examined by analyzing the interference patterns. (a) After $0.1ms$ at which time the BECs have been split far enough ($d = 3.4\mu m$) to inhibit tunneling completely. (b) After $0.8ms$ at which time the clouds have been taken even farther apart ($d = 3.85\mu m$). Left: a cosine function with a Gaussian envelope is fitted to the profiles derived from the two-dimensional images (insets). This yields information on fringe spacing, contrast and phase. Right: contrast and relative phase for 40 realizations of the same experiment are plotted in a polar diagram (inset). A histogram of the same data shows a very narrow distribution of the differential phase ($\sigma = 13^0$) directly after separating the clouds and a slightly broadened distribution ($\sigma = 28^0$) later in the splitting process. Both phase spreads are significantly smaller than what is expected for a random phase. Taken from Ref.[7].

2) Atom Interferometry on a Chip with Static Potentials.

W. Ketterle and D. E. Pritchard Group, MIT, Cambridge, Massachusetts. [6]

Ketterle's group demonstrated a trapped-atom interferometer with Bose-Einstein condensates confined in an optical double-well potential [6]. Condensates were coherently split by deforming an initially single-well potential into two wells separated by 13 μm. The relative phase between the two condensates was determined from the spatial phase of the matter wave interference pattern formed upon releasing the atoms from the separated potential wells. This recombination method detects applied phase shifts on a single realization of the experiment.

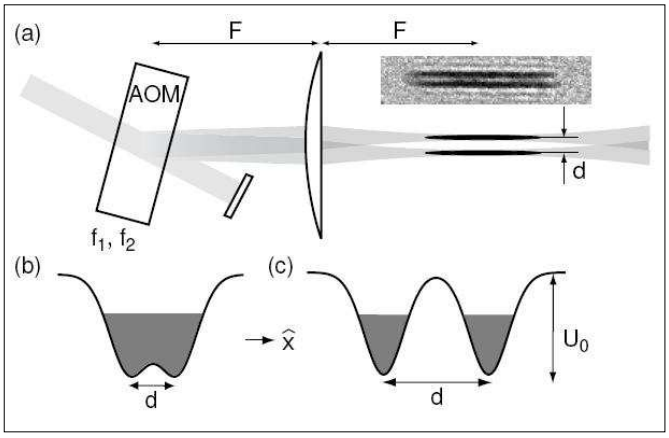

FIG. 5: (a) Schematic diagram of the optical setup for the double-well potential. An acousto-optic modulator (AOM) was driven by two frequencies, f_1 and f_2, and diffracted a collimated beam into two beams. The AOM was placed in the focal plane of a lens of focal length F so that the two beams propagated parallel to each other. The radial separation of the potential wells, d, was controlled by the frequency difference, $\Delta f = |f_1 - f_2|$. The absorption image shows two well-separated condensates confined in the double-well potential diagramed in (c). Energy diagrams describe the initial single-well trap with d = 6 μm (b) and the final double-well trap with d = 13 μm (c). In both (b) and (c), $U_0 = h \times 5kHz$. The potential "dimple" in (b) was $< h \times 500Hz$ which was much less than the peak atomic mean field energy allowing the trap to be characterized as a single-well. The potential "barrier" in (c) was $h \times 4.7kHz$ which was larger than the peak atomic mean field energy allowing the resulting split condensates to be characterized as independent. Taken from Ref. [6].

The large separation between the split potential wells allowed the phase of each condensate to evolve independently and either condensate to be addressed individually. An *ac* Stark phase shift was applied to either condensate by temporarily turning off the optical fields

generating its potential well. The spatial phase of the resulting matter wave interference pattern shifted linearly with the applied phase shift and was independent of the time of its application. This verified the phase sensitivity of the interferometer and the independent phase evolution of the separated condensates. The measured coherence time of the separated condensates was 5 ms.

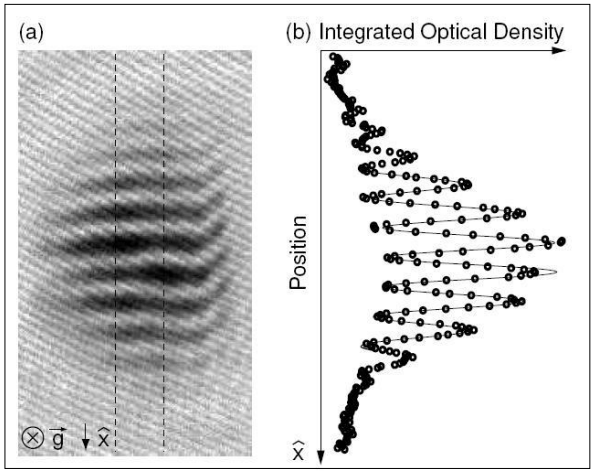

FIG. 6: Matter wave interference. (a) Absorption image of condensates released from the double-well potential in Fig. 5(c) and allowed to overlap during 30 ms of ballistic expansion. The imaging axis was parallel to the direction of gravitational acceleration, $\vec{g}$. The field of view is $600\mu m \times 350\mu m$. (b) Radial density profiles were obtained by integrating the absorption signal between the dashed lines, and typical images gave $> 60\%$ contrast. The solid line is a fit to a sinusoidally-modulated Gaussian. Taken from Ref.[6].

A schematic diagram of the setup for the interferometer's optical trap is shown in Fig.(5)a. The optical potentials were derived from a collimated laser beam that passed through an acousto-optic modulator (AOM) and was focused onto the condensate with a lens. The AOM was driven by two radio frequency (rf) signals to create the double-well potential. The separation between the potential wells was controlled by the frequency difference between the rf drives. The condensate was initially loaded into the single-well trap shown in Fig.(5)b. The cloud was held in this trap for 15 seconds to damp excitations. The single-well trap was deformed into the double-well potential shown in Fig.(5)c by linearly increasing the frequency difference between the rf signals driving the AOM.

The condensates were sufficiently separated that their phases evolved independent of each other to the extent that no coupling between the potential wells could be detected. This

claim is supported qualitatively by the absorption image in Fig.(6)a and the observation of high contrast matter wave interference patterns that penetrated the full atomic density profile with uniform spatial period and no thick central fringe.

The coherent phase evolution of the split condensates is displayed quantitatively in Fig.(7). The relative phase, ϕ_r, between the separated condensates was observed to evolve linearly in time and the standard deviation of eight measurements of ϕ_f (The phase of the interference pattern with respect to a chosen fixed x0) was < 90 degrees up to $5ms$ after splitting.

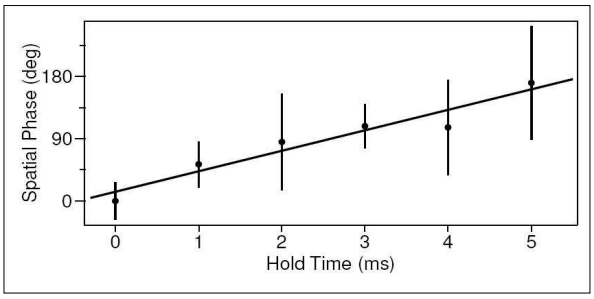

FIG. 7: Phase coherence of the separated condensates. The spatial phase of the interference pattern is plotted versus hold time after splitting. Each point represents the average of eight measurements, and the error bars are one standard deviation. The phase evolution was due to unequal trap depths for the two wells, which was determined from the linear fit to be $h \times 70Hz$ or $\sim 1\%$ of the trap depth. Taken from Ref. [6].

3) Proposals for Guided Atom Interferometry with Optical Potentials.

W. Ertmer Group, University of Hannover, Germany. [15]

Ertmer and his group from the university of Hannover introduced a new direction in the field of atom optics and atom interferometry. It is based on the use of micro fabricated optical elements to manipulate neutral atoms. The optical manipulation of neutral atoms is based on the electric dipole interaction of atoms with laser light. In general, light may be used for cooling of atoms, state preparation and detection of atoms, and for trapping due to an energy shift experienced by the atoms, which gives rise to the dipole potential. In the following, we briefly introduce the basic principle of optical manipulation of neutral atoms and in due course we describe some the suggestions for beam-splitters and wave-guides.

For a basic understanding of this method, it is sufficient to assume the atom to act as a two-level system ignoring the details of its internal sub-structure. The rate of spontaneous scattering processes is given by

$$\Gamma_{sc}(r) = \frac{3\pi c^2}{2\hbar\omega_0^3}\left(\frac{\omega_L}{\omega_0}\right)^3\left(\frac{\Gamma}{\omega_0-\omega_L}+\frac{\Gamma}{\omega_0+\omega_L}\right)^2 I(r)\ , \tag{2.2}$$

where ω_L and ω_0 are the laser frequency and the atomic resonance frequency respectively, Γ is the natural decay rate of the population in the excited state and $I(r)$ is the position dependent laser intensity. This result is valid for negligible saturation ($\Gamma_{sc} \ll \Gamma$) and large detuning $|\Delta| \equiv |\omega_0 - \omega_L| \gg \Gamma$. A conservative, non-dissipative force acting on the atoms is derivable from the dipole potential

$$U(r) = \frac{3\pi c^2}{2\omega_0^3}\left(\frac{\Gamma}{\omega_0-\omega_L}+\frac{\Gamma}{\omega_0+\omega_L}\right) I(r)\ , \tag{2.3}$$

The direction of the dipole force depends on the sign of the detuning Δ. The dipole force is attractive if the frequency of the laser light lies below an atomic resonance ($\Delta > 0$ - red detuning), and repulsive if the frequency of the light lies above an atomic resonance ($\Delta < 0$ - blue detuning). For typical experimental conditions, the detuning is much smaller than the atomic resonance frequency ($|\Delta| \ll \omega_0$). In this regime the dipole potential scales as I/Δ, whereas the rate of spontaneous scattering scales as I/Δ^2. If decoherence caused by spontaneous scattering has to be suppressed, the detuning should be as large as possible.

By using cylindrical micro-lens, one-dimensional guiding structures for atoms can be developed (Fig.(8)). The light that is sent through such a system forms a single line-focus above the lens system. By focusing a red-detuned laser beam with homogeneous intensity distribution an atomic waveguide is formed. Atoms are confined in the two dimensions perpendicular to the lens axis but are free to propagate along the axis.

A combination of the light fields of two curved cylindrical micro-lenses, each micro-lens illuminated by a light beam under a different angle, yields a beam-splitter (Fig.(9)). In this configuration, the laser foci laterally displaced with respect to the center of the lenses. By an appropriate choice of the displacements, the guiding potentials of the waveguides can be made to overlap at the closest approach. Input wave packets propagating along one of the

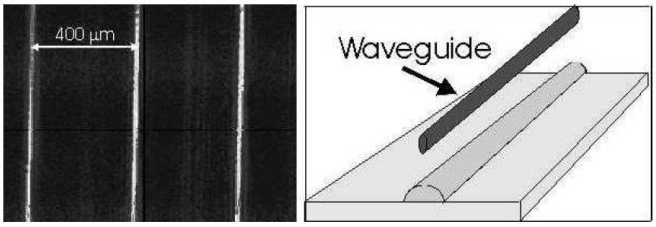

FIG. 8: Left: Section of an image of the intensity distribution in the focal plane of a cylindrical micro-lens array (lateral lens size and separation: 400 μm); Right: Atomic waveguide created by focusing a red-detuned laser beam with a cylindrical micro-lens. Taken from Ref.[15].

waveguides are split into up to four output wave packets propagating along both waveguides in both directions. Since the full structure is completely based on conservative potentials, the beam splitting process should be non-dissipative, so that coherent beam splitting of atomic matter waves is achievable.

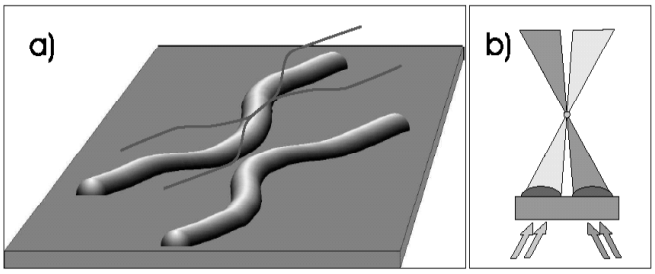

FIG. 9: (a) Beam splitter for atomic matter waves based on two micro-lens waveguides. (b) The micro-lenses are illuminated under different angles in order to make the laser foci overlap at the center of the beam splitter. Atomic wave packets entering along one waveguide are split into up to four output wave packets. Taken from Ref.[15].

This beam splitter can easily be extended to a micro-fabricated interferometer for atomic matter waves: Combining two beam splitters creates a Mach-Zehnder-type interferometer (Fig.(10)).

The two wave packets propagating along the output waveguides of the first beam splitter can be recombined in a second beam splitter and made to interfere. With typical laser powers guiding of ultra-cold atomic matter waves along micro-lens based waveguides over distances of several 10 mm is possible. This allows the realization of interferometers with an enclosed area of $\approx 1\ cm^2$. With microfabrication such a large area can be achieved in a system with dimensions that are significantly smaller than those of setups based on conventional methods. The Mach-Zehnder interferometer presented in Fig.(10) can be used

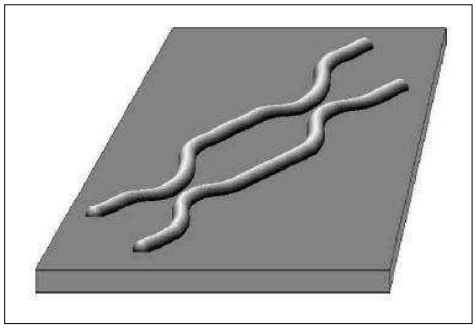

FIG. 10: Mach-Zehnder type interferometer based on a combination of two beam splitters. Taken from Ref.[15]

as a Sagnac interferometer.

2.2. Ring Traps

Guiding a matter wave on a torus is now being investigated by several groups. The motivation is clearly towards the realization of inertial sensors and gyroscopes, since, as analyzed in this thesis, a torus geometry is advantageous for the measurement of quantal phases. In addition, a torus trap filled with a degenerate atomic gas is also a source of inspiration for fundamental questions related to the coherence and super fluid properties of this trapped atomic wave. In this subsection I review some of the latest experiments in this area.

1) Ring Trap with Light Potentials Based on Microlens Arrays.
W. Ertmer Group, University of Hannover, Germany. [16]

Recently, Ertmer [16] and his group reported on the realization of an optical storage ring above a cylindrical ring lens and based on the same principles introduced in the previous sub-chapter (see Fig.(11)-left). The image on the right side of Fig.(11) is a fluorescence image of atoms which are trapped in a ring focus. To obtain this, a ring lens with a ring diameter of $D_{ring} = 1.5\ mm$ was illuminated with light from a Titanium-Sapphire laser, running at a wavelength of 780.7 nm, and the focus was superposed onto an atom trap, such that the upper part of the ring focus was overlapping with the trap. The trap was

then switched off to let the atoms un-trapped by the ring dipole trap leave the experimental region. The remaining atoms propagate in the ring structure.

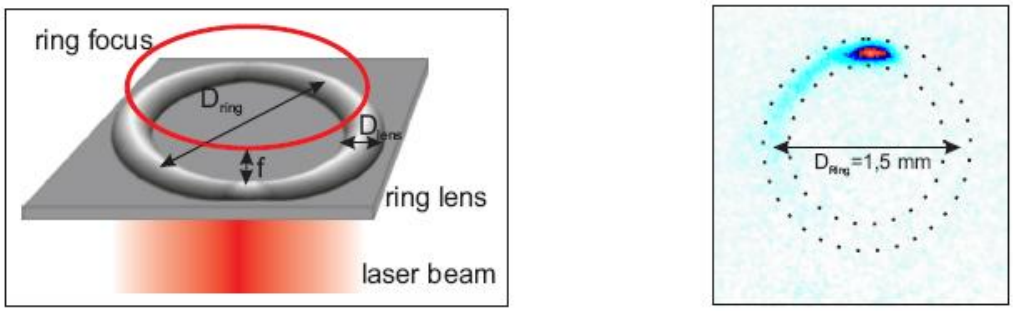

FIG. 11: Schematic of the ring lens (left) and fluorescence image of the atoms in the storage ring (right). Taken from Ref. [16].

2) Magnetic Ring Trap Using Current-Carrying Wires and Permanent Magnetic Structures
R. J. C. Spreeuw Group, University of Amsterdam, The Netherlands [17]

Spreeuw and his group presented a trapping configuration that enables the confinement of gases in a variety of multiply connected topologies. They used a combination of static and oscillating magnetic fields that give rise to adiabatic potentials. The trapping configuration is based on magnetic micro-structures and permanent magnetic structures. In order to ensure high field gradients (up to $10^3 T/m$), and the absence of lead wires that break the symmetry of the trap, a ring-shaped magnetic quadrupole field, generated by two concentric rings of magnetized material with out-of-plane magnetization M, was produced. A scheme of the ring shaped quadropole field is shown in Fig.(12). For small heights h of the magnetic layer, the field sources become equivalent to two pairs of concentric, counter-propagating, line-like currents $I = Mh$ around the edges of the material. They produce a magnetic quadrupole field with a ring-shaped line of zero field.

In order to avoid losses due to non-adiabatic spin flip transitions near the line of zero field, adiabatic radio-frequency (rf) induced potentials were utilized. Resonant coupling between Zeeman levels produces local potential minima near positions where the coupling field is resonant with the atomic Larmor frequency. A visualization of the trapping potential is

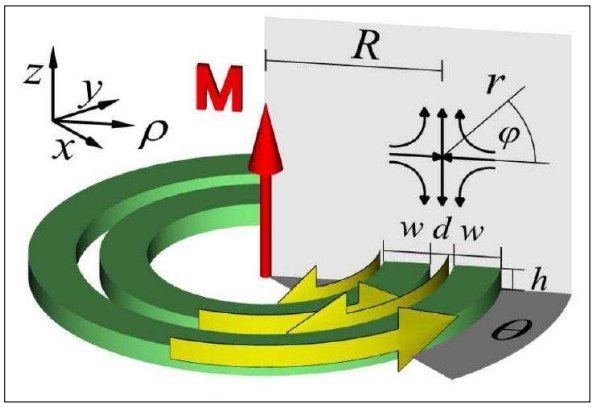

FIG. 12: Schematic view of a ring-shaped quadrupole field produced by two rings of uniform magnetization $M \cdot \hat{z}$, mean radius R, widths w, distance d, and height h. Additional coordinates are given by the distance r from the ring of zero field, and the toroidal and poloidal angles θ and φ, respectively. Taken from Ref. [17].

shown in Fig.(13).

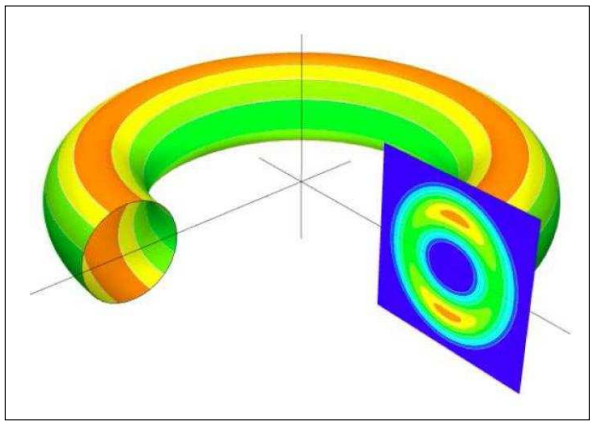

FIG. 13: Visualization of the adiabatic trapping potential. The potential on the resonant torus for vertically split rings is shown together with a cut parallel to a ρ, z-plane. Taken from Ref. [17].

3) Circular Waveguide Based on Coaxial Electro-magnetic Coils

D. M. Stamper-Kurn Group, University of California, Berkeley, California, USA [18]

Stamper-Kurn and his group from Berkeley reported on the creation of a smooth, stable circular waveguide for ultracold atoms. A simple arrangement of coaxial electro-magnetic coils was used to produce a static ring-shaped magnetic trap (Q ring), in which strong transverse confinement is provided by a two-dimensional quadrupole field.

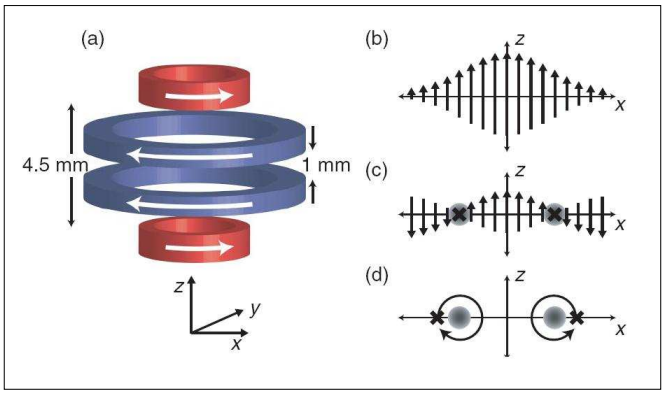

FIG. 14: Forming a circular magnetic waveguide. (a) Four coaxial circular electromagnets are used to generate both the static and rotating fields needed for the waveguide. (b) The field (arrows) from just the two outer coils (curvature coils, outer pair) points axially in the midplane between the coils, with largest fields at the axis. (c) Adding a uniform opposing bias field (using antibias coils, inner pair) produces a ring of field zeros ($\times$) in the $\hat{x} - \hat{y}$ plane around which weak-field seeking atoms (shaded region) are trapped. (d) Rapidly rotating the field zeros around the trapped atoms produces a time-orbiting ring trap. Taken from Ref. [18].

The Q ring is formed using a set of four coaxial circular electromagnets (see Fig.(14)) generating both the static and rotating fields needed for the waveguide. The trapping lifetime of atoms in the Q ring is limited by spin flips (Majorana) losses. In a balanced Q ring, trapped atoms passing close to the line of zero field, which extends all around the ring, may flip their spins and be expelled from the trap. The high loss rates in the Q ring can be mended by rapidly rotating it around the trapped atoms, to create a time-orbiting ring trap (TORT) with nonzero bias field (Fig.(14)d).

As shown in Fig.(15) the trap lifetime dramatically increases by application of the TORT trap. Switching on the TORT, causes a fast loss of atoms and a simultaneous drop in their temperature. These loss and cooling are due to the evaporation of atoms from the trapped cloud. As the temperature dropped, the evaporation rate diminished and the lifetime of trapped atoms became vacuum limited at 90 s.

In order to assess the suitability of the TORT as an atomic waveguide for interferometry, the trapped BECs were launched into closed-loop circular motion along the guide. This was accomplished by reorienting the sideways bias field B_s, inducing the trapped BEC to accelerate toward the newly positioned tilted TORT trap minimum, while simultaneously reducing the magnitude of B_s to $Bs \sim 0$ and increasing the magnitude of the rotating field

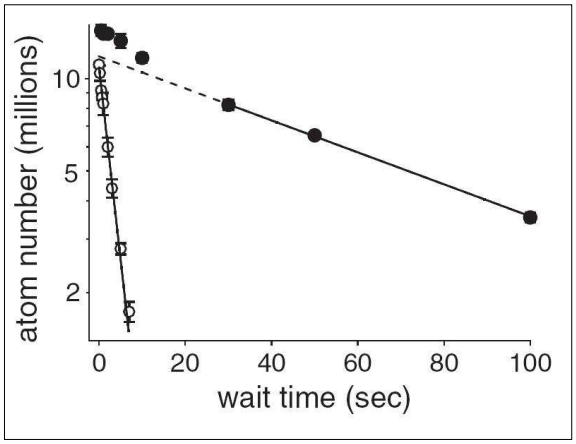

FIG. 15: Elimination of Majorana losses in the TORT. The measured number of trapped atoms in a Q ring (open circles) or TORT (solid circles) trap is shown vs residence time in the trap. Taken from Ref. [18].

seen at the trap minimum, to produce a well-balanced TORT trap.

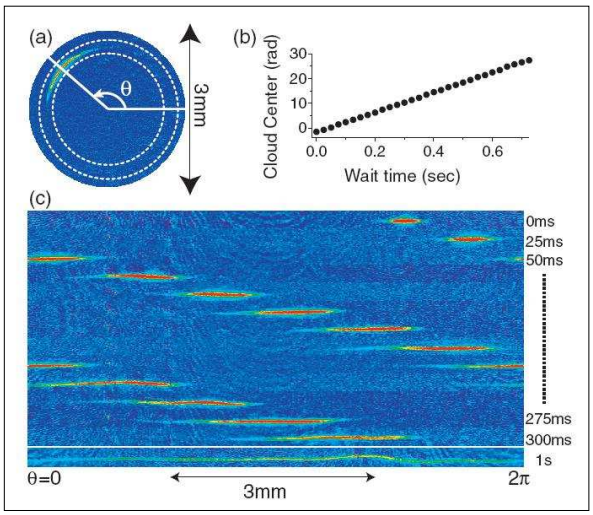

FIG. 16: Circular motion of a quantum degenerate atomic beam in a waveguide. A Bose-Einstein condensate was launched into a balanced TORT and allowed to propagate. (a) Top view in-trap absorption image during the propagation. The mean azimuthal position of the BEC measured from such images is shown in (b). Annular portions (indicated by dashed circles) of top-view images taken at different guiding times are shown in (c) displayed in polar coordinates (radius vs azimuthal angle). The beam advances at an angular velocity of 40.5 rad/s while expanding due to an rms azimuthal velocity spread of 1.4 mm/s. After 1 s, the beam fills the entire guide. Taken from Ref. [18].

The atoms were allowed to propagate freely around the guide for various guiding times before being observed by absorption imaging. As shown in Fig.(16), the ultracold atomic beam propagated around the circular waveguide at an angular (linear) velocity of $40.5 rad/s$

$(50.6mm/s)$. The pulsed atom beam was characterized by an azimuthal rms velocity spread of $1.4mm/s$, as measured from the azimuthal extent of the atoms for different guiding times. This velocity is equivalent to a longitudinal kinetic temperature of $22nK$. After about $1s$ of guiding, the velocity variation caused the atomic cloud to spread throughout a distance of $L = 51mm$ along the waveguide, encompassing an area of $A = 32mm^2$. However, the expected fringe periodicity for a spatial interference, between the front and back ends of the expanding BEC, is well below the imaging resolution, and such interference was not observed.

4) Ring Trap Based on a Combination of RF Magnetic Trap and a Standing Wave of Light. H. Perrin Group, CNRS, France [19]

The group of Perrin proposed a toroidal trap geometry based on an adiabatic transformation of a radio-frequency two-dimensional trapping potential by the addition of a standing optical wave. Namely, this trap is the superposition of two different traps, an egg shell trap relying on a magnetic trapping field and rf coupling, combined with a standing wave of light.

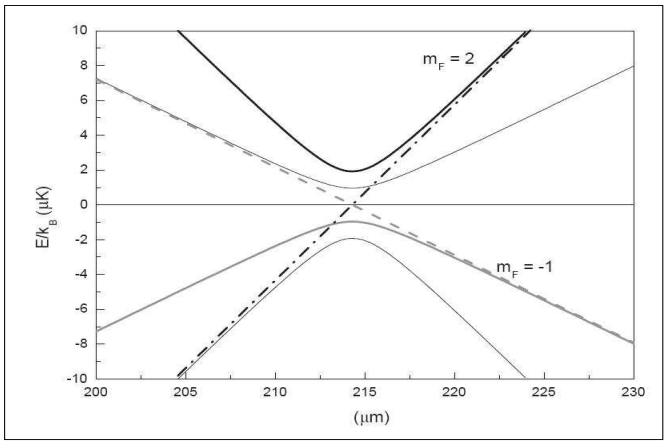

FIG. 17: Energy of the dressed levels in the magnetic quadrupole trap, plotted along the radial coordinate. The five dressed sub levels for a $F = 2$ spin state are plotted, as well as two bare states for comparison (bare state $m_F = -1$ is shown dashed and $m_F = 2$ dash-dotted). The ring trap is based on the upper dressed potential $m_F = F = 2$, for the radial trapping (bold solid line). Taken from Ref. [19].

In order to understand the principle of the rf-dressed potentials, let us examine the case of $^{87}Rb, F = 2$ ground state. An inhomogeneous magnetic field of norm $B(r)$ presenting a local minimum (the base of a magnetic trap) is used together with a rf coupling between

m_F Zeeman sub-states created by an oscillating magnetic field $B_{rf}\cos(\omega_{rf}t)$. This results in a dressing of the m_F states, as represented on Fig.(17), and the potential experienced by the upper adiabatic state reads:

$$V_d(r) = F((V_B(r) - \hbar\Delta)^2 + (\hbar\Omega)^2)^{\frac{1}{2}} \ , \tag{2.4}$$

where, $m_F = F = 2$ for ^{87}Rb and $V_B(r) = g_L\mu_B B(r)$ is the potential created by the magnetic trap alone for $F = 2,\ m_F = 1$, where g_L is the Landé factor and μ_B the Bohr magneton, $\Delta = \omega_{rf} - \omega_0$ is the detuning between the rf applied frequency and the resonant frequency at the magnetic potential minimum, and $\Omega = g_L\mu_B B_{rf}/2\hbar$ is the Rabi frequency of rf coupling. $V_d(r)$ has a minimum for $V_B(r) = \hbar\Delta$ (a surface defined by $g_L\mu_B B(r) = \hbar\Delta$.

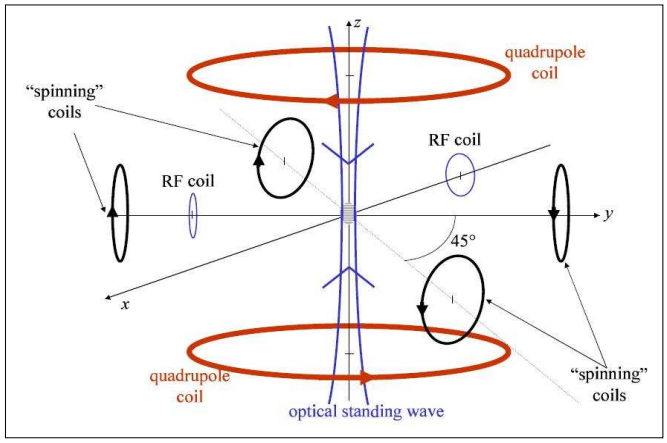

FIG. 18: Coils and laser configuration for producing and exciting the ring trap. The trap is the combination of a vertical light standing wave (blue beam on the figure) and an egg shell rf trap. This egg shell trap relies on a magnetic field gradient (produced by the quadrupole coils) and rf coupling between Zeeman sub levels. The additional spinning coils could be used for exciting the rotation of the atoms inside the ring trap. Taken from Ref. [19].

Regarding the case of a quadrupole trap with z as its symmetry axis, the magnetic field in the center is zero, so that $\Delta = \omega_{rf}$. Denoting the field gradient in the radial direction by b, and defining α as $\alpha = g_L\mu_B b/\hbar$, we obtain the potential of an atom in a dressed state

$$V_d(\rho, z) = F\hbar((\alpha\sqrt{\rho^2 + 4z^2} - \Delta)^2 + \Omega^2)^{\frac{1}{2}} \ , \tag{2.5}$$

where $\rho^2 = x^2 + y^2$. In the presence of gravity, the atoms fall to the bottom of this shell and

the resulting trapped cloud is in a quasi 2D geometry.

An additional optical standing wave, blue detuned (by $\delta > 0$ with respect to an atomic dipole transition), elongated to the vertical z direction, and with identical linear polarization for the two laser beams (Fig.(18)), will create a light shift. This light shift creates in its turn, a periodic potential of period $\lambda/2$ where λ is the light wavelength. Along z, the atoms are then confined in a series of parallel planes. As a result, if they also experience the adiabatic rf potential in a quadrupole trap, the atoms sit on a circle, the intersection of that plane and the ellipsoid, defined by $\rho = R$ of radius $R = \sqrt{r_0^2 - 4z_0^2}$ much greater than λ (Fig.(19)).

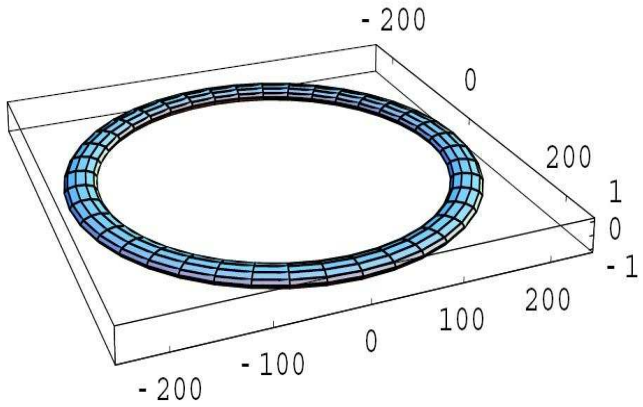

FIG. 19: A view of the ring trap. An isopotential surface is plotted for the given parameters: laser power-$P = 0.5\ W$, laser wavelength-$\lambda = 771\ nm$, rf frequency-$\Delta/2\pi = 2250\ kHz$ and magnetic field gradient-$b' = 150\ G/cm$. The length unit is $1\mu m$. The vertical direction is amplified 10 times for clarity. Taken from Ref. [19].

5) Atomic Micro Traps Generated by Multi-Frequency Magnetic Field Modulation

C. Zimmermann, University of Tubingen, Germany. [20]

Zimmermann and his group proposed a realization of a versatile atomic micro trap for cold atoms based on multimode radio frequency radiation in combination with static inhomogeneous magnetic fields. The use of radio frequency combs (the radio frequencies are of the form $\omega_n = 2\pi(c_1 + c_2 n)$, where c_1 and c_2 are constants) gives rise to periodic potentials acting as gratings for cold atoms. In strong magnetic field gradients the lattice constant can be well below $1\mu m$. By changing the frequencies of the comb in time, the

gratings can easily be propagated in space.

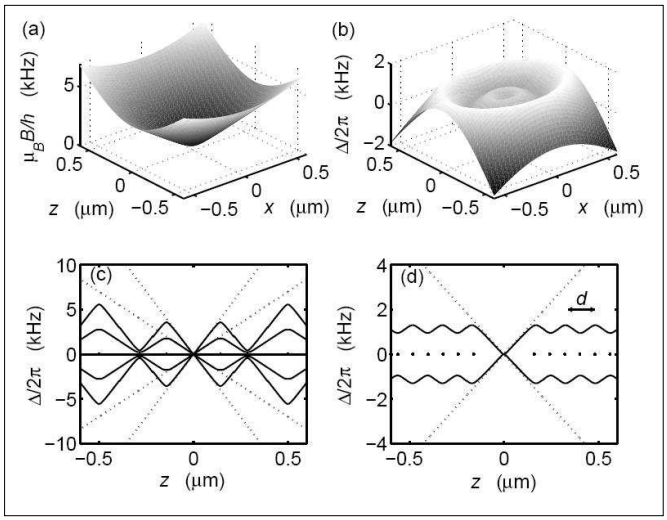

FIG. 20: (a) 2D quadrupole magnetic field with gradients $b_z = 200G/cm$ and $b_x = 140G/cm$. (b) Corresponding adiabatic potentials for the ^6Li two-level system $F = \frac{1}{2}$. (c) Adiabatic potentials for a system with five Zeeman substates, $F = 2$. (d) Adiabatic potentials for a frequency comb and the ^6Li two-level system. Taken from Ref. [20].

An incident microwave or radio frequency radiation can have a strong impact on a magnetic trapping potential. This is due to the fact that the potential depends on the magnetic substate of the trapped atoms. The energy of this substate can be manipulated by admixing other substates via resonant radio frequency radiation. In inhomogeneous magnetic fields this coupling is local and leads, within a dressed states picture, to avoided level crossings. Atoms moving across an area where the coupling is strong, follow adiabatic potentials by avoiding the crossings. Using this technique allows for an almost complete control over the spatial shape and the temporal evolution of the potentials. In particular, irregular patterns may be formed, and very small structures, only limited by the size of the technically feasible magnetic field gradient, may result in gratings with very small lattice constants. Fig.(20)a,b visualizes the case of a two-dimensional quadrupole magnetic field with three frequencies irradiated. Fig. 20(c) shows the adiabatic potentials for five Zeeman substates, as in the case of the ^7Li ground state hyperfine level $F = 2$. Finally, Fig.(20)d represents the adiabatic potentials for the case of a frequency comb $\omega_n = 2\pi \times (3+1.5n)kHz$.

6) Atomic Ring trap Based on Four Circular Water-Cooled Current Carriers

A. S. Arnold Group, University of Strathclyde, Scotland. [21, 22]

Arnold and his group from the university of Strathclyde in Scotland reported on the realization of a magnetic storage ring for cold atoms and a localized formation of Bose-Einstein condensate in a section of the torus. The magnetic coil design can be utilized as a magneto-optical trap or a storage ring. A large number of atoms can be confined in the ring and it has a long magnetic trap lifetime compared to other rings. Additionally, its large (10 cm) diameter and high level of optical access should facilitate atom interferometry.

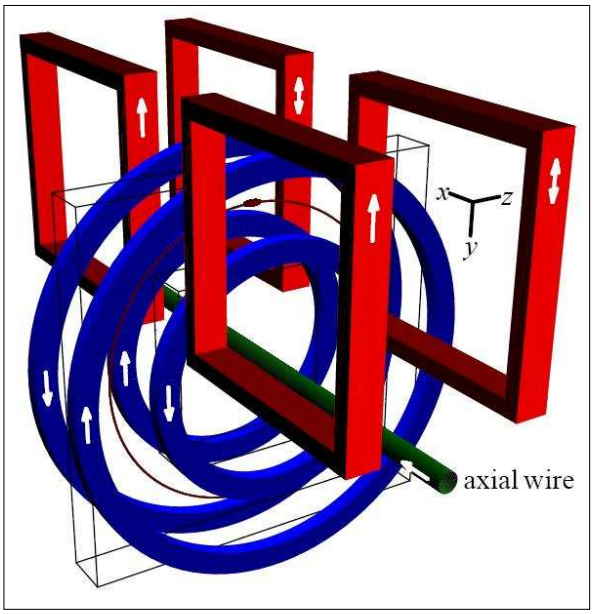

FIG. 21: Four circular coils with average diameter 10 cm make up the storage ring (thin circle) to which the axial wire adds an adjustable azimuthal magnetic field. The square coils localize the atoms (small cigar) in either a magneto-optical or magnetic trap depending on the current direction in the right square coil pair. Taken from Ref. [22].

Before loading into a Ioffe-Pritchard magnetic trap [23], the atoms are trapped in a double magneto-optical trap (MOT) system, in which the low pressure MOT contains around $N = 1\,10^9$ ^{87}Rb atoms. Four circular coils form a toroidal quadrupole field, where each coil consists of two water-cooled loops carrying a current of $500A$ and the geometric center of the coils has a diameter of $10cm$. Additional pinch coils at the top of the storage ring enable the formation of MOT and Ioffe-Pritchard field configuration [23] in a section of the torus.

This coil design allows cold atoms or condensates to be formed inside the storage ring. A scheme of the coil design is shown in Fig.(21)

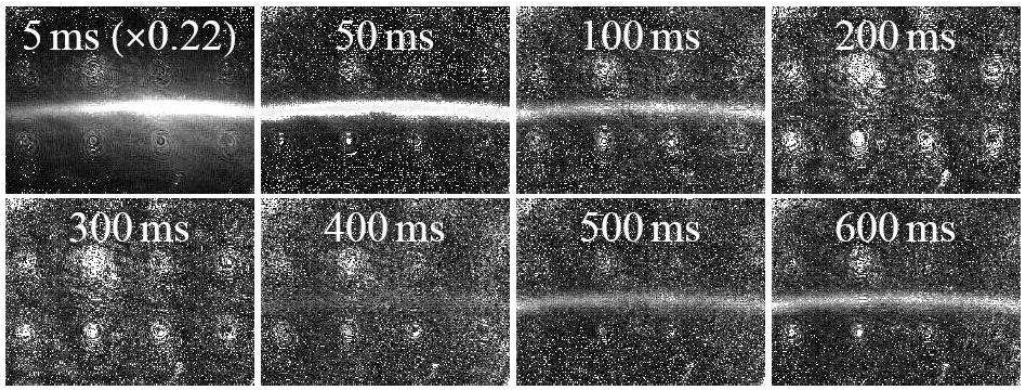

FIG. 22: Cold atoms with a temperature of $1\,mK$ confined in the storage ring. They disappear after $200\,ms$ and reappear after $600\,ms$. Each absorption image is $6.4\,mm$ wide, and the spots on either side of the trapped atoms are due to imperfections in the CCD camera. Taken from Ref. [21].

While the first storage rings contained 10^6 atoms/molecules with lifetimes of less than half a second, this storage ring contains more than 10^8 atoms and has a lifetime of $40sec$. The next step is the formation of Bose-Einstein condensates in a localized section of the ring by evaporatively cooling atoms in the storage ring's Ioffe-Pritchard magnetic trap configuration. The condensate fraction contains up to $N = 5\,10^5$ atoms. Up till now, experiments utilising the full extent of the storage ring have been performed only with cold atoms (see Fig.(22)), but very recently this group performed such an experiment with BECs [22]. In the near future there is an intention to perform Sagnac interferometry by locating the condensate at the exact top of the ring, and coherently splitting the sample by simply releasing it.

2.3. Free Space Beam Splitters and Atom Interferometers

As explained in the following, present day Sagnac free-space atom interferometers, are mostly based on two-photon Raman transitions to manipulate atoms. This way of operation, like any other free-space interferometer, imposes a single pass trajectory and therefore a large size interferometer in order to achieve a large area leading to high rotation sensitivity. To the best of my knowledge, the only usable Sagnac matter wave interferometer and the most sensitive known gyroscope is the free-space atom interferometer demonstrated by M.

A. Kasevich and his group.

1) Rotation Measurements with a Cesium Interferometer Gyroscope

M. A. Kasevich Group, Stanford University, California, USA [24–26]

A remarkable set of experiments was performed in the recent years by M.A. Kasevich and his group from Stanford University. This group developed an atomic state interferometer which uses two-photon velocity selective Raman transitions to manipulate atoms while keeping them in long-lived ground states. This device has a short-term rotation-rate sensitivity of $6 \cdot 10^{-10} rad/sec$ over one second of integration. This result is the best publicly reported value to date. A schematic of the interferometer configuration used for the gyroscope is shown in Fig.(23).

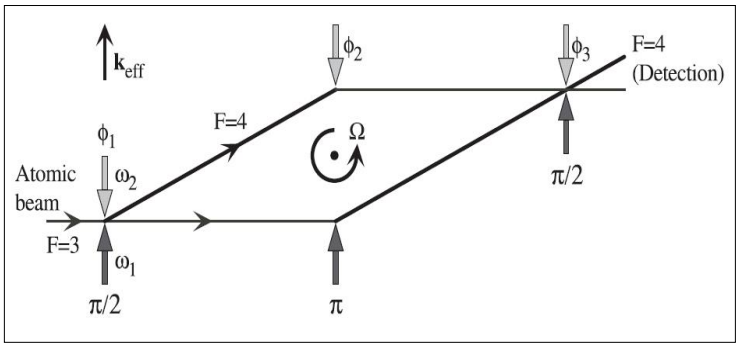

FIG. 23: Interferometer configuration. Three pairs of Raman beams are used to divide, deflect and recombine atomic trajectories. Taken from Ref. [25].

Briefly, counter propagating cesium atomic beams in an ultra-high-vacuum (UHV) chamber are transversely cooled, and optically pumped into a particular ground state before entering the interferometer region. There, three pairs of stimulated Raman transition lasers serve to divide, deflect, and recombine the atomic wavepackets. Interference between the two paths through the interferometer allows the rotation-rate dependent phase shift between the paths to be observed by detecting the number of atoms exiting the interferometer in a particular hyperfine electronic state, as measured by fluorescence from a resonant probe laser. The apparatus measures the relative angular velocity between the inertial frame of the freely falling atoms in the atomic beam, and the lab frame containing the optical table.

A uniform magnetic bias field is applied along the axis of the Raman beams throughout the length of the interferometer region, and a two-layer magnetic shield is used to protect this region from stray magnetic fields. Atoms in a thermal beam are pumped into the hyperfine $F = 3$ state, and then pass through a sequence of three Raman laser beams. The first beam ($\pi/2$ pulse) puts the atoms in a coherent superposition of the $F = 3$ and $F = 4$ ground states. Due to conservation of momentum with the laser interactions, each internal state is associated with a particular transverse momentum. Thus, this first pulse serves as a beam splitter, causing the atomic wavepackets to divide into two trajectories. The second beam (π pulse) acts as a mirror by exchanging the atomic states and momenta, deflecting the trajectories back towards each other. The third beam ($\pi/2$ pulse) acts as a beam-splitter that recombines the two trajectories so interference can occur. Rotation induces a relative phase-shift between the two paths of the interferometer, and the interference signal can be observed by measuring the number of atoms in the $F = 4$ state. Since atoms from the atomic beam have random relative phase, the interference effect is a single particle phenomenon with coherence length given by the de-Broglie wavelength. For initial verification of the sensitivity of the interferometer to rotations, the optical table is rotated mechanically, and a seismometer was used to determine the center of rotation and to calibrate the table motion. The table revolved at $4.5Hz$, near its resonance, and observed interference fringes using a single atomic beam as shown in Fig.(24).

A signal-to-noise ratio of $400 : 1$ for 800 $msec$ of integration per point, was measured, both at the center of the fringe and on the tails. A shift between the rotation zero measured by the seismometer and the contrast envelope center, was observed which indicates zero rotation as measured by the atoms. The offset arises because the seismometer is not sensitive to the constant rotation rate of the Earth but the gyroscope is, and measuring the offset gives the Earth rotation rate. A rotation rate of 45 ± 3 $\mu rad/sec$ was found, which is consistent with the expected value of 44.2 $\mu rad/sec$ for Stanford's latitude.

In the next step, an additional counter-propagating atomic beam used to determine absolute zero rotation rate (without using a seismometer). The Sagnac phase shift depends on the Coriolis acceleration, $a_{Cor} = -2\Omega \times v$ (see chapter 3) which is proportional to the vector velocity, v, and therefore has opposite sign for the two atomic beams. In the limit of perfect

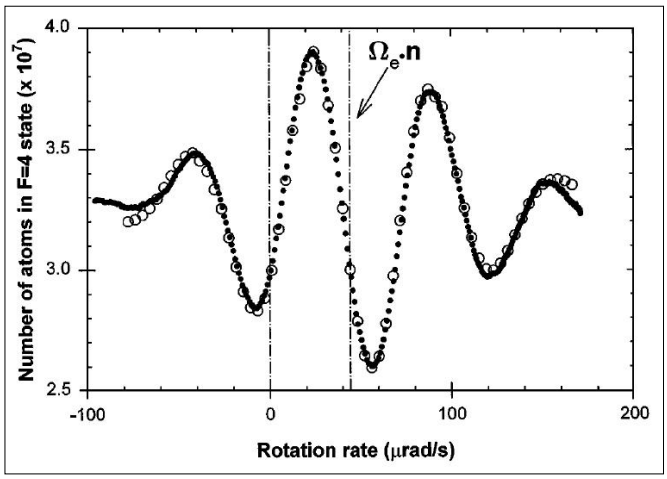

FIG. 24: Measurement of an atom interference pattern versus rotation rate. Black dots: experimental data. Open circles: calculated signal. The shift of the contrast envelope provides a measurement of the Earths rotation rate. Taken from Ref. [3].

contrast, the probability for an atom exiting the interferometer in the $F = 4$ state used for detection is equal to

$$P(F = 4) = \frac{1}{2}[1 - \cos(\phi_\Omega + \phi_{arb})] \ , \tag{2.6}$$

where ϕ_Ω is the Sagnac phase shift, and ϕ_{arb} is the sum of acceleration and the arbitrary laser phase. Therefore, the gyroscope signals corresponding to counter-propagating atomic beams have the form

$$\begin{aligned} S_{north} &\sim \cos(\phi_\Omega + \phi_{arb}) \\ S_{south} &\sim \cos(-\phi_\Omega + \phi_{arb}) \end{aligned} \tag{2.7}$$

where S represents the detected signal of the north or south atomic beam (north and south are arbitrary labels for the counter-propagating atomic beams). Using trigonometric identities, one can rearrange these equations as follows:

$$S_{north} - S_{south} \sim \sin(\phi_\Omega)\cos(\phi_{arb}) \tag{2.8}$$

Due to the sine factor, the difference signal has a zero crossing for zero rotation rate, and the amplitude factor (cosine) can be maximized by adjusting the arbitrary phase, as seen in

Fig.(25).

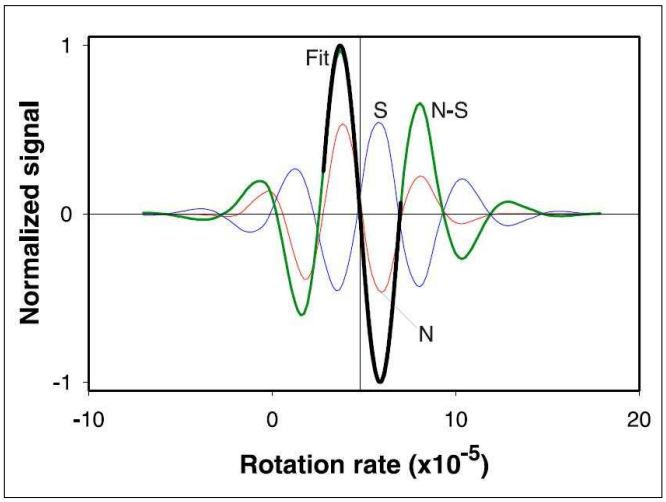

FIG. 25: Earth rotation rate measurement. The north and south rotation fringes are the symmetric signals shown with thin curves, the difference north - south is labeled N-S, and the fit to the center of the difference curve is shown with a heavy black curve. The arbitrary phase was chosen so that the north and south signals have opposite sign, maximizing the contrast of the difference signal. Taken from Ref. [25].

This method allows precise determination of the zero rotation rate relative to the non-rotating inertial frame, and does not depend on knowledge of the gyroscope area or arbitrary phase. To implement the counter-propagating atomic beams, Cesium sources were mounted at each end of the vacuum chamber and aligned to overlap spatially so that the beams would sample the same magnetic bias field (collisions are negligible). The atoms from each atomic beam are transversely cooled in two dimensions using red-detuned laser light, and are optically pumped into the $F = 3$ ground state before passing through the detection laser for the opposing atomic beam. Since the detection light was tuned to the $F = 4 \rightarrow F' = 5$ resonance, the only atoms detected are those that end up in the $F = 4$ state after the interferometer interaction pulses.

2) On-going Cesium Interferometer Gyroscope construction

C. J. Borde Group, Laboratoire de Physique des Lasers - CNRS, France. [27, 28]

A gyroscope based on de-Broglie wave interferences of cold Cesium atoms is under construction at the Observatoire de Paris. It consists of a rotating interferometer, using stimulated

Raman transitions to manipulate the atomic wave packets. When the setup rotates around its axis, a phase shift appears between the two interferometer arms, owing to the Sagnac effect. The number of atoms detected on one of the two outputs of the interferometer depends on this phase shift, which is proportional to the rotation rate of the gyroscope. The configuration used is similar to an optical Mach-Zehnder interferometer, as seen in Fig.(26).

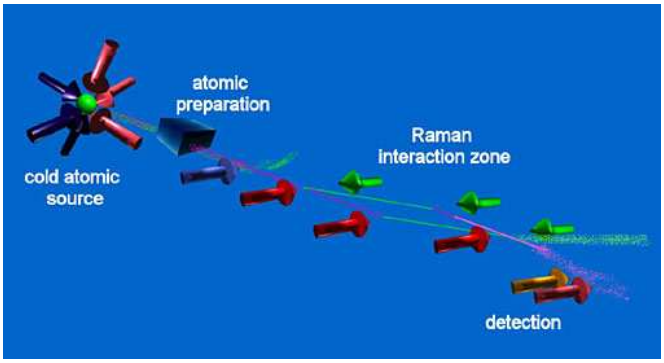

FIG. 26: Scheme of an atom interferometer providing large interferometer area. Taken from Ref. [28].

First, Cesium atoms are cooled with lasers in the three spatial directions, the temperature in the magneto-optical trap is as low as several μK. Then, atoms prepared in the $(6S_{1/2},\ F = 3,\ m_F = 0)$ state are launched at about $3m/sec$ toward the zone in which Raman lasers are used for the atomic wave packet manipulations. In this interaction zone, atoms are submitted to three stimulated Raman transitions which realize a $\pi/2 - \pi - \pi/2$ sequence. The time between consecutive laser pulses is 50 $msec$. The first pulse splits the atomic wave packet into two different states, $(6S_{1/2},\ F = 3,\ m_F = 0)$ and $(6S_{1/2},\ F = 4,\ m_F = 0)$, spatially separated. The second pulse acts as a mirror for both arms, then the third pulse recombines them. The Sagnac effect results in a phase shift between the two arms of the interferometer, which is proportional to the rotation rate of the gyroscope. Atomic interferences are then detected on one of the interferometer outputs, from which the phase shift is determined.
The atom interferometer is sensitive both to rotations around the axis perpendicular to its plane and to accelerations in the direction of the Raman lasers. To discriminate between these phenomena, two counter-propagating atomic beams which share the same Raman lasers were used. Any acceleration results in the same phase shift for both interferometers, whereas any rotation results in opposite phase shift. The rotation rate is deduced from

the difference of the two signals and the acceleration information from their sum. The two trajectories have to be superimposed to see the same phase shifts. This is the reason why atomic packets are launched with an angle of 8^o from the vertical axis defined by gravity. The trajectory is then a parabolic flight, as seen in Fig.(27).

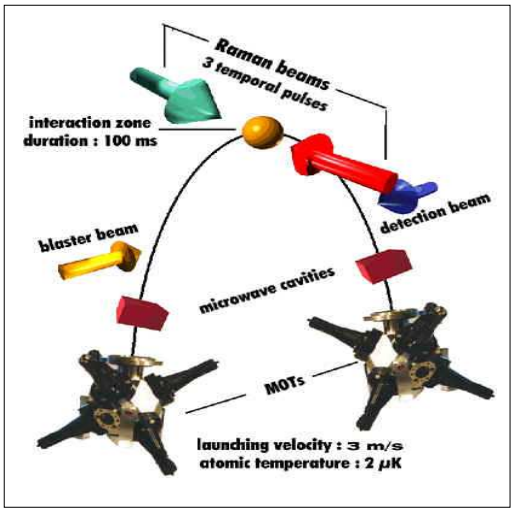

FIG. 27: Principle of the cold cesium gyro-accelerometer developed at the Paris Observatory. Taken from Ref. [28].

A sensitivity of $3 \cdot 10^{-8} rad/sec/\sqrt{Hz}$ is expected for rotation measurements, and $4 \cdot 10^{-8} m/sec^2/\sqrt{Hz}$ for accelerations. At the moment, the gyrometer is being improved and characterized and the optimum sensitivity of this setup should be reached soon.

3) On-going Rubidium Interferometer Gyroscope construction

W. Ertmer and E. Rasel Group, University of Hannover, Germany. [29]

Another gyroscope based on two-photon Raman transitions to manipulate atoms is under construction at the Hannover university. This experiment investigates different strategies for the realization of a transportable matter-wave sensor. It uses two counter-propagating pulsed or continuous beams of cold ^{87}Rb atoms to measure rotations thanks to the Sagnac-effect in a Mach-Zehnder type atom interferometer. The use of cold atoms makes it possible to realize compact devices with sensitivities competitive with classical state-of-the-art sensors. The heart of the set-up will be a 15 cm-long Mach-Zehnder interferometer in spatial and/or

temporal domain consisting of 3 atom-laser interactions. The length of the complete sensor will be about 90 cm. Each of the 2 atom sources consists of 2 magneto-optical traps (MOT): A 2-dimensional MOT, which forms a bright atomic beam, that is loaded into a 3D MOT to prepare a cold and intense atomic ensemble. A major goal is the transportability of the entire experiment. This has two reasons: First for a possible comparison of two atomic rotation sensors (such as the cold cesium atom gyroscope at the Observatoire de Paris), and also as a ground based test facility for future satellite missions. At the moment, the experiment is still under construction, but several experimental steps have already been realized. A Double MOT-system has been built and the most important experimental parameters were characterized. To realize a vacuum setup, that is as compact as possible, several new sealing techniques were employed and the final vacuum chamber has been completed.

3. THEORY

In this chapter we will stepwise introduce the physical model suggested in this thesis. In order to do so we will explain the basic terminology and derive the equations that are needed for understanding the model and its results as presented in chapter 4. The chapter is organized as follows. In Section 3.1 we describe the analogy between a neutral particle travelling in a rotating frame and a charged particle travelling in a ring with a magnetic flux. The physical model, based on the scattering matrix formalism is described in section 3.2. The model relies on the analogy introduced in section 3.1. In sections $3.3-3.5$ we apply the scattering matrix formalism to three special cases and obtain three sets of equations. A solution for each set describes the interferometer transmission for the given case. In section 3.6 we derive the expression for the interferometer sensitivity and describe its relation to noise. The coherence length for a none interacting particle in a rotating frame is derived in section 3.7. Sections $3.8-3.9$ are devoted to the relation between the finesse and the average number of cycles that a particle completes in the interferometer and to experimental limitation on the interferometer parameters.

3.1. The Analogy Between a Massive Particle in a Rotating Frame and a Charged Particle in a Ring with an induced Magnetic Flux

The phase shift derived in Eq.(1.9) could be also derived by making an analogy between a massive particle travelling in a rotating atom interferometer and a charged particle travelling in an interferometer with a magnetic flux [30]. The quantum mechanical phenomenon by which a charged particle is affected by electromagnetic fields in regions from which the particle is excluded is known as the Aharonov-Bohm effect [31]. A commonly described case is when the wave function of a charged particle passing around a ring experiences a phase shift as a result of the enclosed magnetic field, despite the magnetic field being zero in the region through which the particle passes. This phase shift has been observed experimentally by its affect on interference fringes.

The magnetic force applied on a charged particle is given by

$$F_{Lor} = \frac{e}{c}\mathbf{v} \times \mathbf{B} = \frac{e}{c}\mathbf{v} \times (\nabla \times \mathbf{A}) \ , \tag{3.1}$$

where $\mathbf{v}$ is the particle velocity, $\mathbf{B}$ is the magnetic field and $\mathbf{A}$ stands for the vector potential. The Lorentz force is analogous in form to the Coriolis force which acts on a particle in a rotating frame,

$$F_{Cor} = 2m\mathbf{v} \times \mathbf{\Omega} \ , \tag{3.2}$$

where the direction of Ω is perpendicular to rotating frame. From this analogy one can describe a massive neutral particle which feels a Coriolis force in terms of an electron in presence of effective magnetic field

$$B_{eff} = \frac{2mc}{e}\mathbf{\Omega} \ . \tag{3.3}$$

If a beam of charged particles in a presence of $\mathbf{A}$ is split into two paths and then recombines, the resulting phase difference between the two paths is proportional to the magnetic flux enclosed by the interferometer

$$\phi = \frac{e}{\hbar c}\oint \mathbf{A} \cdot d\mathbf{l} = \frac{e}{\hbar c}\int \mathbf{B} \cdot d\sigma \ . \tag{3.4}$$

Substitute Eq.(3.3) into Eq.(3.4) (Ω is spatially uniform) we obtain

$$\phi = \frac{2m}{\hbar}\int \mathbf{\Omega} \cdot d\sigma = \frac{2ms}{\hbar}\Omega \ , \tag{3.5}$$

as was derived in Eq.(1.9) and the magnitude of $\mathbf{A}_{eff}$ is given by

$$|A_{eff}| = \frac{2mcs}{eL}\Omega \ , \tag{3.6}$$

where L is the interferometer perimeter and the direction of $\mathbf{A}_{eff}$ is parallel to the particle trajectory. According to this analogy, the Hamiltonian of a massive particle in a rotating frame is given by

$$\hat{H} = \frac{1}{2m}(\hat{\mathbf{P}} - \frac{e}{c}\mathbf{A}_{eff})^2 = \frac{1}{2m}(\hat{\mathbf{P}} - \hbar\frac{\phi}{L})^2 \ , \tag{3.7}$$

where its eigenstates are the momentum ($\hat{\mathbf{P}}$) eigenstates. In a closed rotating ring the momentum operator eigenvalues are given by $P = \hbar(\frac{2n\pi}{L} - \frac{\phi}{L})$ and therefore the eigen energies are given by

$$E_n = \frac{\hbar^2}{2m}(\frac{2n\pi}{L} - \frac{\phi}{L})^2 \ . \tag{3.8}$$

In chapter 4 we will see that the eigenenergies define the transmission resonance location in an open ring geometry at the limit in which the particle has high probability to complete many full cycles.

3.2. Scattering-Matrix Formalism

Similarly to quantum electronics where electrons are manipulated inside semiconductor structures, in atom optics, atoms move inside waveguide structures and are manipulated using potentials where at least one dimension is comparable to the de Broglie wavelength of the atoms. Let us denote a guiding potential where a particle moves in by $U(y, z)$, where the particle is free to propagate in the longitudinal (x) and it is confined in the transverse dimensions (y, z). Since the transverse dimensions have a finite size the transverse energy

is quantized and each state of the energy defines a transverse mode. The wavefunction of a transverse mode j and energy E_j can be written as a product of $\psi_j(y,z)e^{ikx}$, where $\psi_j(y,z)$ is the eigenstate of the transverse Hamiltonian.

A symmetrically splitting of the atom guiding potential into two identical output guides forms a Y beam splitter, as seen in Fig 28, where a coherent beam-splitter can be characterized by a scattering matrix that relates the outgoing wave amplitudes to the incoming wave amplitudes at the different channels [32]. More specific, if there are three single-mode channels, we can write

$$\begin{pmatrix} b_1 \\ b_2 \\ b_3 \end{pmatrix} = \begin{pmatrix} s_{11} & s_{12} & s_{13} \\ s_{21} & s_{22} & s_{23} \\ s_{31} & s_{32} & s_{33} \end{pmatrix} \cdot \begin{pmatrix} a_1 \\ a_2 \\ a_3 \end{pmatrix} , \tag{3.9}$$

where a_i are the amplitudes of the incoming wave, b_i are the amplitudes of the outgoing wave and s_{ij} is the transmission amplitude between a_j and b_i. At any given energy E, we will denote the number of propagating modes at channel p by $M_p(E)$. The total number of modes is obtained by summing the number of modes in each channel

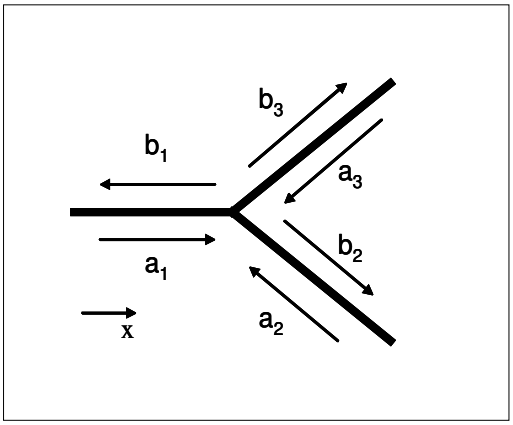

FIG. 28: A scheme of a one dimensional beam-splitter. In such a beam-splitter there is only single mode of the energy in each channel

$$M_T(E) = \sum_p M_p(E). \tag{3.10}$$

The scattering matrix is of dimensions $M_T \times M_T$.

In principle we can calculate the S-matrix starting from the *Schrödinger* equation

$$\left[\frac{(i\hbar\nabla + \frac{e}{c}\mathbf{A}_{eff})^2}{2m} + U(x,y,z)\right]\Psi(x,y,z) = E\Psi(x,y,z)\ ,$$

if we know the effective vector potential $\mathbf{A}_{eff}$ (see Eq.(3.6)) and the potential energy U(x,y,z) at the junction. This could be achieved by calculating the overlap between the eigenstates in different sides of the waveguide. The transmission probability T_{mn} is obtained by taking the squared magnitude of the corresponding element of the S-matrix,

$$T_{m\leftarrow n} = |S_{m\leftarrow n}|^2\ . \tag{3.11}$$

In order to ensure current conservation the S-matrix must be unitary. We can write in matrix notation

$$\{b\} = [S]\{a\}\ , \tag{3.12}$$

where the matrix $[S]$ has dimensions $M_T \times M_T$ being the total number of modes in all the channels, while $\{a\}$ and $\{b\}$ are column vector representing the incoming and outgoing wave amplitudes in the different modes in the channels. We assume that the incoming and outgoing currents in a particular mode m are proportional to the squared magnitudes of the corresponding mode amplitudes a_m and b_m respectively. Current conservation then requires that

$$\sum_m |a_m|^2 = \sum_m |b_m|^2 \ ,$$

that is,

$$\{a\}^\dagger\{a\} = \{b\}^\dagger\{b\} \ . \tag{3.13}$$

Substituting Eq.3.12 into Eq.3.13 we obtain

$$\{a\}^\dagger\{a\} = \{Sa\}^\dagger\{Sa\} = \{a\}^\dagger[S]^\dagger[S]\{a\} \ . \tag{3.14}$$

Hence

$$[S]^\dagger[S] = I \ , \tag{3.15}$$

so in terms of the elements of the S-matrix we have

$$\sum_{m=1}^{M_T} |S_{mn}|^2 = 1 \ , \tag{3.16}$$

The general S matrix of a three channel junction (Y shaped-junction) depends on twelve parameters and given by

$$\hat{S} = \begin{pmatrix} r_{11} & t_{12} & t_{13} \\ t_{21} & r_{22} & t_{23} \\ t_{31} & t_{32} & r_{33} \end{pmatrix} \ , \tag{3.17}$$

where $[S]^\dagger[S] = I$ and t_{ij}, r_{ij} are complex numbers. In a coherent microscopic system we

can assume that there is time reversal symmetry where $t \rightarrow -t$ and $k \rightarrow -k$. In a beam splitter it means that a particle that passes from channel i to channel j suffer the same phaseshift as a particle that passes from channel j to channel i, i.e $t_{ij} = t_{ji}$ [33, 34]. Under the assumptions that the junction is not fully symmetric i.e. $t_{12} = t_{13} \neq t_{23}$, as seen in Fig.(29), the scattering matrix depends on eight parameters and becomes into

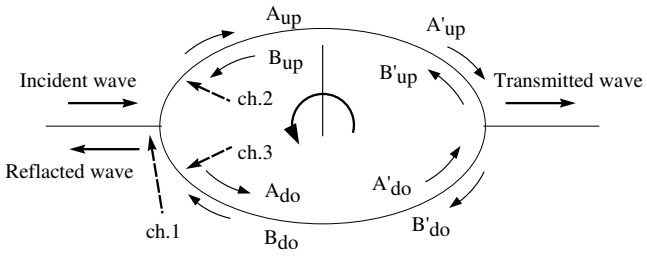

FIG. 29: A schematic representation of an asymmetric double Y junction rotating interferometer where the transmission amplitude (TA) between ch.1 and ch.2 is equal to the TA between ch.1 and ch.3 but is not equal to the TA between ch.2 and ch.3

$$\hat{S} = \begin{pmatrix} r_1 & t_1 & t_1 \\ t_1' & r & t \\ t_1' & t & r \end{pmatrix} , \tag{3.18}$$

3.3. Real Amplitudes Scattering Matrix

Due to the analogy between a massive particle travelling in a rotating frame and a charged particle travelling in a ring with a magnetic flux, a theoretical examination of beam-splitters with similar structure to the electronic case [31] is a natural choice.

Assuming that the transmission and reflection amplitudes are real, one can express the scattering matrix with four parameters and from unitarity consideration it could be expressed in terms of a single parameter, the coupling between the symmetric interferometer arms (internal transmission amplitude), by the following matrix

$$\hat{S} = \begin{pmatrix} 1-2t & \sqrt{2\,t(1-t)} & \sqrt{2\,t(1-t)} \\ \sqrt{2\,t(1-t)} & -(1-t) & t \\ \sqrt{2\,t(1-t)} & t & -(1-t) \end{pmatrix} . \tag{3.19}$$

Mathematical description of the transmission in a Double-Y interferometer could be given from the solution of this set of equation

$$\hat{S}.\begin{pmatrix} 1 \\ B_{up} \\ B_{do} \end{pmatrix} = \begin{pmatrix} r_a \\ A_{up} \\ A_{do} \end{pmatrix} \;,\quad \hat{S}.\begin{pmatrix} 0 \\ A'_{up} \\ A'_{do} \end{pmatrix} = \begin{pmatrix} t_a \\ B'_{up} \\ B'_{do} \end{pmatrix} \;, \tag{3.20}$$

where $A', B', A, B_{up,do}$ are the internal amplitudes (see Fig.(29)), t_a is the total transmission amplitude and r_a is the total reflection amplitude. Using the relations,

$$\begin{aligned} A'_{up} = A_{up}e^{i(k-\frac{\phi}{L})\frac{L}{2}} \quad,\quad A'_{do} = A_{do}e^{i(k+\frac{\phi}{L})\frac{L}{2}} \;, \\ B'_{up} = B_{up}e^{i(k+\frac{\phi}{L})\frac{L}{2}} \quad,\quad B'_{do} = B_{do}e^{i(k-\frac{\phi}{L})\frac{L}{2}}, \end{aligned} \tag{3.21}$$

where k is the particle momentum, L is the interferometer perimeter and ϕ is the effective flux, we obtain the following equations,

$$\hat{S}\cdot\begin{pmatrix} 1 \\ B_{up} \\ B_{do} \end{pmatrix} = \begin{pmatrix} r_a \\ A_{up} \\ A_{do} \end{pmatrix} \quad,\quad \hat{S}\cdot\begin{pmatrix} 0 \\ A_{up}e^{i(k-\frac{\phi}{L})\frac{L}{2}} \\ A_{do}e^{i(k+\frac{\phi}{L})\frac{L}{2}} \end{pmatrix} = \begin{pmatrix} t_a \\ B_{up}e^{i(k+\frac{\phi}{L})\frac{L}{2}} \\ B_{do}e^{i(k-\frac{\phi}{L})\frac{L}{2}} \end{pmatrix} . \tag{3.22}$$

A solution for this set yields the total transmission amplitude, t_a and the transmission, i.e. the probability of a particle to exit the interferometer is given by $T = |t_a|^2$.

3.4. Horizontal Complex Amplitudes Beam-Splitter

There are experimental limitations to realizing a Y (3 port) beamsplitter in matter waves (e.g. via light or magnetic fields). In any case, as may be seen from the scattering matrix in the previous section, such a beam splitter induces uncontrolled inherent reflection to preserve unitarity. The beam splitter described in the previous sections was motivated by interferometers realized for electrons in conductors. An alternative approach would be to design matter wave beam splitters based of the optical analogue having 4 ports (rather than 3 above). Such an X beam splitter is the topic of the following sections.

As we would like to continue to focus on 3 port junctions, we will in the following analyze an X beamsplitter with a "mirror" in front of one of the channels. In such of atomic beam splitter a potential barrier splits an atomic beam into two trajectories , as seen in Fig.(30).

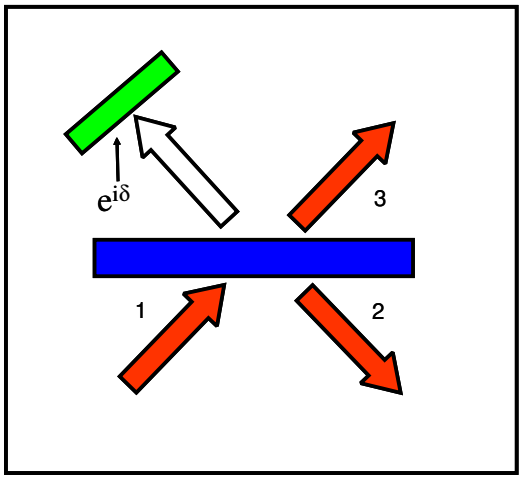

FIG. 30: A scheme of a horizontal complex amplitudes beam splitter. The reflection amplitude of the mirror (green) in channel 4 and the distance between the potential barrier (blue) and the mirror defines the geometric phase δ.

A beam that comes from channel 1 can either be transmitted to channel 3 with amplitude t or reflected to channel 2 with amplitude r. A beam that comes from channel 2 can be either reflected to channel 1 or transmitted to channel 4, reflect back by the mirror while accumulating a geometrical phase and transmitted back to channel 2 or reflected to channel 3. A beam that comes from channel 3 can be either transmitted to channel 1 or reflected to channel 4, reflect back by the mirror and reflected back to channel 3 or transmitted to

channel 2. It can be shown that the S-Matrix for the outputs of channels 1,2,3 in terms of the inputs at the same channels is given by (see Appendix A)

$$\hat{S} = \begin{pmatrix} 0 & r & t \\ r & t^2 e^{i\delta} & rte^{i\delta} \\ t & tre^{i\delta} & r^2 e^{i\delta} \end{pmatrix} . \tag{3.23}$$

From the demand for unitarity we obtain that $|t|^2 + |r|^2 = 1$ and $r^* t + t^* r = 0$. By rewriting the second condition in terms of absolute value and phase we obtain, $2|r||t|\cos[\beta - \alpha] = 0$, i.e. this conditions implies that there is always a phase difference of $\frac{\pi}{2}$ between r and t. We may assume that t is real and then r is pure imaginary, in particular we discuss the case where $t = \frac{1}{\sqrt{2}}$, in order to obtain a symmetric beam splitter. This choice results in the S-matrix

$$\hat{S} = \begin{pmatrix} 0 & \frac{i}{\sqrt{2}} & \frac{1}{\sqrt{2}} \\ \frac{i}{\sqrt{2}} & \frac{1}{2}e^{i\delta} & \frac{i}{2}e^{i\delta} \\ \frac{1}{\sqrt{2}} & \frac{i}{2}e^{i\delta} & -\frac{1}{2}e^{i\delta} \end{pmatrix} . \tag{3.24}$$

There are two options to configure this interferometer. In the symmetric configuration the mirror ports are set in the same direction, e.g. in the "upper" part of the the interferometer, in both sides of the interferometer, as seen in Fig. (31 a). A particle that travels in the "lower" part accumulates a phase of $e^{i\pi}$ due to reflections and the total transmission will be zero for $\phi_{eff} = 0$ and 1 for $\phi_{eff} = \pi$. In the anti-symmetric configuration the mirror ports are set in opposite directions in both sides of the interferometer, as seen in Fig. (31 b). The total transmission will be 1 for $\phi_{eff} = 0$ and zero for $\phi_{eff} = \pi$, similar to the real amplitudes case.

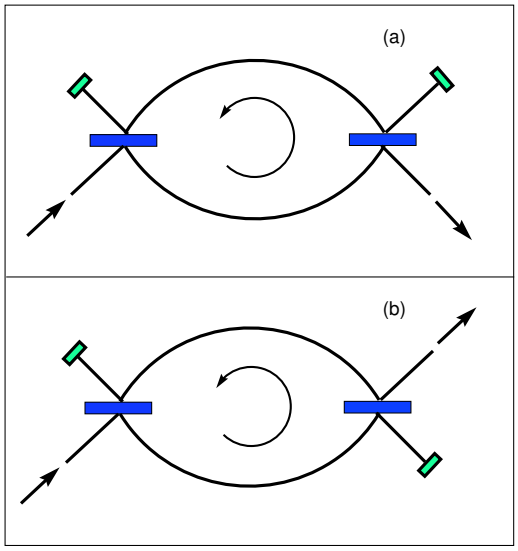

FIG. 31: (a) The mirror ports set in the same direction on both sides of the interferometer. (b) The mirror ports set in opposite directions on both sides of the interferometer.

3.5. Vertical Complex Amplitudes Scattering Matrix

Similarly configured to the horizontal beam splitter, is the vertical beam splitter. Unlike the horizontal configuration, this configuration allows symmetric scattering between port 2 and 3 and a multipath trajectory inside an interferometer constructed from two horizontal beam splitters. A scheme of the horizontal beam splitter is seen in Fig.(32).

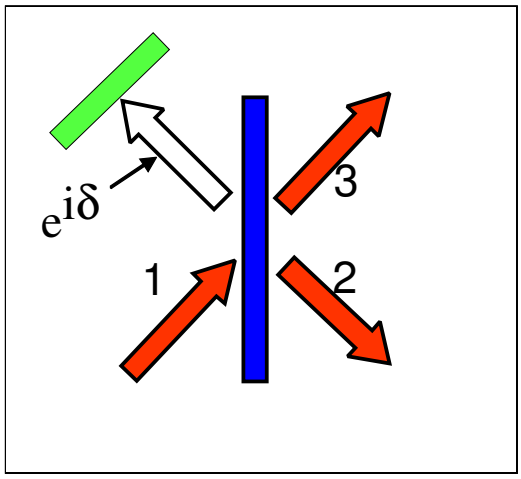

FIG. 32: A scheme of a vertical complex amplitudes beam splitter.

A beam that comes from port 1 can either be transmitted to port 3 with amplitude t or

reflected to port 4 with amplitude r. The reflected beam accumulates a phase of $e^{i\delta}$ and can either be reflected back to port 1 with amplitude r or transmitted to port 2. A beam that comes from port 2 can be either reflected to port 3 or transmitted to port 4. The transmitted beam accumulates a phase of $e^{i\delta}$ and can either be reflected back by the mirror to port 1 with amplitude r or transmitted to port 3 with amplitude t. A beam that comes from port 3 can be either transmitted to port 1 with amplitude t or reflected to port 2 with amplitude r. It can be shown that the S-Matrix for the outputs of ports 1,2,3 in terms of the inputs at the same ports is given by

$$\hat{S} = \begin{pmatrix} r^2 e^{i\delta} & rte^{i\delta} & t \\ rte^{i\delta} & t^2 e^{i\delta} & r \\ t & r & 0 \end{pmatrix} . \tag{3.25}$$

From the demand for unitarity we obtain the same conditions like in the vertical configuration. Under the assumption that r is real (and then t is pure imaginary) and by using the first condition we obtain the relation between r and t. In this case the S-matrix becomes into

$$\hat{S} = \begin{pmatrix} e^{i\delta} r^2 & i\ e^{i\delta} r\sqrt{1-r^2} & i\sqrt{1-r^2} \\ i\ e^{i\delta} r\sqrt{1-r^2} & e^{i\delta}(-1+r^2) & r \\ i\sqrt{1-r^2} & r & 0 \end{pmatrix} . \tag{3.26}$$

Setting $r \to 1$, implies $|\hat{S}_{12}| \approx |\hat{S}_{13}|$, and a multipass trajectory with a symmetric scattering between port 2 and 3 is achieved. A scheme of this interferometer is shown in Fig.(33)

3.6. Noise and Gyroscope Units

In our model we treat the atoms as quantum (rather than classical) particles, which are represented by a continious wave function. The square amplitude of the transmitted wave is the *probability* of an atom to exit the interferometer. On the other hand, in

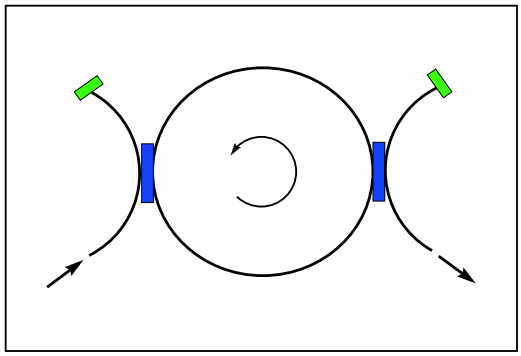

FIG. 33: A scheme of a vertical complex amplitudes interferometer.

a real experiment, we measure the atoms as classical discrete particles. Therefore, by measuring the numbers of atoms passing a point in the interferometer and detecting the number of atoms at the exit of the interferometer, for some time interval, one would expect to count a different number of atoms in one time interval versus the next. It is impossible to predict the motion of individual atom, but it is possible to calculate the average number of atoms drifting past a particular point per time interval. The variation about the mean value or average of these quantity is the noise. Shot-noise is due to the corpuscular nature of transport and it is always associated with direct particles current flow. In fact, it is required that there be direct current flow or there is no shot-noise. Generally, in order to discern shot-noise, a particle that enters the detection point must do so as a purely random event and independent of any other atom crossing this point. Since the events are random and independent, Poisson statistics describe this process.

Short-term sensitivity (STS) define the ability to detect small rotations over short time scales. It depends on interferometer area, the mass of the atom and on signal-to-noise ratio (SNR). Gyroscope sensitivity is typically referred in units of $(rad/sec)/\sqrt{Hz}$. These units signify a rotation rate (rad/sec) measurement that is presumed to be limited by shot-noise. In such a case the shot-noise is an intrinsic noise of the system and it is impossible to overcome it, unlike fluctuations from external sources/fields which, theoretically, could be screened. As stated, shot-noise processes obey Poisson statistics with standard deviation equal to $\sqrt{N}$ of the number of particles, and the total number of particles in the signal increases linearly with time. Therefore,a shot-noise-limited signal improves like $\sqrt{t}$ with

integration time t. Dividing by $\sqrt{Hz}$ normalizes the result by the measurement bandwidth, yielding the sensitivity in 1 second.

To present rotation sensitivity as a function of system parameters and its relation to the SNR, let us express the change in the number of atoms that exit the interferometer due to rotations in the form:

$$\Delta N_{out} = \frac{\Delta N_{out}}{\Delta\Omega}\Delta\Omega \ . \tag{3.27}$$

In order to notice any changes in the number of atoms that exit the interferometer, we demand that any change will be larger than the noise of the system. Since the noise in a shot-noise limited system is Poissonian, we demand that,

$$\frac{\Delta N_{out}}{\Delta\Omega}\Delta\Omega \geq \sqrt{N_{out}} \ , \tag{3.28}$$

and the STS is given by

$$\Delta\Omega = \frac{\sqrt{N_{out}}}{\frac{dN_{out}}{d\Omega}} = \frac{\sqrt{N_{out}}}{\frac{dN_{out}}{d\phi}\frac{d\phi}{d\Omega}} \ . \tag{3.29}$$

This derivation is with analogy to Gustavson's derivation [26] as explained at Appendix B. By substituting $N_{out} = N_{in}\,T$, where N_{in} is the incoming atomic flux and T is the interferometer transmission Eq.(3.29) becomes

$$\Delta\Omega = \frac{1}{\sqrt{N_{in}}\frac{d\phi}{d\Omega}}\frac{\sqrt{T}}{\frac{dT}{d\phi}} = \frac{\Delta\phi}{\sqrt{N_{in}}\frac{d\phi}{d\Omega}} \ , \tag{3.30}$$

where $\Delta\phi \equiv \frac{\sqrt{T}}{\frac{dT}{d\phi}}$ is the intrinsic sensitivity of the interferometer and it depends only on the beamsplitter characteristics.

3.7. Coherence length

An incident particle flux with spectral width Δ_k may be viewed as a statistical mixture of wavepackets with random initial phases and/or random initial locations, such that interference occurs only if the path difference is smaller than the coherence length $\Delta_x = 1/\Delta_k$ [35].

A Fourier integral representation of one-dimensional wave-packet is given by

$$\psi(x) = \int_{-\infty}^{\infty} a(k) e^{ikx} dk \ , \tag{3.31}$$

assuming Gaussian momentum distribution $\psi(x)$ becomes

$$\psi(x) = \frac{A}{\sqrt{2\pi}\Delta_k} \int_{-\infty}^{\infty} \exp\left[-\frac{(k-k_0)^2}{2\Delta_k^2}\right] e^{ikx} dk \ , \tag{3.32}$$

where the mean wavenumber $\langle k \rangle = k_0$ and Δ_k is the standard deviation of k. We change variables to $k' \equiv k - k_0$, $u \equiv \frac{k'}{\sqrt{2}\Delta_k}$ and $z \equiv u - \frac{i\Delta_k x}{\sqrt{2}}$, to obtain

$$\psi(x) = A \exp\left[-\frac{x^2}{2\Delta_x^2}\right] e^{ik_0 x} \ . \tag{3.33}$$

The requirement for normalization $\int \psi^* \psi dx = 1$ provides the value of A

$$A = \sqrt{\frac{\Delta_k}{\sqrt{\pi}}} = \sqrt{\frac{1}{\Delta_x \sqrt{\pi}}} \ . \tag{3.34}$$

In an un-revolving interferometer with different internal channel length, as sketched in Fig. 34, the length difference between the internal channels $\Delta_L = |L_2 - L_1|$ must be much smaller than Δ_x or the spatial overlap of the wave contributions will go down to zero and no interference will occur (this statement still holds even after the time evolution has made the wave packets broader).

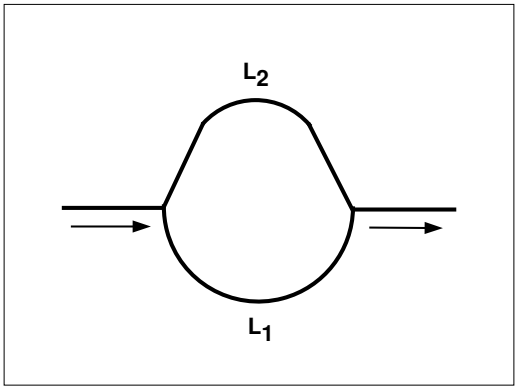

FIG. 34: A scheme of an interferometer with different internal channel length.

In terms of phases this condition becomes $k|L_2 - L_1| \ll k\Delta_x$.

3.8. The Relation Between the Finesse and the Average Number of Cycles

The Sagnac phase difference is accumulated along the arms of a revolving interferometer and as arises from Eq.(1.9) it is proportional to the interferometer area. We expect that increasing the number of full cycle trajectories transversed by the particle, will increase the interferometer sensitivity or alternatively allow to reduce the interferometer area while maintaining the same sensitivity of a larger area single pass interferometer.

In the high finesse limit where we can neglect back reflections inside the interferometer loop (i.e. $t \to 1$ in the real amplitudes model and $r \to 1$ in the vertical complex model), the probability of a particle to complete N cycles in the interferometer is t^{4N}. The normalized probability to complete up to N cycles is given by

$$P(N) = (1 - t^4) \sum_{n=0}^{N} t^{4n} \ , \tag{3.35}$$

(normalized, i.e. $P(N \to \infty) \to 1$) and the average number of cycles is given by

$$\langle N \rangle = (1 - t^4) \sum_{n=0}^{\infty} n\, t^{4n} = \frac{t^4}{1 - t^4}. \tag{3.36}$$

Alternatively, the distance between adjacent transmission peaks is called the free spectral range (FSR) and as will be shown in the results chapter, in our case it is given by

$$\Delta_{FSR} = \frac{2\pi}{L}. \tag{3.37}$$

The FSR is related to the full-width half-maximum, Δ_k, of any one transmission peak by a quantity known as the finesse

$$\mathcal{F} = \frac{\Delta_{FSR}}{\Delta_k}. \tag{3.38}$$

In the real amplitude $t \to 1$ model, Δ_k is given by

$$\Delta_k = \frac{4(1-t)}{L\,t}, \tag{3.39}$$

and the finesse is given by

$$\mathcal{F} = 2\pi \frac{t}{4(1-t)}. \tag{3.40}$$

Up to a 2π factor, the leading order of the Taylor expansion (around $t \to 1$) is equal to $\frac{1}{4(1-t)}$ for both $\mathcal{F}$ or $\langle N \rangle$, i.e. these quantities scale similarly as t becomes closer to one.
In practice the number of cycles is limited by experimental and technological limitations as will be shown in the next section. In addition, the number of cycles is limited by the required band width or response time of the sensor. The larger the finesse the longer the response time will be as at any given time, the interferometer transmission will still be affected by a phase accumulated previously under a different angular velocity.

3.9. Experimental Limitation on the Interferometer Parameters

The approximated average life time of an atom in an ultra high vacuum chamber (10^{-10} Torr) is about $\tau = 10sec$ due to background gas collisions. The maximal atom velocity is limited by the interferometer curvature. For example, if the atom is guided in the interferometer under the influence of a magnetic potential, the resultant force, which keeps the atoms in the radial axis, should be larger than the centrifugal force

$$\mu_B \nabla B > m\frac{v^2}{r} \tag{3.41}$$

where μ_B is the Bohr magneton, B is the magnetic field, v is the atom velocity, m is its mass and r is radius of the interferometer. From Eq.(3.41) we obtain

$$v < \sqrt{\frac{\mu_B \nabla B r}{m}}\ . \tag{3.42}$$

For Cs atom moving in an interferometer with a radius of $2.6\,mm$ (for this radius the area is equal to the area of the Stanford atom interferometer) and with a feasible experimental magnetic gradient of $\approx 10^3 \frac{T}{m}$, the maximal velocity is $\approx 10 \frac{m}{sec}$. Considering the life-time of the atom and its velocity we obtain that the maximal path inside the interferometer is $d \approx 100m$. This path is also equal to the number of cycles times the interferometer perimeter $d = N\,2\pi r$. The geometrical limitation on the radius minimization is due to the resolution of the chip fabrication and the limitations on the radius maximization is due to chip size. In order to achieve high finesse the interferometer radius should be decreased, but as we see in Eq.(3.30) the sensitivity scales like $\frac{1}{r^2}$, and hence we should choose a large interferometer radius. In the case of $r = 2.6\,10^{-3}\,m$ the estimated average number of cycles in the interferometer is

$$\langle N \rangle = \frac{v\,\tau}{2\,\pi\,r} \approx 6000 \ , \tag{3.43}$$

and each cycle takes

$$\tau_0 = \frac{2\,\pi\,r}{v} \approx 1.5\,10^{-3}\,sec \ . \tag{3.44}$$

By substituting $\langle N \rangle = 6000$ into Eq.(3.36) we find the matrix parameter $t = 0.99996$ which satisfies this equation. This rough estimation can be made more precise by taking in account the exact expression for the trapped atom life time due to background gas collisions. We then find the probability to be

$$P(N) = (1 - t^4) \sum_{n=0}^{N} t^{4n} \, \exp[-n \frac{\tau_0}{\tau}] \ , \tag{3.45}$$

where $P(\infty) \neq 1$ due to the atom collisions with the background gas inside the interferometer. The average number of cycles is then given by

$$\langle N \rangle = (1 - t^4) \sum_{n=0}^{\infty} n\,t^{4n} \, \exp[-n \frac{\tau_0}{\tau}] = \frac{\exp[\frac{\tau_0}{\tau}]\,t^4(1 - t^4)}{(\exp[\frac{\tau_0}{\tau}] - t^4)^2} \ . \tag{3.46}$$

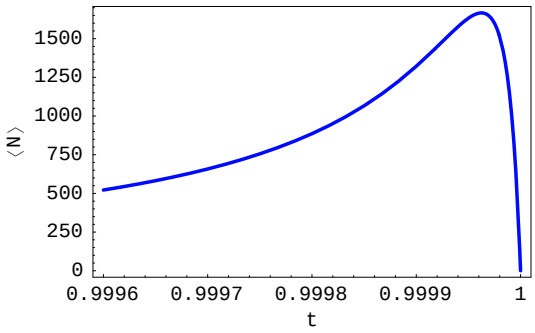

FIG. 35: Average number of cycles vs the matrix parameter t.

The maximal average number of cycles $\langle N \rangle \approx 1650$ is achieved around $t = 0.99996$, as seen in Fig.(35).

4. RESULTS

In this chapter we present the results of the model, i.e. the solutions for the equations given in chapter 3 for different beam splitters. The chapter is organized as follows. In Section 4.1 we describe in general terms the expected transmission of an interferometer based on a real amplitudes beam splitter (see section 3.3). In sections $4.2-4.4$ we present in detail the expected transmission and the expected sensitivity for three different regimes of the matrix parameter t (see Eq.3.19): $t \ll 1$, $t = \frac{1}{2}$ and $t \to 1$. In section 4.5 we incorporate the results of sections $4.2-4.4$ to obtain the main result of this chapter, an expression for the sensitivity for any matrix parameter t, as a function of the incoming particle flux, the atomic mass and the interferometer area. In this section, we verify the assumption that the high finesse interferometer will allow to reduce the interferometer's size while still achieving high sensitivity. In section 4.6 we present the expected transmission and the expected sensitivity for an interferometer based on an horizontal, complex amplitudes, beam splitter (see section 3.4) and in section 4.7 we present the results for a vertical, complex amplitudes, beam splitter (see section 3.5), which is perhaps the most experimentally feasible on an atom chip among the interferometers described in chapter 3.

We note that in most sections of this chapter, the main numerical results (sensitivity results) are calculated using the parameters reported in Gustavson's thesis [26]: $N_{in} = 1.6\,10^{10}\,\frac{atom}{sec}$, $m = 2.2\,10^{-25}\,kg$ (Cesium atom) and $r = 2.6\,10^{-3}\,m$, which allows for a comparison between the results presented here and those of up-to-date experiments.

4.1. The Transmission of an Interferometer Based on a Real Amplitudes Beam-Splitter

In this section we give a short description of the transmission of an interferometer based on a real amplitude beam splitter. A more detailed description will be given in sections $4.2-4.4$.

Recalling Eq.(3.19) we notice that the matrix parameter t governs the behavior of the particle at the beam splitter. For $t \ll 1$, there is high reflectivity at the junction, while for

$t \to 1$, the particle has a high probability to be transmitted from one internal loop channel to the other internal channel, i.e. from channel 2 to channel 3 and vice versa. Solving Eq.(3.22) results in the wave amplitudes at the interferometer, and in particular we obtain the total transmission amplitude of the interferometer, t_a, where a general expression for the interferometer transmission is given by

$$T = |t_a|^2 = \frac{16(1-t)^2 t^2 \cos^2\left(\frac{\phi}{2}\right) \sin^2\left(\frac{kL}{2}\right)}{\left((1-t)^2 + (-1+2(1-t)t)\cos(kL) + t^2\cos(\phi)\right)^2 + 4(1-t)^2 t^2 \sin^2(kL)} \quad (4.1)$$

The interferometer transmission has a $\frac{2\pi}{L}$ period and it strongly depends on the parameter t and we can distinguish between three major regimes of t, $t \ll 1,\ t = \frac{1}{2},\ t \approx 1$. In Fig.(36) we present a few representative examples at certain values. For $t \ll 1$, the probability of an atom to travel forward and backward is large, while the probability to complete a full cycle or exit the interferometer is small. On the other hand, we know that the eigenvalues of the momentum in a ring geometry are given by $k = \frac{2n\pi}{L}$. Thus, unless $kL(mod\ 2\pi) \leq t$, i.e interference occurs despite the low probability to exit the interferometer, the transmission at this regime is small with respect to the other regimes (Fig.(36a,b)), and it becomes smaller, down to zero, as ϕ becomes larger between $0 < \phi < \pi$ and vice versa between $\pi < \phi < 2\pi$. From inspecting the scattering matrix, it is clear that for $t = \frac{1}{2}$ the probability of a particle to be reflected at the entrance of the interferometer (for instance, the left beam splitter in Fig 29) is equal to zero, thus, the particle must enter the interferometer. At the right beam splitter the particle could exit the interferometer, it could also be reflected back to the same channel, or it could be internally transmitted to the second channel, with opposite amplitude. This leads to a fully destructive interference at the left beam splitter and to a single path trajectory. At $\phi = 0$, this behavior of the particle manifests itself by unity transmission for every k. As ϕ increases, periodic narrow dips appear, located at $k = \frac{2n\pi}{L}$. These dips become wider and the transmission becomes smaller as ϕ is getting larger,as seen in Fig(36c,d). Recall Eq.(3.19) we notice that for $t \approx 1$, the term $\hat{S}_{11} = 1 - 2\,t$ implies a low probability to enter the interferometer. On the other hand, the terms $\hat{S}_{23,32} = t$ implies that once the particle enters the interferometer it has high probability to complete many

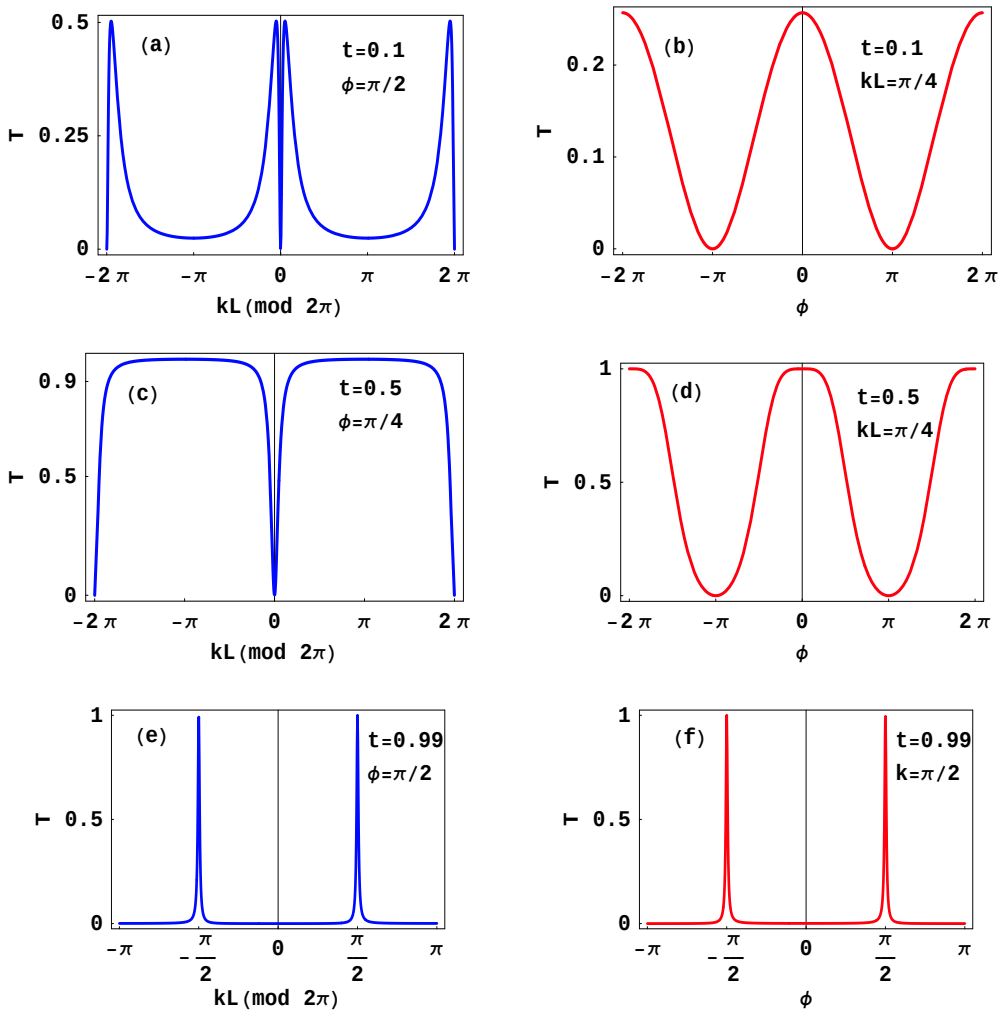

FIG. 36: The transmission of an interferometer at a few representative regimes. (a) At $t \ll 1$ and $\phi \neq 0$ the transmission curve is double peaked. As ϕ is getting larger the transmission is getting smaller. (b) $t \ll kL \pmod{2\pi}$ i.e. reflection effects are stronger than interference effects. Thus, the transmission vs ϕ is poor. (c) At $t = \frac{1}{2}$, and $\phi = 0$, the transmission is equal to unity for every k. As ϕ increases, periodic narrow dips appear, located at $k = \frac{2n\pi}{L}$. These dips become wider and the transmission becomes smaller as ϕ is getting larger. (d) For $kL \neq 2n\pi$ and around $\phi = 0$ the transmission is ≈ 1 and small change in ϕ causes a small change the transmission. (e,f) At $t \approx 1$, the probability of an atom to travel along a large number of cycles is high. Thus, the phase difference between a clockwise trajectory and a counter-clockwise trajectory is large. The transmission curve characterized by narrow peaks due to this phase shift and any small displacement from resonance causes a destructive interference and the transmission goes to zero.

full cycle passes, while the probability to be reflected back to the origin channel is very small. This motion could be approximated by a motion of a particle in a closed ring. Recall Eq.(3.8) we obtain that, in this regime, the location of the peaks is given by

$$k_n = \frac{2n\pi}{L} \pm \frac{\phi}{L}, \tag{4.2}$$

as seen in the inset of Fig.(38b). At $\phi = 0$ the transmission curve is single peaked periodic Lorentzian shape with peaks at $k = \frac{2n\pi}{L}$. As ϕ increases, the lineshape transforms into two separated peaks as seen in Fig.(36e, f).

The transmission maximal value along k depends on two factors, the matrix parameter t and the effective flux $\phi = \frac{2ms}{\hbar}\Omega$ (see Eq.(3.5)). In Fig(37) we see that the maximal value becomes smaller, down to zero, as t becomes smaller and ϕ becomes closer to π. The maximal transmission value dependence on t is symmetric around $\phi = \pi$, where the transmission is zero for every t.

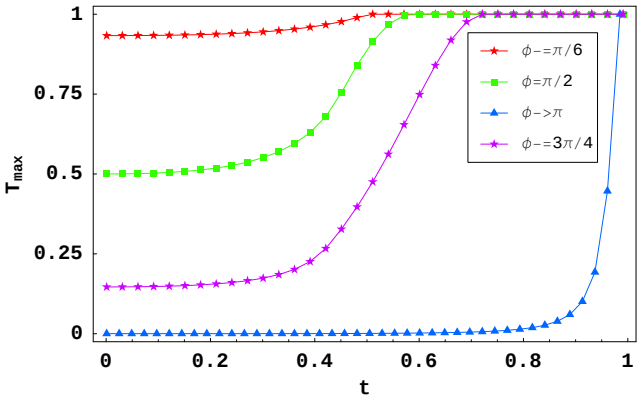

FIG. 37: Transmission maximal values of interferometer with radius of $r = 500\ \mu m$ vs the parameter t, for different $\phi's$. For small ϕ and $t \geq \frac{1}{2}$ the maximal transmission value is 1, this value decreases a little. As ϕ increases the decrease in the maximal value occurs at larger t. At $\phi \to \pi$ the transmission is very low for $t < 1$ and a maximal transmission value of 1 achieved only for $t \to 1$.

By taking the derivative of the transmission with respect to k, and equating to zero, we obtain the shift of the peak location, relative to $k = \frac{2n\pi}{L}$ at $\phi = 0$, due to rotations

$$\Delta k = \frac{2}{L}\cos^{-1}\left[\sqrt{1 - \frac{t^4\sin^4(\phi)}{2(\cos(\phi)+1)|1-2t|t^2\sin^2(\phi)}}\right]. \tag{4.3}$$

At $t \ll 1$, Δk is very small and hardly changes due to rotations. At this values of t, there is a high probability to follow forward and backward trajectories, thus, the transmission is insensitive to rotations. At $t \to \frac{1}{2}$, Δk rapidly converges to $\frac{\pi}{L}$, due to the forward scattering and backward scattering symmetry, as mentioned above. As t increases towards 1, $\Delta k \to \frac{\pi}{L}$, as seen in Fig.(38).

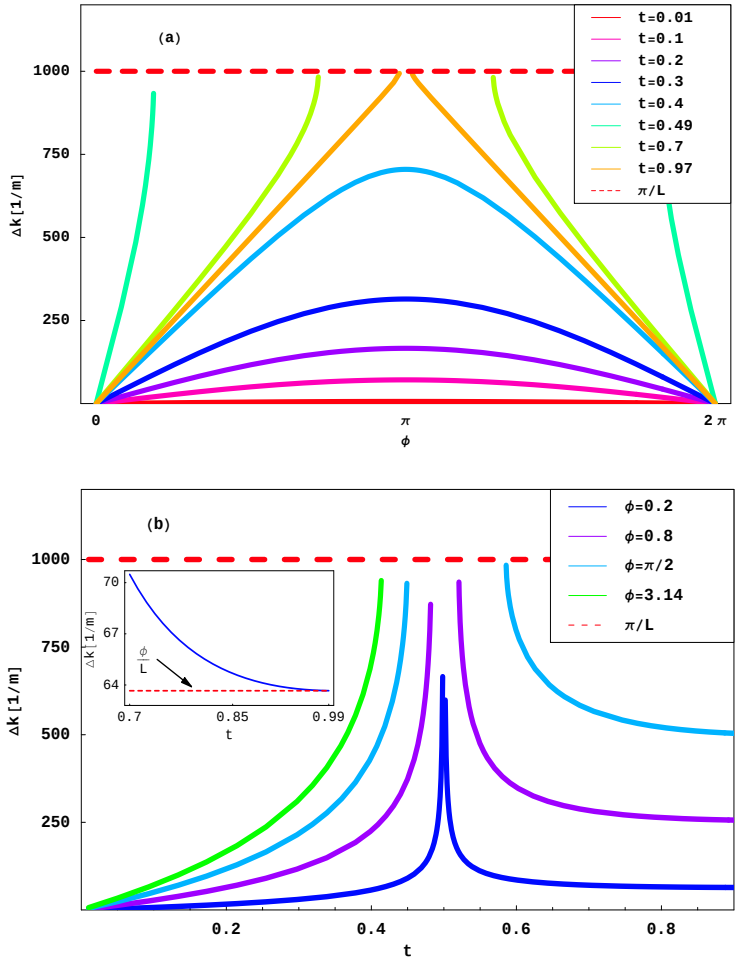

FIG. 38: The peak shift due to rotations in interferometer with radius of $r = 500\ \mu m$. (a) At $t \to \frac{1}{2}$, Δk is rapidly converges to $\frac{\pi}{L}$ and it rapidly converges back to 0 as $t \to 2\pi$. The slope of the orange curve ($t \approx 1$) is $\frac{1}{L}$. (b) For small ϕ, the transmission curve is double peaked around $k = \frac{2\,n\,\pi}{L}$, at a larger range of t, but the peak shift is poor at this range. As ϕ increases the transmission curve is double peaked at a smaller regime of t, but the peak shift is more significant. As ϕ approaches π the transmission is double peaked up to $t \approx 0.4$. At this range, the transmission is very poor, and the transmission curve become rapidly single peaked.

4.2. Interferometer Transmission and Sensitivity Calculation for $t \ll 1$

For $t \ll 1$ the probability to pass from channel to channel is very small compared to the probability of reflection within the channels (see Eq.(3.19)). In other words the particle moves back and forth along a channel without crossing the junction. If t is also much smaller than kL (mod 2π), multi-path interference of waves travelling many times back and forth add up destructively at the output channel. In this case the transmission amplitude (TA) could be approximated by two independent sums over trajectories of each arm of the interferometer

$$\begin{aligned} t_a \approx & \sum_{n=0}^{\infty} \sqrt{2(t-t^2)} \left(\exp\left[i(k-\frac{\phi}{L})\frac{L}{2} \right] \left((t-1)\exp\left[i(k+\frac{\phi}{L})\frac{L}{2} \right] (t-1)\exp\left[i(k-\frac{\phi}{L})\frac{L}{2} \right] \right)^n \right. \\ & \left. + \exp\left[i(k+\frac{\phi}{L})\frac{L}{2} \right] \left((t-1)\exp\left[i(k-\frac{\phi}{L})\frac{L}{2} \right] (t-1)\exp\left[i(k+\frac{\phi}{L})\frac{L}{2} \right] \right)^n \right) \sqrt{2(t-t^2)} = \\ = & \sum_{n=0}^{\infty} 4(t-t^2)\cos\frac{\phi}{2} e^{ik\frac{L}{2}} (1-t)^{2n} e^{nikL} = \frac{4(t-t^2)\cos(\frac{\phi}{2}) e^{ik\frac{L}{2}}}{1-(1-t)^2 e^{ikL}} \quad , \end{aligned} \tag{4.4}$$

and the transmission is given by

$$T = |t_a|^2 = \frac{16t^2(1-t)^2\cos^2(\frac{\phi}{2})}{1+(1-t)^4-2(1-t)^2\cos(kL)} \approx \frac{16t^2(1-t)^2\cos^2(\frac{\phi}{2})}{2(1-\cos(kL))(1-4t)} \approx \frac{4t^2\cos^2\left(\frac{\phi}{2}\right)}{\sin^2\left(\frac{kL}{2}\right)} \tag{4.5}$$

Under the conditions in which this approximation is valid, the device transmission is poor due to the $\frac{4t^2}{\sin^2(\frac{kL}{2})}$ factor which is very small, as shown in Fig.(39).

If kL (mod 2π) $\leq t \ll 1$, although t is small, multi-path interference of waves travelling many times back and forth add up constructively at the output channel, and the transmission is resonantly shaped with a periodic single peak, as shown in Fig.(40).

Since the transmission depends on the particles momentum we distinguish between three regimes of bandwidth of the momentum.

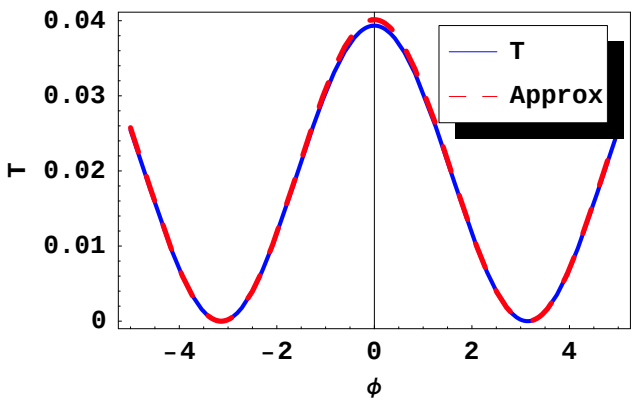

FIG. 39: The transmission *vs* ϕ for $t = 0.01$ and $kL(mod\ 2\pi) = 0.2$. In these conditions multi-path interference of waves travelling many times back and forth add up destructively at the output channel and the transmission is poor. The red dashed line is the approximated transmission.

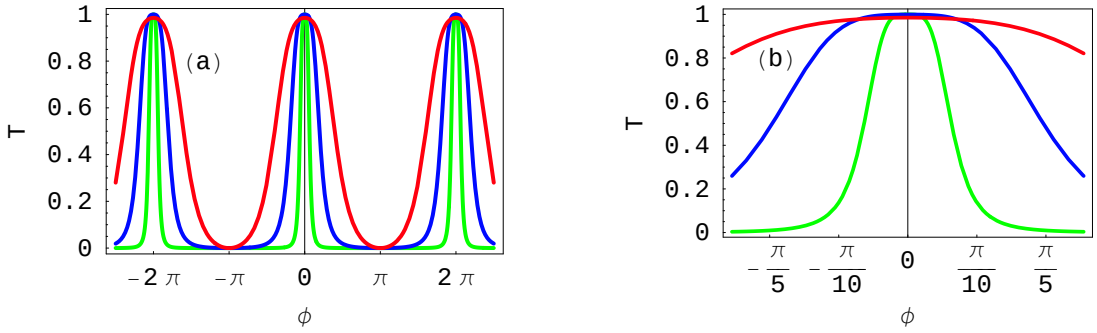

FIG. 40: The transmission *vs* ϕ for $t = 0.01$. The green line is for $kL(mod\ 2\pi) = 0.0001$, the blue line is for $kL(mod\ 2\pi) = 0.001$ and the red line is for $kL(mod\ 2\pi) = 0.005$. In these cases kL (mod $2\pi) \leq t \ll 1$, thus for $\phi = 2\,n\,\pi$, interfering waves add up constructively at the output channel. (a) zoom out,(b) zoom in.

1. Monochromatic input wave

Theoretically, at very low temperatures, the width of the momentum distribution of the atoms Δ_k may be much smaller than the width of the transmission resonance peak Δ_T ($\Delta_k \ll \Delta_T$) and in such a case, we can assume that the incoming wave is monochromatic. The width of Δ_T and its slope depends on $\tilde{\phi} \equiv kL \pmod{2\pi}$, where the peak becomes narrower and the slope becomes steeper as $\tilde{\phi}$ becomes smaller, as shown in Fig.(40). Substituting Eq.(4.1) into Eq.(3.30), results in the sensitivity of the interferometer in this regime. After substituting, one may find the maximal intrinsic sensitivity vs $\tilde{\phi}$ for $t = 0.01$ as shown in Fig.(41) and the location (in ϕ) vs $\tilde{\phi}$ as shown in Fig.(42). Fitting these curves

show that these quantities scale as square root of $\tilde{\phi}$

$$\begin{aligned} \Delta\phi_{max} &= 14.85\tilde{\phi}^{\frac{1}{2}} \quad , \\ \phi_{max} &= 19.89\tilde{\phi}^{\frac{1}{2}} \quad . \end{aligned} \tag{4.6}$$

From this example (note that the coefficient depends on t) we learn that $\Delta\phi_{max} \to 0$, as $\tilde{\phi} \to 0$. In order to achieve momentum distribution narrower than Δ_T it is needed to cool the atoms many orders of magnitude lower than a feasible temperature (See App.C). Therefore, this kind of operation is not applicable.

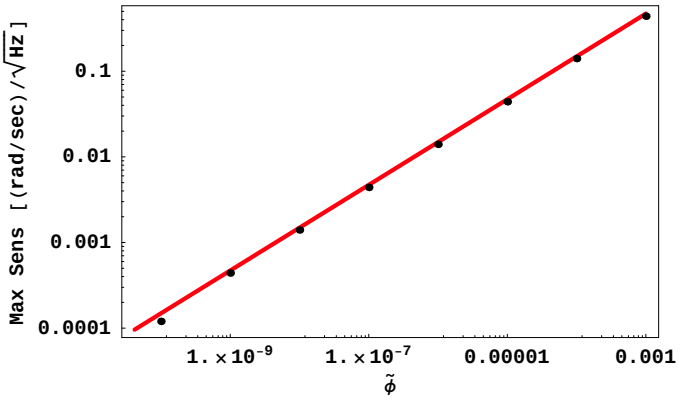

FIG. 41: Logarithmic scale of the maximal intrinsic sensitivity of rotating interferometer with matrix parameter $t = 0.01$ *vs* Log$[\tilde{\phi}]$. The maximal sensitivity goes to zero like the square root of $\tilde{\phi}$.

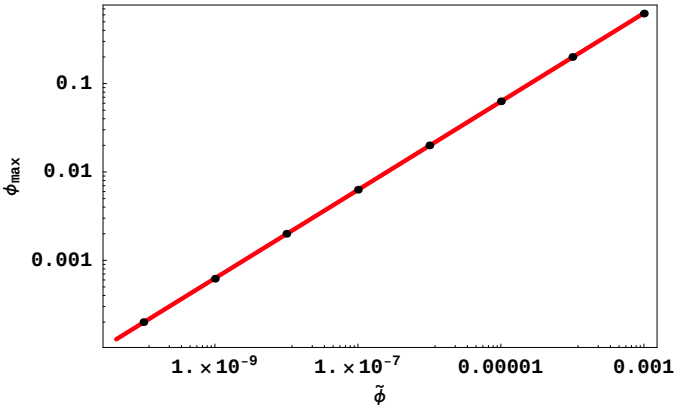

FIG. 42: Logarithmic scale of $\tilde{\phi}_{max}$ *vs* Log$[\tilde{\phi}]$. The location of the maximal sensitivity point goes to zero like the square root of $\tilde{\phi}$.

2. Narrow Band

Another regime is the narrow band regime, where the momentum of atoms entering the interferometer is determined by a Gaussian distribution

$$I_{in}(k) = I_0\ G(k) = I_0 \exp\left[-\frac{1}{2}\left(\frac{(k-k')}{\Delta_k}\right)^2\right] \tag{4.7}$$

(Δ_k is the Gaussian width, $I_0 = \frac{1}{\sqrt{2\pi}\Delta_k}$ and k' is the most probable momentum) and the width of the Gaussian is comparable with the width of the transmission peak, i.e. $\Delta_k \approx \Delta_T$, where $\Delta_T = \frac{4t(1-t)}{L(1-2t)}$ (see derivation in App. D). The number of atoms that exit the interferometer is given by

$$N_{out} \ = \ N_{in} \int_{-\pi/L}^{\pi/L} dk\ I_{in}(k)\ T(k,\phi)\ . \tag{4.8}$$

It is easy to show that an integral of the form (note that $I_{in} \sim L$)

$$I = L \int_{-\pi/L}^{\pi/L} f(k \cdot L) dk, \tag{4.9}$$

is equivalent to

$$I \equiv \int_{-\pi}^{\pi} f(u) du\ , \tag{4.10}$$

where $u \equiv k \cdot L$ and the dependence on L vanishes for any f. For simplicity and due to periodicity of the transmission we may assume that $k' = 0$. A numerical integration for $\Delta_k = \Delta_T$, where $t = 0.01$ and $L = 2\,\pi\,2.6\,10^{-3}\,mm$, is given in Fig.(43).

To this numerical integration one can fit an approximate analytical solution

$$N_{out}/N_{in} \approx \frac{2}{3}\cos[\frac{\phi}{2}]^2\ . \tag{4.11}$$

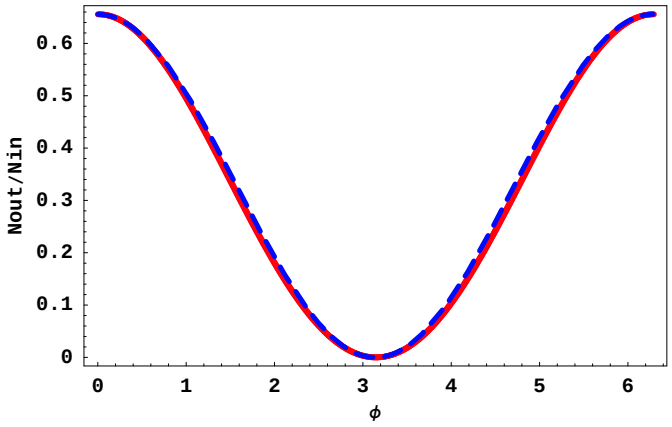

FIG. 43: Interferometer total transmission for $t = 0.01$. The blue dashed line is a fit to the function $\frac{2}{3}\cos[\frac{\phi}{2}]^2$

A correspondence between the numerical integration and the analytical approximation is shown in Fig.(43). Substituting the parameters given in the introduction to this chapter and Eq.(4.11) into Eq.(3.30), yields the sensitivity of the interferometer in this regime, as seen in Fig.(44). A maximal sensitivity of 1.1 10^{-10} $rad/sec/\sqrt{Hz}$ is achieved at $\phi = \pi$, which is equivalent to rotation rate of $\pi\frac{\hbar}{2ms} = 3.53\ 10^{-5}\ rad/sec$.

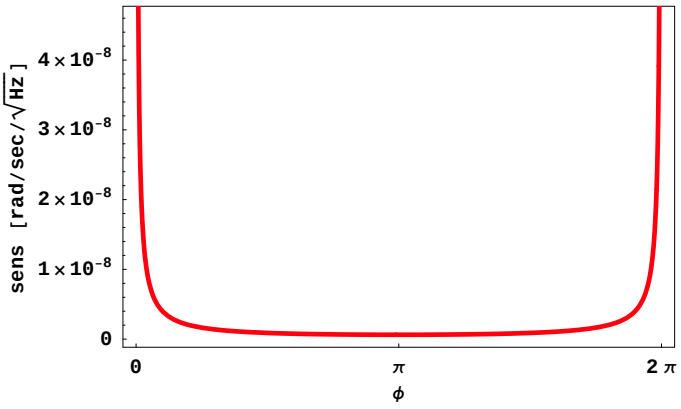

FIG. 44: Interferometer sensitivity for $t = 0.01$, $L = 2\pi 2.6\,mm$, $m = 2.2\ 10^{-25}\ Kg$ and $N_{in} = 1.6\ 10^{1}0\ \frac{atom}{sec}$ at the narrow band regime. A maximal sensitivity of 1.1 10^{-10} $rad/sec/\sqrt{Hz}$ is achieved at $\phi = \pi$, which is equivalent to rotation of $\pi\frac{\hbar}{2ms} = 3.53\ 10^{-5}\ rad/sec$.

Like in the monochromatic case, the atoms should be cooled to a temperature which is lower than a feasible temperature (See App.C).

3. Wide Band

The third regime is the wide band regime where $\Delta_k \gg \frac{2\pi}{L} > \Delta_T$. Similarly to the narrow band regime the number of atoms that exit the interferometer is given by an integration over the product $I(k)T(k,\phi)$, but unlike the narrow-band regime the limits are all over the spectrum

$$N_{out} \;=\; N_{in}\int_{-\infty}^{\infty} dk\; I_{in}(k)\; T(k,\phi)\;. \tag{4.12}$$

In appendix D we show in details that this integral can be approximated by

$$N_{out} \approx N_{in} a_1(\Delta_1 - \Delta_2)\frac{L}{2}\;, \tag{4.13}$$

where

$$\begin{aligned}
\Delta_1 \;&=\; \sqrt{\frac{1-\frac{1-2t+2t^2}{2(1-t)^2}\sin^2[\frac{\phi}{2}]}{L^2\left(\left(\frac{1-2t+2t^2}{4t(1-t)}\right)^2-\frac{1}{2}\right)}} \quad;\quad \Delta_2 = \sqrt{\frac{t^2\left(1-\frac{1-2t+2t^2}{2(1-t)^2}\sin^2[\frac{\phi}{2}]\right)}{L^2(1-t)^2\left(\frac{1}{\sin^4[\frac{\phi}{2}]}-\frac{t^2}{4(1-t)^2}\right)}}\;; \\
a_1 \;&=\; \frac{\cos^2[\frac{\phi}{2}]}{1-\frac{1-2t+2t^2}{2(1-t)^2}\sin^2[\frac{\phi}{2}]}\;.
\end{aligned} \tag{4.14}$$

We note that the dependence on r vanishes due to the $\frac{1}{L}$ factor in the terms Δ_1 and Δ_2. In Fig.(45) we see the changing of N_{out} due to varying in ϕ for matrix parameter $t = 0.01$ and an approximate analytical fit given by

$$N_{out}/N_{in} \approx \frac{2t}{1-t}\cos[\frac{\phi}{2}]^2\;. \tag{4.15}$$

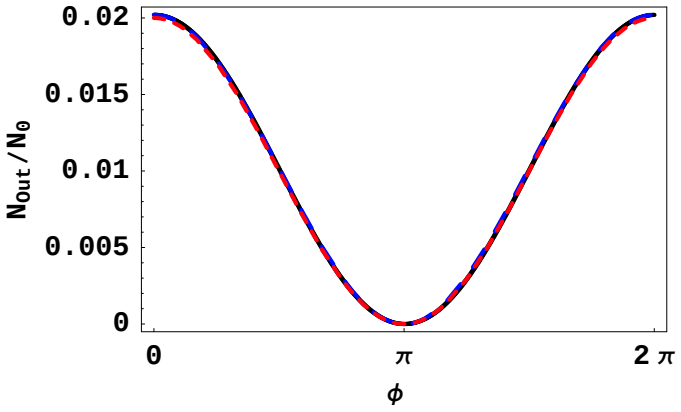

FIG. 45: Interferometer total transmission *vs* ϕ for $t = 0.01$. The black curve is the numeric integration of $\sum_{n=-\infty}^{\infty} I_{in}(\frac{2n\pi}{L}) \int_{-\pi}^{\pi} dk\ T(k,\phi)$. The blue dashed line is the Lorentzians subtraction approximation (Eq.(4.13)). The dashed red line is the a fit to $\frac{2t}{1-t}\cos[\frac{\phi}{2}]^2$.

In this regime, where $\Delta_k \gg \frac{2\pi}{L}$, the coherence length is much smaller than L, $\Delta_x \ll L$ (see section 3.7). From this, it follows that only equal order trajectories can interfere. Under this assumption we can rewrite Eq.(4.5)

$$t_a \approx \sum_{n=0}^{\infty} 4(t-t^2)\cos\frac{\phi}{2} e^{ik\frac{L}{2}}(1-t)^{2n}\, e^{nikL} = \sum_{n=0}^{\infty} a_n\, e^{nikL} \ \rightarrow\ \sum_{n=0}^{\infty} a_n\ , \tag{4.16}$$

where the dependence on k vanishes. It is interesting to note that the resulting transmission $T = |\sum_{n=0}^{\infty} a_n|^2$ can be approximated, up to a $\frac{t}{2}$ factor, to the result given in Eq.(4.15)
Substituting the parameters given in the introduction to this chapter and Eq.(4.15) into Eq.(3.30), yields the sensitivity of the interferometer in this regime, as seen in Fig.(46). A maximal sensitivity of $6.28\ 10^{-10}\ rad/sec/\sqrt{Hz}$ is achieved at $\phi = \pi$, which is equivalent to rotation rate of $\pi\frac{\hbar}{2ms} = 3.53\ 10^{-5}\ rad/sec$.
In summary, we find that a better sensitivity is achieved as the bandwidth becomes narrower (see Table.(I)), i.e. the temperature is lower. As the required temperature for the monochromatic regime i.e. the narrow band regime is lower than an experimentally feasible temperature, in the following sections we focus on the wide band regime. Furthermore, by examining the scattering matrix (Eq.3.19), we notice that at the regime $t \ll 1$ the probability amplitude of internal reflection is ≈ -1 and the probability of an atom to be reflected forward and backwards is ≈ 1. Every time an atom moves forward and backward

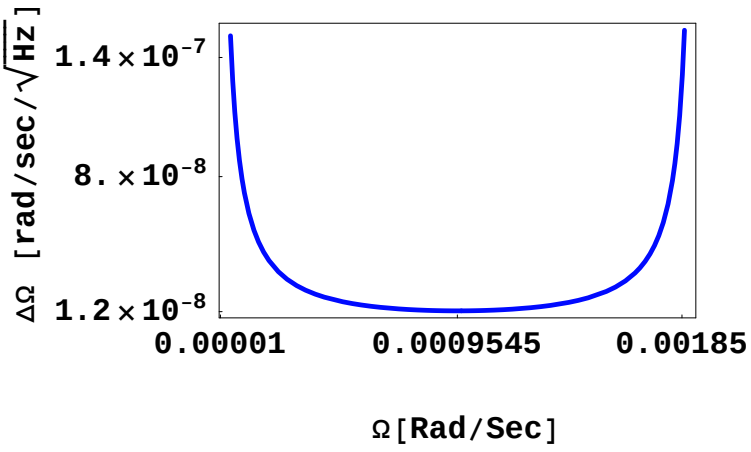

FIG. 46: Interferometer sensitivity for $t = 0.01$, $L = 2\pi 2.6\, mm$, $m = 2.2\, 10^{-25}\, Kg$ and $N_{in} = 1.6\, 10^{1}0\, \frac{atom}{sec}$ at the wide band regime. A maximal sensitivity of $6.28\ 10^{-10}\ rad/sec/\sqrt{Hz}$ is achieved at $\phi = \pi$, which is equivalent to rotation of $\pi\frac{\hbar}{2ms} = 3.53\ 10^{-5}\ rad/sec$.

Type	**Max. Sensitivity** $(\frac{rad}{sec}/\sqrt{Hz})$
Monochromatic	$\rightarrow\ 0$ as $kL(mod\, 2\pi)\ \rightarrow\ 0$
Narrow Band	$1.1\, 10^{-10}$
Wide Band	$6.28\, 10^{-10}$

TABLE I: Interferometer sensitivity for different bandwidths

a cancelation of the phase shift occurs, hence the sensitivity at this regime expected to be lower than regimes of higher t.

4.3. Interferometer Transmission and Sensitivity Calculation for $t = \frac{1}{2}$

By substitution of $t = \frac{1}{2}$ into Eq.(4.1) we obtain the transmission

$$T(k,t=\frac{1}{2})=\frac{4\cos^2\frac{\phi}{2}\sin^2\frac{kL}{2}}{\left(0.5-\cos kL+0.5\cos\phi\right)^2+\sin^2 kL}\ . \tag{4.17}$$

For $\phi=0$ the transmission is unity for every k and as ϕ becomes different than zero occur dips around $k\,L=2\,n\,\pi$, as seen in Fig.(47).

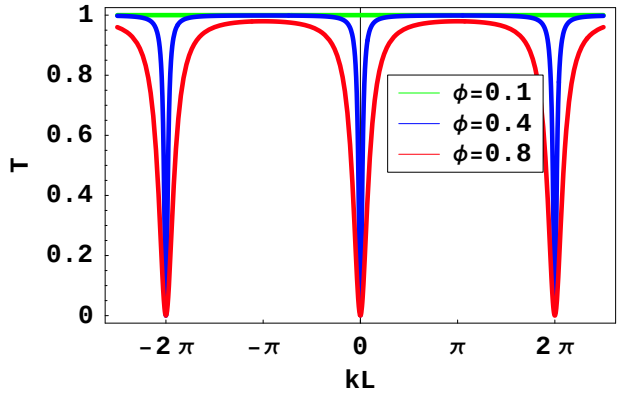

FIG. 47: Interferometer Transmission for $t=\frac{1}{2}$. The location of the dips is constant for different rotation rates, but the width of dips is getting larger with ϕ, between $0\div\pi$ and vice versa between $\pi\div 2\pi$

Similarly to the $t\ll 1$ regime we would like to simplify the expression for the transmission in a way that will simply demonstrate, in mathematical terms, the behavior of the function and will permit to calculate the integral $\int_{-\infty}^{\infty}dkI(k)T(k,\phi)$. From Eq.(4.17) we obtain

$$T(k_0+\Delta k,t=\frac{1}{2})=\frac{4\cos^2\frac{\phi}{2}\sin^2\frac{k_0L+\Delta kL}{2}}{\left(0.5-\cos\left(k_0L+\Delta kL\right)+0.5\cos\phi\right)^2+\sin^2\left(k_0L+\Delta kL\right)} \tag{4.18}$$

Algebraic manipulation and Taylor expansion around $k_0=\frac{2n\pi}{L}$ will give ,

$$
\begin{aligned}
T(k_0+\Delta k, t=\frac{1}{2}) &= \frac{4\cos^2\frac{\phi}{2}\sin^2\frac{\Delta kL}{2}}{\left(0.5-\cos\left(\Delta kL\right)+0.5\cos\phi\right)^2+\sin^2\left(\Delta kL\right)} \\
&= \frac{4\cos^2\frac{\phi}{2}\sin^2\frac{\Delta kL}{2}}{\left(\sin^2\left(\frac{\phi}{2}\right)-2\sin^2\frac{\Delta kL}{2}\right)\right)^2+\sin^2\left(\Delta kL\right)} \\
&\approx \frac{\cos^2\frac{\phi}{2}(\Delta kL)^2}{\sin^4\left(\frac{\phi}{2}\right)-\sin^2\left(\frac{\phi}{2}\right)(\Delta kL)^2+(\Delta kL)^2} \\
&= \frac{(\Delta k)^2}{\frac{\sin^2\left(\frac{\phi}{2}\right)\tan^2\left(\frac{\phi}{2}\right)}{L^2}+(\Delta k)^2} \approx \frac{(\Delta k)^2}{(\frac{\phi^2}{4L})^2+(\Delta k)^2} \ ,
\end{aligned}
\tag{4.19}
$$

For $\phi \lesssim \frac{\pi}{2}$, a good periodic approximation for Eq.(4.18) is given by

$$
T(k, t=\frac{1}{2}) = 1-\sum_{n=-\infty}^{\infty}\frac{\Delta(\phi)^2}{\left(k-\frac{2n\pi}{L}\right)^2+\Delta(\phi)^2} = 1-\sum_{n=-\infty}^{\infty}\tilde{T}_n(k,\phi) \ . \tag{4.20}
$$

where $\Delta(\phi)=\frac{\phi^2}{4L}$. The sum in Eq.(4.20) converges into

$$
T(k, t=\frac{1}{2}) = 1-\frac{\phi^2\sinh(\frac{\phi^2}{4})}{8\cosh(\frac{\phi^2}{4})-8\cos(kL)} \ . \tag{4.21}
$$

The transmission vs the momentum and the approximated transmission shown in Fig.(48)

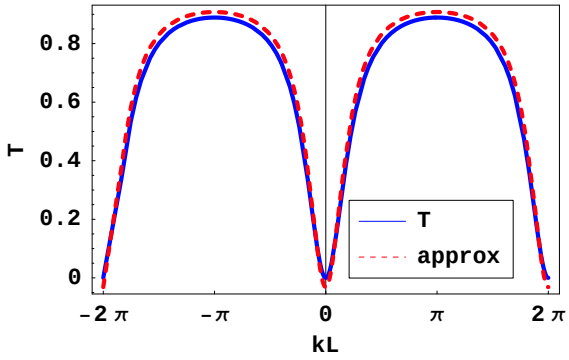

FIG. 48: Interferometer transmission vs the momentum, for $\phi=\frac{\pi}{2}$. The dashed red line is the approximated transmission as given in Eq.4.21.

As mentioned above, similarly to the $t \ll 1$ regime, the number of atoms that exit the

interferometer is given by

$$N_{out} \approx N_{in} \sum_{n=-\infty}^{\infty} I_{in}(\frac{2n\pi}{L}) \int_{\frac{(2n-1)\pi}{L}}^{\frac{(2n+1)\pi}{L}} dk\ T(k,\phi) = N_{in} \frac{L}{2\,\pi} \int_{-\frac{\pi}{L}}^{\frac{\pi}{L}} dk\ T(k,\phi)\ , \quad (4.22)$$

where the dependence on L vanishes (see Eq.(4.10)). A numerical solution to Eq.(4.22) and an analytical fit to

$$\frac{N_{out}}{N_{in}} \approx a_1 \left(1 - \exp\left[-\frac{1}{2}\left(\frac{\phi-\pi}{a_2}\right)^2\right]\right)\ , \quad (4.23)$$

are shown in Fig.(49) where $a_1 \approx 1.01$ and $a_2 \approx 1.06$.

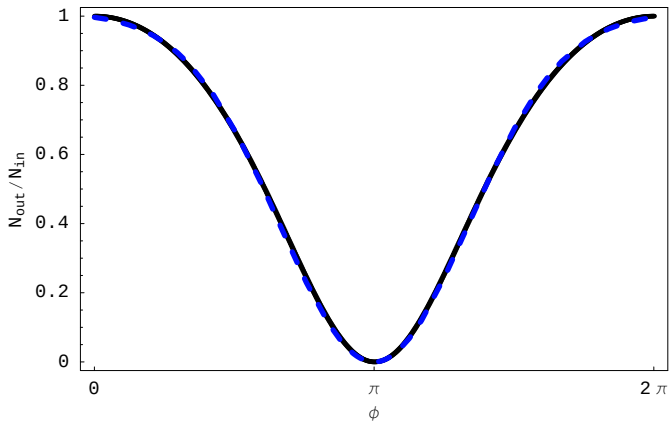

FIG. 49: The black curve is the numeric integration of $\frac{N_{out}(\phi)}{N_{in}}$. The dashed blue line is a fit to this result

Substituting the parameters given in the introduction to this chapter and Eq.(4.23) into Eq.(3.30), yields the sensitivity of the interferometer in this regime, as seen in Fig.(50). A maximal sensitivity of 6.6 10^{-11} $rad/sec/\sqrt{Hz}$ is achieved at $\phi = \pi$, which is equivalent to rotation rate of $\pi\frac{\hbar}{2ms} = 3.53\ 10^{-5}\ rad/sec$. This result is one order of magnitude better than the result calculated for the $t \ll 1$ regime.

In this regime the particle has a higher probability to complete a full cycle than at the regime $t \ll 1$, thus the sensitivity in this regime is higher.

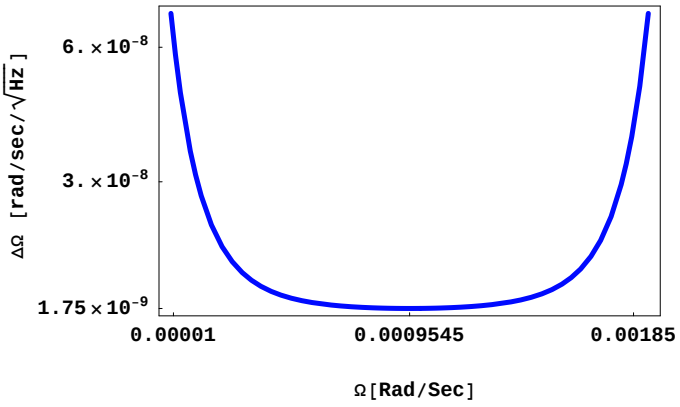

FIG. 50: Interferometer sensitivity for $t = \frac{1}{2}$, $L = 2\pi 2.6\ mm$, $m = 2.2\ 10^{-25}\ Kg$ and $N_{in} = 1.6\ 10^{1}0\ \frac{atom}{sec}$. A maximal sensitivity of $6.6\ 10^{-11}\ rad/sec/\sqrt{Hz}$ is achieved at $\phi = \pi$, which is equivalent to rotation of $\pi\frac{\hbar}{2ms} = 3.53\ 10^{-5}\ rad/sec$.

4.4. Interferometer Transmission and Sensitivity Calculation for $t \approx 1$

From Eq.(3.19) we obtain that for $t \to 1$ the probability of the reflection within the channels is much smaller compared to the probability of a particle to pass from channel to channel inside the interferometer. In other words the particle completes many full cycles before crossing the junction out of the interferometer and the the transmission amplitude (TA) could be approximated by two independent sums over trajectories of each arm of the interferometer. The approximated TA of the clockwise trajectory is given by

$$\begin{aligned} t_{a,c.w.} &\approx \sum_{n=0}^{\infty} \sqrt{2(t-t^2)}\exp\left[i(k-\frac{\phi}{L})\frac{L}{2}\right]\left(t^2\exp\left[i(k-\frac{\phi}{L})L\right]\right)^n\sqrt{2(t-t^2)} \\ &= \frac{2(t-t^2)\exp\left[i(k-\frac{\phi}{L})\frac{L}{2}\right]}{1-t^2\exp\left[i(kL-\phi)\right]}, \end{aligned} \tag{4.24}$$

and

$$\begin{aligned} T_{c.w.} &= |t_{a,c.w}|^2 \approx \frac{4(t-t^2)^2}{1+t^4-2t^2\cos(kL-\phi)} \approx \frac{4(t-t^2)^2}{1+t^4-2t^2\left(1-\frac{(kL-\phi)^2}{2!}\right)} \\ &= \frac{4(t-t^2)^2}{(1-t^2)^2+t^2(kL-\phi)^2}. \end{aligned} \tag{4.25}$$

Taylor expansion for $t \approx 1$ will give

$$T_{c.w.} \approx \frac{[2(1-t)/t]^2}{[2(t-1)/t]^2 + (kL-\phi)^2}. \tag{4.26}$$

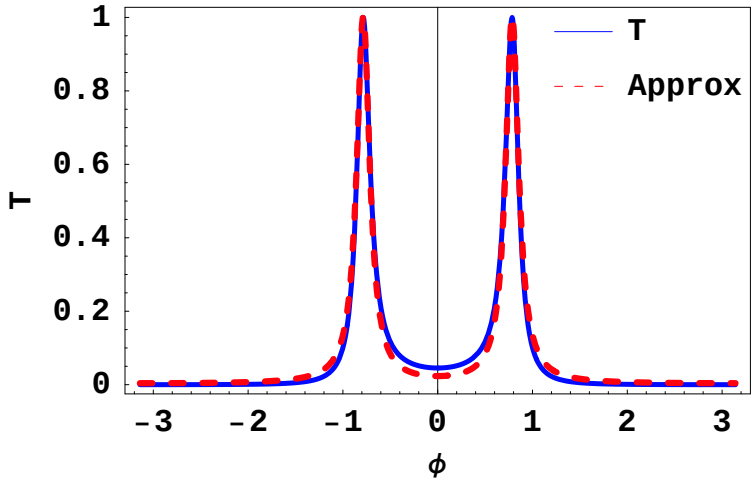

FIG. 51: Transmission of interferometer with matrix parameter $t = 0.96$ and $\phi = \frac{\pi}{3}$ (blue line). The red dashed line is the approximated transmission as given in Eq.(4.29).

From the same consideration the counter-clockwise transmission may be approximated by

$$T_{cc.w.} = \frac{4(t-t^2)^2}{1+t^4+2t^2\cos(kL+\phi)} \approx \frac{[2(1-t)/t]^2}{[2(t-1)/t]^2 + (kL+\phi)^2}. \tag{4.27}$$

The total transmission , as shown in Fig(51), is the sum of the transmission in both directions

$$T = T_{c.w.} + T_{cc.w.}\ , \tag{4.28}$$

The periodic form of Eq.(4.28) is given by an infinite sum of Lorentzians, as shown in Fig.(51)

$$T(k,\phi) \approx \sum_{n=-\infty}^{\infty} \Delta \left(\frac{\Delta}{(k\,L-(2n\pi+\phi))^2+\Delta^2} + \frac{\Delta}{(k\,L+(2n\pi-\phi))^2+\Delta^2} \right)$$
$$= \sum_{n=-\infty}^{\infty} T_n(k,\phi)\ , \tag{4.29}$$

where $\phi = \frac{2mS}{\hbar}\Omega$ and $\Delta = \frac{2(1-t)}{t}$ is the Lorentzian width. All the Lorentzians are equal and the area under each Lorentzian is given by

$$\int_{-\infty}^{\infty} T_n dk = \pi\Delta\ . \tag{4.30}$$

Let us inspect the behavior of the transmission as a function of the momentum k, as shown in Fig.(52). At this regime ($t \to 1$) and for $\phi = 0$ the transmission is characterized by a single Lorentzian curve which evolve smoothly into two Lorentzian curves, each Lorentzian centered around $k\,L = 2n\pi \pm \phi$, as ϕ becomes different than zero. The right Lorentzian is shifted to the right, and the left one is shifted to the left, as ϕ increases, and viseversa as ϕ decreases.

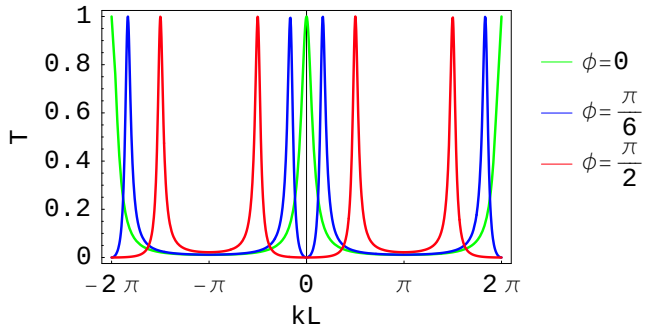

FIG. 52: Interferometer transmission matrix parameter $t = 0.95$. As ϕ increases, the peaks are shifted from the center of the double peak structure, located at $k = \frac{2n\pi}{L}$. Once the curve structure evolves into full separated peaks their width is constant with ϕ.

Similar to the $t \ll 1$ and the $t = \frac{1}{2}$ cases, the number of atoms that exit the interferometer could be given by

$$
\begin{aligned}
N_{out} &= N_{in}\int_{-\infty}^{\infty} dk\ I_{in}(k)\ T(k,\phi) \approx N_{in}\sum_{n=-\infty}^{\infty}\int_{-\infty}^{\infty} dk\ I_{in}(k)\ T_n(k,\phi) \\
&= N_{in}\sum_{n=-\infty}^{\infty}(I_{in}(\frac{2n\pi+\phi}{L})+I_{in}(\frac{2n\pi-\phi}{L}))\int_{\frac{2n\pi}{L}}^{\frac{2(n+1)\pi}{L}} dk\ T_n(k,\phi) \\
&\approx N_{in}\pi\Delta\sum_{-\infty}^{\infty}(I_{in}(\frac{2n\pi+\phi}{L})+I_{in}(\frac{2n\pi-\phi}{L})) \\
&\approx N_{in}\pi\frac{2(1-t)}{tL}2r = N_{in}\frac{2(1-t)}{t}\ . \qquad (4.31)
\end{aligned}
$$

This approximation is not valid around $\phi=\pi$ but we will use its final results to characterize more correct approximation. In order to find N_{out} let us recall Eq.(4.22) and integrate numerically (for $t=0.99$) as plotted in Fig.(53).

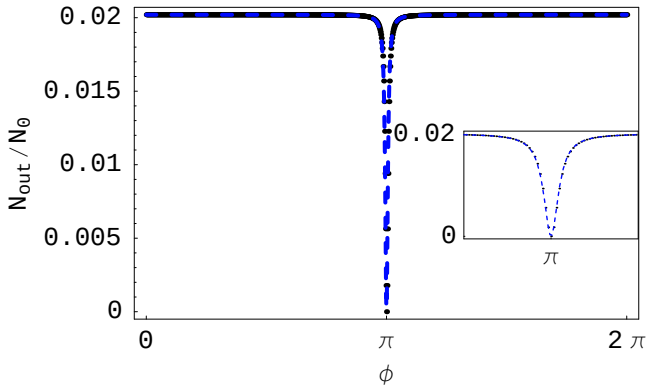

FIG. 53: The black curve is the numeric solution of N_{out} (in units of N_0) *vs* ϕ, for $t=0.99$ and $r=500\mu m$. The dashed blue line is a fit to this result and a zoom in on the Lorentzian shape is plotted in the inset

An analytical fit to this curve is given by

$$
\frac{N_{out}}{N_{in}} \approx \left(a-\frac{a^3}{a^2+(\phi-\pi)^2}\right)\ , \qquad (4.32)
$$

where $a=\Delta$ could be also derived from the final result of Eq.(4.31). Substituting the parameters given in the introduction to this chapter and Eq.(4.23) into Eq.(3.30), yields the sensitivity of the interferometer in this regime, as seen in Fig.(54). A maximal sensitivity

of 6.3 10^{-12} $rad/sec/\sqrt{Hz}$ is achieved at $\phi = \pi$, which is equivalent to rotation rate of $\pi\frac{\hbar}{2ms} = 3.53\ 10^{-5}\ rad/sec$. This result is one order of magnitude better than the result calculated for the $t = \frac{1}{2}$ regime.

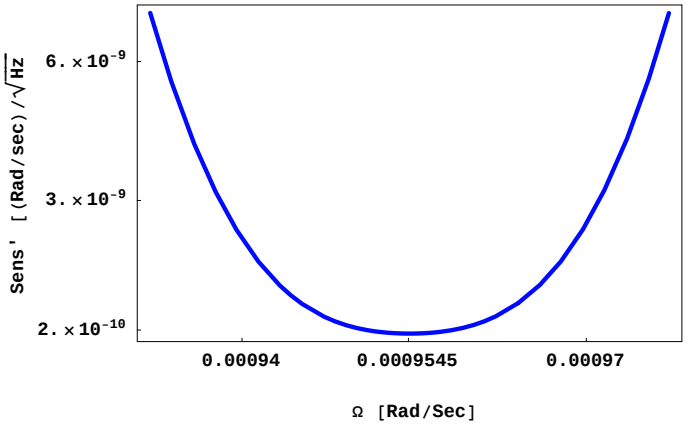

FIG. 54: Interferometer sensitivity for $t = 0.99$, $L = 2\pi 2.6\ mm$, $m = 2.2\ 10^{-25}\ Kg$ and $N_{in} = 1.6\ 10^{1}0\ \frac{atom}{sec}$. A maximal sensitivity of 6.3 10^{-12} $rad/sec/\sqrt{Hz}$ is achieved at $\phi = \pi$, which is equivalent to rotation of $\pi\frac{\hbar}{2ms} = 3.53\ 10^{-5}\ rad/sec$.

In this regime the particle has the highest probability to complete many full cycles and to accumulate Sagnac phase shift. Thus the sensitivity in this regime is the highest.

4.5. General Expression for Sensitivity

Recall Eq.(3.30), we notice that only the term $\Delta\phi \equiv \sqrt{T}/\frac{dT}{d\phi}$ depends on the matrix parameter t. It turns out that in both regimes $t \ll 1$ and $t \to 1$ the intrinsic sensitivity converges to

$$\lim_{\phi\to\pi} \Delta\phi = \sqrt{\frac{1-t}{2\,t}}\ . \tag{4.33}$$

Substituting this result into Eq.(3.30) yields a general expression for the maximal sensitivity

$$\Delta\Omega_{max} = \frac{\hbar}{2\,m\,s\,\sqrt{N_{in}}}\sqrt{\frac{1-t}{2\,t}} = \frac{\hbar}{2\,m\,s\,\sqrt{N_{in}}}\sqrt{\frac{\pi}{4\,\mathcal{F}}}\ . \tag{4.34}$$

The maximal sensitivity goes to zero as $t \to 1$, i.e. the sensitivity is getting better as the finesse (see section 3.8) of the interferometer is getting higher.

In Table.(II) we compare between the final results of sections 4.2−4.5. Although these values are given for an interferometer with specific parameters ($r = 2.6\,10^{-3}\,m$, $m = 2.2\,10^{-25}\,Kg$ and $N_{in} = 1.6\,10^{10}\,\frac{atom}{sec}$), we can see that the high finesse interferometer is more sensitive by two orders of magnitude than the low finesse interferometer. This result is the main result of this chapter.

Matrix Parameter (t)	**Max. Sensitivity** $(\frac{rad}{sec}/\sqrt{Hz})$
0.01	$6.28\,10^{-10}$
$\frac{1}{2}$	$6.6\,10^{-11}$
0.99	$6.3\,10^{-12}$

TABLE II: A summary of the final results for the real amplitudes interferometer sensitivity

4.6. Transmission and Sensitivity Calculation for Interferometer based on Horizontal Complex Amplitudes Beam-Splitter

In order to calculate the total transmission amplitude of an anti-symmetrically configured interferometer with a beam splitter described in section (3.3), we substitute the scattering matrix given by Eq.(3.24) into Eq.(3.22) and permute B_{up} with B_{do}. Like in the real amplitudes case a solution of the six equations set, yields an expression for the total transmission amplitude. A general expression for the interferometer transmission is given by

$$T = \frac{32\cos(\frac{k\,L}{2} + \delta)^2\cos(\frac{\phi}{2})^2}{11 + 4\,\cos(\phi) + 8\,\cos(k\,L + 2\,\delta)\,(1 + \cos(\phi)) + \cos(2\,\phi)}\ , \tag{4.35}$$

where δ defined by the distance between the potential barrier and the "mirror" in port 4

and by the imaginary part of the reflection coefficient of the "mirror". In the anti-symmetric configuration , both channels accumulate a phase of $e^{i\frac{\pi}{2}}$ due to the crossing of two beam-splitters and similar to the real amplitude case the total transmission will be unity for $\phi = 0$ and zero for $\phi = \pi$. In particular, the transmission is similar to the real amplitudes, $t = \frac{1}{2}$ case, up to a shift of $\pi - 2\delta$, i.e. the center of the dip located at $kL = (2n+1)\pi - 2\delta$, as seen in Fig.(55). In order to calculate the number of atoms that exit the interferometer in the feasible wide band case, we integrate over a full period of 2π, therefore the ratio $\frac{N_{out}(\phi)}{N_{in}}$ (see Eq.(4.23) and Fig.49) and the sensitivity (see Fig.(50) and Tab.II) are equal to the real amplitudes, $t = \frac{1}{2}$ case for every δ.

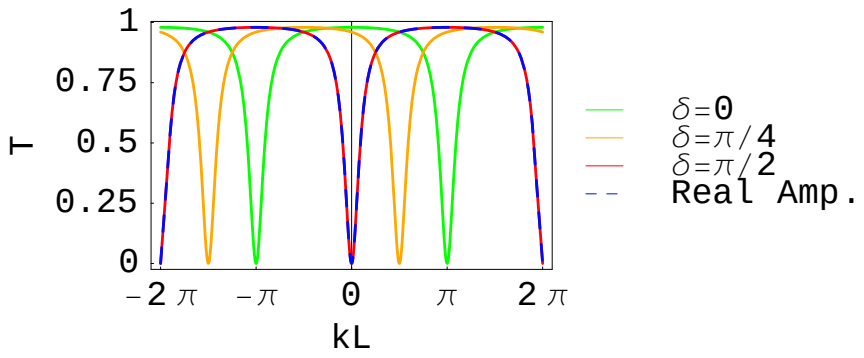

FIG. 55: Horizontal anti-symmetrically configured interferometer transmission vs kL for different δ where $\phi = \frac{\pi}{3}$. The dashed blue line is the transmission of a real amplitude interferometer with matrix parameter $t = \frac{1}{2}$.

Similarly by substituting the scattering matrix given by 3.24 into Eq.(3.22), without permuting B_{up} with B_{do}, we obtain a different set of six equations. A solution of this set, yields an expression for the total transmission amplitude of a symmetrically configured interferometer with a beam splitter described in section (3.3). A general expression for the interferometer transmission is given by,

$$T = \frac{32\sin(\frac{kL}{2}+\delta)^2\sin(\frac{\phi}{2})^2}{11+8\cos(kL+2\delta)\,(-1+\cos(\phi))-4\cos(\phi)+\cos(2\phi)}\,. \tag{4.36}$$

In the symmetric configuration , a particle that travels in the port opposite to the mirrors port accumulates a phase of $e^{i\pi}$ due to reflections and the total transmission will be zero

for $\phi = 0$ and 1 for $\phi = \pi$. The center of the dip located at $kL = 2n\pi - 2\delta$, as seen in Fig.(56). Like in the anti-symmetric configuration, and from the same reasons, the sensitivity magnitude is equal to the Real amplitudes, $t = \frac{1}{2}$ for every δ, but in contrast, the maximal sensitivity achieved around *zero*.

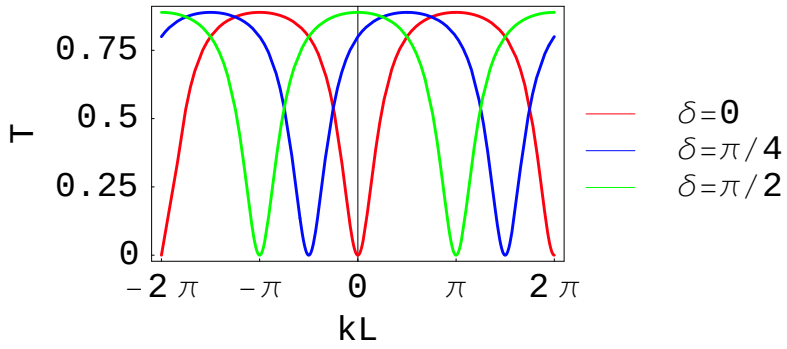

FIG. 56: Horizontal symmetrically configured interferometer transmission vs kL for different δ where $\phi_{eff} = \frac{\pi}{2}$.

4.7. Transmission and Sensitivity Calculation for Interferometer based on Vertical Complex Amplitudes Beam-Splitter

In the vertical configuration of two complex amplitude beam-splitters and for $r \to 1$ the atom has a high probability to complete many cycles in the interferometer and to accumulate a large Sagnac phase-shift between the "left" and "right" contributions. Similarly to the horizontal configuration there are two optional configurations. In the horizontal case we noticed that in the anti-symmetric configuration the transmission is unity for $\phi = 0$ and zero for $\phi = \pi$ and vice versa in the symmetric configuration. The zeroing of the transmission at $\phi = 0$ ensure an optimal working point of the interferometer at $\Omega \to 0$. From this reason, the symmetric configuration is of a main interest in this section.

By Substituting Eq.(3.26) into Eq.(3.22) we obtain a set of six equation. A solution for this set yields the total transmission amplitude t_a and the interferometer transmission $T = |t_a|^2$, is given by

$$T = \left(2\left(-1+r^2\right)^2\cos(\frac{k\,L}{2})^2\left(1+r^4-2\,r^2\,\cos(\phi)\right)\right)\Big[P(r)+r^4\,\cos(2\,k\,L)-2\left(r-r^3\right)^2\cos(\phi) + \left(1+r^4\right)\cos(k\,L)\left(\left(-1+r^2\right)^2-2\,r^2\,\cos(\phi)\right)+r^4\,\cos(2\,\phi)\Big]^{-1}\,, \tag{4.37}$$

where $P(r) = 1-2\,r^2+4\,r^4-2\,r^6+r^8$. Similarly to the real amplitudes $t \to 1$ case, we obtain a 2π period single peaked structure at $\phi = 0$, each peak evolves into a double peak structure as ϕ becomes different from zero. Unlike the previous configurations the transmission does not vanish for $\phi = 0$ nor for $\phi = \pi$, as seen in Fig.(57).

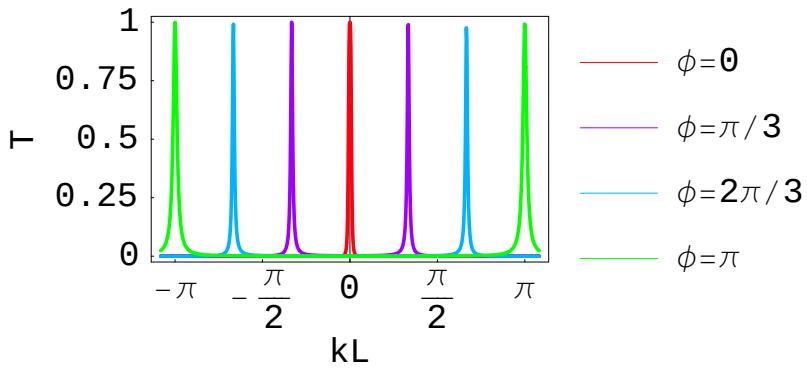

FIG. 57: Vertical symmetrically configured interferometer transmission vs kL for different δ where $\phi_{eff} = \frac{\pi}{2}$.

As seen in Fig.(58), the rate of atoms that exit the interferometer is given by

$$N_{out} = N_{in}\int_{-\infty}^{\infty} dk T(k,\phi)I(k) \approx N_{in}\left(a - \frac{a^3}{2a^2+\phi^2}\right) = N_{in}\left(a - \frac{a^3}{2a^2+(\alpha\Omega)^2}\right), \tag{4.38}$$

where $I(k)$ is the momentum distribution and $a \approx \frac{2(1-r)}{r}$. Unlike other configurations treated in previous sections, the minimal value of N_{out}/N_{in} is not zero, but it is equal to $a/2$, i.e half of the maximal value. Recall Eq.(3.29) we obtain the interferometer sensitivity

$$\Delta\Omega = \frac{\left(2\,a^2+\alpha^2\,\Omega^2\right)^2\sqrt{a-\frac{a^3}{2\,a^2+\alpha^2\,\Omega^2}}}{2\,a^3\,\alpha^2\,\Omega\,\sqrt{N_{in}}}\,. \tag{4.39}$$

By comparing $\frac{d}{d\Omega}(\Delta\Omega)$ to zero we obtain Ω_0, the rotation rate where the sensitivity is

maximal

$$\Omega_0 \approx \frac{\pi a}{3\sqrt{2}\alpha} \ . \tag{4.40}$$

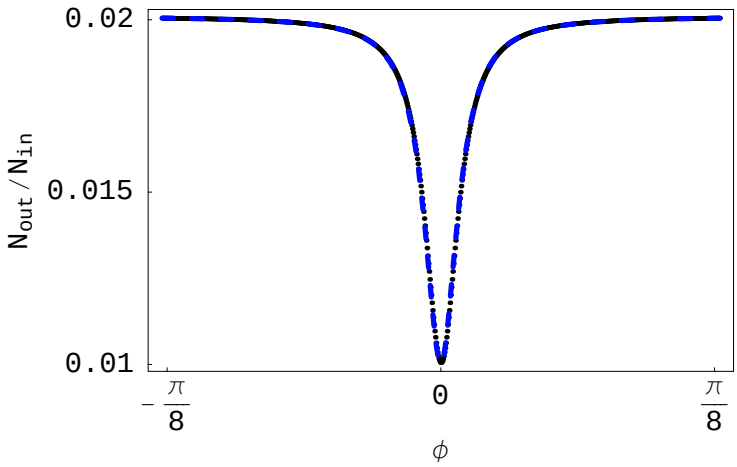

FIG. 58: N_{out} vs *phi* for $r = 0.99$. The rate of atoms exit the interferometer does not go to zero at $\phi = 0$ nor at $\phi = \pi$ but it goes to the half of the maximal value at $\phi = 0$

Substituting Eq.(4.40) into Eq.(4.39) yields the maximal sensitivity in terms of the fundamental interferometer parameters

$$\Delta\Omega_{max} = \frac{\left(2a^2 + \alpha^2\Omega^2\right)^2 \sqrt{a - \frac{a^3}{2a^2+\alpha^2\Omega^2}}}{2a^3\alpha^2\Omega\sqrt{N_{\rm in}}} \approx \frac{3\pi^3}{20\sqrt{a\,N_{\rm in}}}\,\Omega_0 \ . \tag{4.41}$$

For $r = 0.99$ (equivalent to $t = 0.99$ in the real amplitudes case) and for the standard parameters in this work $m = 2.2\ 10^{-25} Kg$, $r = 2.6\,10^{-3}\,m$ and $N_{in} = 1.6\ 10^{10}\frac{atoms}{sec}$ we obtain at $\phi_0 = \frac{\pi}{210}$, which is equivalent to rotation rate of $1.68\,10^{-7}\,\frac{rad}{sec}$, a maximal sensitivity of $4.3\ 10^{-11}\ \frac{rad}{sec}/\sqrt{Hz}$. This result is one order of magnitude worse the result obtained in the real amplitude $t \to 1$ case. The difference between the two high finesse configurations could be explained by a crucial difference in the symmetry of each beamsplitter. In the real amplitude case, once the particle enters the interferometer there is a symmetry between the transmission and reflection amplitudes of the internal channels which accumulate the Sagnac phase shift (see Eq.(3.19)). Namely, when $\phi = \pi$, for each copropagating contribution of the wave function there is a counterpropagating contribution with a π phase difference. Therefore, the total transmission is identical to zero for $\phi = \pi$. On the other hand, in the

vertical complex case, the reflection amplitudes of the internal channels are not symmetrical (see Eq.(3.26)), moreover one of the reflection amplitude is identical to zero. That means that the reflected contributions from the internal channel with non-zero reflection amplitude do not have counterpropagating contributions with a π phase difference to destructively interfere with. Therefore, the total transmission does not go down to zero for any ϕ, but goes down to half of the maximal value. Furthermore, this asymmetry increases the complexity of the interfering trajectories and the width of the Lorentzian curve becomes wider (see Eq.(4.32) and Eq.(4.38)). These differences imply also a difference in the sensitivity due to the term $dN_{out}/d\phi$.

5. SUMMARY, CONCLUSIONS AND FUTURE WORK

5.1. Summary and Conclusions

In this thesis we presented a theoretical model for a Sagnac atom interferometer. The model relies on the analogy between a massive particle travelling in a rotating frame and a charged particle travelling in a ring with a magnetic flux. Within the model, we neglected atom-atom interactions and impurities in the system. The scattering matrix formalism was used to calculate the transmission and the sensitivity of a revolving atom interferometer. First, the general transmission of an interferometer based on a double Y beamsplitter was calculated. Due to the complexity of the expression for the transmission we distinguished between three regimes of the matrix parameter t, which corresponds physically to the ability of a particle to cross from one arm of the interferometer to another: $t \ll 1$, $t = \frac{1}{2}$ and $t \to 1$. We inspected the regime $t \ll 1$ as a test case, and within this regime we distinguished between three regimes of the momentum bandwidth. We demonstrated that the sensitivity is improved with the decreasing of the momentum bandwidth (see Table.(I)), i.e. with the decreasing of the temperature.

However, the required temperature for a narrow momentum bandwidth is much lower than experimentally feasible temperatures. Therefore, this work focuses on the wide band regime, which is experimentally feasible, and analyzes the sensitivity in the $t = \frac{1}{2}$ and $t \to 1$ regimes. The main result of the thesis is an expression for the maximal sensitivity as a function of the finesse

$$\Delta\Omega_{max} = \frac{\hbar}{2\,m\,s\,\sqrt{N_{in}}}\sqrt{\frac{\pi}{4\,\mathcal{F}}}\ ,$$

where $\hbar$ is the Planck constant, m is the atomic mass, s is the interferometer area, N_{in} is the incoming particles flux and $\mathcal{F}$ is the finesse. Our model confirms the assumption that the sensitivity is improved with the increasing of the interferometer finesse. We have confirmed that the sensitivity found in the real amplitude case, in the situation where $t \ll 1$, i.e. describing a low finesse interferometer, is of the same order of magnitude as the sensitivity of the experimentally realized 'one-pass' freely propagating atom interferometers. This result

is significant not only because it verifies our model, but also as it confirms the assumption that in this regime of low finesse, the total effect on the sensitivity to rotations, of a particle in a freely propagating atom interferometer, is similar to the total effect of a particle in a smoothly guided atom interferometer. Up to date, there is no realized high finesse atom interferometer to compare our model with, and the obtained results will hopefully motivate such a realization.

Type	**Section**	**Matrix Parameter**	**Max. Sensitivity** $(\frac{rad}{sec}/\sqrt{Hz})$	**Comparison**
Single Mode	4.2	$t = 0.01$	$6.3\,10^{-10}$	2.86
Real Amplitudes	4.3	$t = \frac{1}{2}$	$6.6\,10^{-11}$	0.3
Scattering Matrix	4.4	$t = 0.99$	$6.3\,10^{-12}$	0.028
Horizontal Complex Amplitudes Scattering Matrix	4.6	$r = \frac{i}{\sqrt{2}}$; $t = \frac{1}{\sqrt{2}}$	$6.6\,10^{-11}$	0.3
Vertical Complex Amplitudes Scattering Matrix	4.7	$r = 0.99$	$4.3\,10^{-11}$	0.2
Experimental Results (Ref. [26])	2.3	Single Pass	$2.2\,10^{-10}$	1

TABLE III: A summary of final sensitivity results for a double Y and a double semi-X interferometer with comparison to the Stanford interferometer. The fundamental parameters (N_{in}, m *and* r-radius) are similar for all the interferometers

In Table.(III) we present the final sensitivity results for a double Y beamsplitter atom interferometer and for an atom interferometer based on two semi-X beamsplitters. These results are obtained with the parameters $N_{in} = 1.6\,10^{10}\,\frac{atom}{sec}$, $m = 2.2\,10^{-25}\,kg$ and $r = 2.6\,mm$, which are the same as the those given in Ref. [26]. As can be noticed, the best sensitivity, on the order of $\approx 10^{-12}\frac{rad}{sec}/\sqrt{Hz}$, is two orders of magnitude better than the best sensitivity realized so far with a single pass interferometer (also noted in the table). The best sensitivity is achieved in the real amplitude, $t \rightarrow 1$ case, which describes a high finesse double Y interferometer. In such an interferometer the particle has a high probability to complete many cycles inside the interferometer and therefore the accumulated Sagnac phase difference between counterpropagating trajectories is large. The apparent sensitivity difference in the above table between the latter configuration and the vertical complex case, which also describes a high finesse interferometer, could be explained by a crucial difference in the symmetry of each beamsplitter. In the real amplitude case, the inherent symmetry of the Y beam splitters ensures that every clockwise propagating wave has an identical counter clockwise partner, which destructively interferes with it when $\phi = \pi$. On the contrary, in the semi-X configuration, the asymmetry of the beam splitter (as the mirror is on a specific side) means that not all clockwise waves have counter clockwise partners. This gives rise to the fact that the minima of the transmission in the former case goes to zero while in the latter only to half the base height. This factor 2 difference, as well as a difference in the Lorenzian width, give rise to the sensitivity difference observed in the table between the two high finesse configurations.

Finally, our model may be applied to interferometers based on other configurations, if one knows the scattering matrix of the beamsplitter, and so we hope it will serve as a base for designing more advanced interferometer configurations in the future.

5.2. Future work

Much work still needs to be done before all aspects of the problem are accounted for. For example, within the scope of this work one should expand the model to a multi mode system. We have assumed that the motional transverse modes of the waveguide are not

excited due to thermal fluctuations nor scattering effects, i.e the energy gap between the transverse modes is larger than any excitation in the system. This assumption allowed us to treat the system as a single mode system, but a more realistic feasibility study should include coupling between modes.

Furthermore, Atom-Atom interactions and guiding potential impurities may decrease dramatically the sensitivity of a guided interferometer, especially in the high finesse regime (multipass interferometer), due to incoherent scattering. The effect of these phenomena on the interferometer behavior, and in particular on its sensitivity, may be an interesting question for a future theoretical research.

APPENDIX A: BEAM-SPLITTER WITH A COMPLEX S-MATRIX

In order to obtain the scattering matrix of the interferometer setup depicted in Fig.(30), let us examine a few examples in detail. Starting from channel 1, we see that it can only be reflected to channel 2 or transmitted to channel 3. Thus, the scattering matrix elements will be $S_{11} = 0,\ S_{12} = r,\ S_{13} = t$. As another examples let us study the matrix element S_{23}. In order to be transmitted from channel 2 to channel 3 the wave should be first transmitted to the mirror port (with amplitude t) and than be reflected back to channel 3 (with amplitude r) while accumulating some phase $e^{i\delta}$. Thus, the resulting matrix element is $S_{23} = rte^{i\delta}$. Following the above procedure for all channels one obtains the S-matrix of Eq.(3.23)

APPENDIX B: STS DERIVATION

In T. L. Gustavson's thesis [26] the STS is given by

$$\Delta\Omega = \chi^{-1}\frac{1}{vk_{eff}\tau^2}, \tag{B.1}$$

where v is the longitudinal velocity, K_{eff} is the additional momentum kick due to the $\frac{\pi}{2}$ pulse and τ is the time between the pulses. In the following we show that Eq.(B.1) is analogous to Eq.(3.29).

The peak-to-peak interference fringe signal as shown in Fig.(59) is

$$S_{pp} = N_{max} - N_{min}\ , \tag{B.2}$$

while the noise in a shot-noise limited system is poissonian. Since we are interested in the sensitivity for small rotation rates, the noise near $\Omega = 0$ is given by

$$N_{oise} = \sqrt{N_{(\Omega=0)}} \ . \tag{B.3}$$

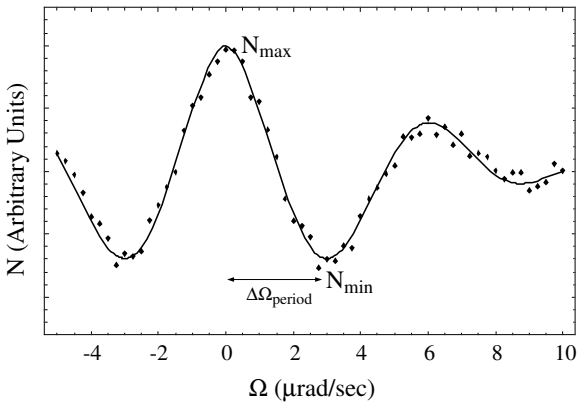

FIG. 59: An example of a typical signal of an atom interferometer rotation measurement (computer generated)

The signal to noise ratio is given by

$$\chi = \frac{S_{pp}}{\sqrt{N_(\Omega = 0)}} \ . \tag{B.4}$$

In order to detect a differences in the signal, we demand that changes in the signal due to rotations will be at least from the same magnitude of the noise

$$\frac{\Delta N}{\Delta \Omega} \Delta \Omega \geq \sqrt{N_{(\Omega=0)}} \ , \tag{B.5}$$

and rearranging we get

$$\Delta \Omega = \frac{\sqrt{N_{(\Omega=0)}}}{\frac{dN}{d\Omega}}. \tag{B.6}$$

The effective flux ϕ has a 2π periodicity, therefore Ω has a $\frac{\pi\hbar}{mA}$ periodicity (recalling that

$\phi = \frac{2mA}{\hbar}\Omega$), and the peak-to-peak distance is given by

$$\Delta\Omega_{period} = \frac{\pi\hbar}{2mA}. \tag{B.7}$$

For a smoothly varying function, such as cosine in Gustavson's experiment, a good approximation for $\frac{dN}{d\Omega}$ is given by

$$\frac{dN}{d\Omega} \approx \frac{N_{max} - N_{min}}{\Delta\Omega_{period.}} \tag{B.8}$$

By substitute of Eq.(B.4) and Eq.(B.8) into Eq.(B.6) we obtain

$$\Delta\Omega = \chi^{-1}\Delta\Omega_{period} \ . \tag{B.9}$$

Recall Eq.(B.1) we can manipulate its second term,

$$\frac{1}{vk_{eff}\tau^2} = \frac{v}{v^2k_{eff}\tau^2}. \tag{B.10}$$

The product $L = v\tau$ is the geometrical distance between two pulses, i.e. half of the interferometer length, thus Eq.(B.10) becomes

$$\frac{1}{vk_{eff}\tau^2} = \frac{v}{L^2k_{eff}} = \frac{\hbar}{mL^2}\frac{k}{k_{eff}} \ , \tag{B.11}$$

where $\hbar$ is Planck constant, m is the particle mass and k is the longitudinal momentum. From the ratio between the transversal momentum and the longitudinal momentum, one can obtain $\tan(\theta)$, where θ is the angle between the arms of the interferometer, and calculate its area,

$$\frac{\hbar}{mL^2}\frac{k}{k_{eff}} = \frac{\hbar}{mL^2}\frac{1}{\tan(\theta)} = \frac{\hbar}{mA} \ . \tag{B.12}$$

From Eq.(B.12) we can notice that Eq.(B.1) and Eq.(B.9) are equal up to a constant factor

≈ 1.5.

APPENDIX C: TEMPERATURE LIMIT

The classical relation between velocity and temperature τ, (in one dimension) is given by

$$\frac{1}{2}mv^2 = \frac{1}{2}K_B\tau \Rightarrow \Delta v = \sqrt{\frac{K_B\Delta\tau}{m}}\ , \tag{C.1}$$

and in terms of momemtum we obtain

$$\Delta k = \sqrt{\frac{mK_B\Delta\tau}{\hbar^2}}\ . \tag{C.2}$$

From Eq.(4.2) one can see that momentum fluctuations yield peak drifts and from the demand that this drift will be narrower than the peak width we obtain (under the $t \approx 1$ approx.)

$$\Delta kL < 4(1-t) \tag{C.3}$$

By Substitution of Eq.(C.2) we obtain

$$\sqrt{\frac{mK_B\Delta\tau}{\hbar^2}} < \frac{4(1-t)}{L} \Rightarrow \Delta\tau < \frac{16\hbar^2(1-t)^2}{mK_BL^2}\ . \tag{C.4}$$

For Cs Atom moving in interferometer with radius of $2.6\,10^{-3}\,m$ and $t = 0.99$ the needed temperature is from the order of $\approx 10^{-20}K$ which is far below a feasible temperature.

APPENDIX D: INTEGRATION AT THE $t \ll 1$ - WIDE BAND REGIME

Let us simplify the integral

$$N_{out} \;=\; N_{in} \int_{-\infty}^{\infty} dk \; I_{in}(k) \; T(k,\phi) \; , \tag{D.1}$$

in few steps:

For $\phi = 0$ the transmission curve has a Lorentzian shaped resonances as plotted (for $t = 0.1$) in Fig.(60) and Eq.(4.1) is given by

$$T_{(\phi=0)} = \frac{4 \sin \frac{kL}{2}^2}{\left(\frac{1-2t+2t^2}{2t(1-t)}\right)^2 (1-\cos\left[kL\right])^2 + \sin^2\left[kL\right]} \; . \tag{D.2}$$

Using trigonometric identities and algebric manipulations we obtain

$$T_{(\phi=0)} = \frac{1}{\left(\left(\frac{1-2t+2t^2}{2t(1-t)}\right)^2 - 1\right)} \frac{1}{sin^2[\frac{kL}{2}] + \frac{1}{\left(\left(\frac{1-2t+2t^2}{2t(1-t)}\right)^2 - 1\right)}}. \tag{D.3}$$

A Taylor expantion around $k = \frac{n\pi}{L}$ will obtain

$$\begin{aligned} T_{(\phi=0)} \;&\approx\; \frac{4}{L^2 \left(\left(\frac{1-2t+2t^2}{2t(1-t)}\right)^2 - 1\right)} \sum_{n=-\infty}^{\infty} \frac{1}{\left(k - \frac{2n\pi}{L}\right)^2 + \frac{4}{\left(\left(\frac{1-2t+2t^2}{2t(1-t)}\right)^2 - 1\right)}} \\ &=\; \frac{\Delta_T \, L \sinh[\Delta_T \, L]}{2\cosh[\Delta_T \, L] - 2\cos[kL]} \; , \end{aligned} \tag{D.4}$$

where

$$\Delta_T = \frac{4t(1-t)}{L(1-2t)}. \tag{D.5}$$

The approximation given in Eq.(D.4) is plotted in Fig.(60).

For $\phi \neq 0$, the maximal transmission is getting smaller then 1 between $0 < \phi \leq \pi$ and

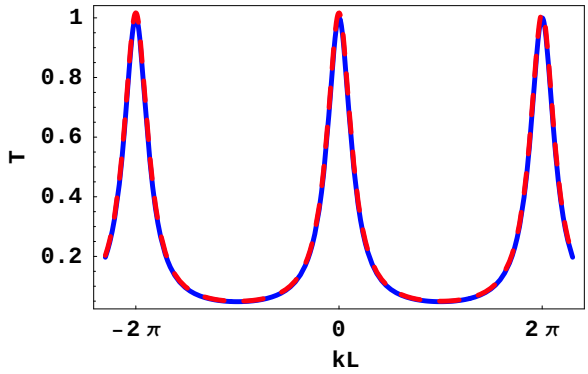

FIG. 60: Interferometer transmission for $\phi = 0$ and $t = 0.1$. The red dashed line is the approximated transmission given in Eq.(D.4)

viceversa between $\pi < \phi \leq 2\pi$. The transmission curve is not simply a Lorentzian, but it has a Lorentzian envelope curve, as seen in Fig.(61). The envelope curve is given by

$$L_1 = \frac{\cos^2[\frac{\phi}{2}]}{\left(\left(\frac{1-2t+t^2}{2t(1-t)}\right)^2 - 1\right)\sin^2[\frac{kL}{2}] + \left(1 - \frac{2t^2(1-2t+2t^2)}{(2t(1-t))^2}\sin^2[\frac{\phi}{2}]\right)}. \tag{D.6}$$

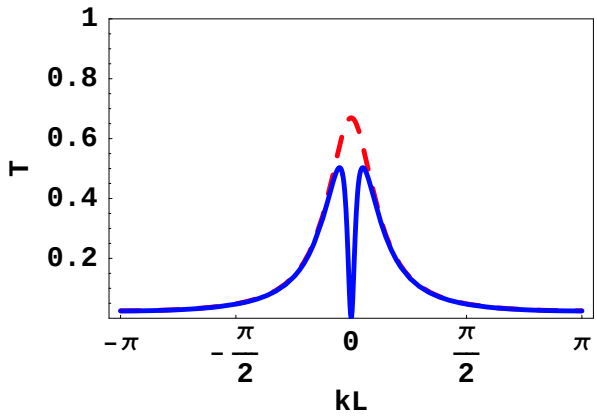

FIG. 61: Interferometer transmission for $\phi = \frac{\pi}{2}$ and $t = 0.1$. The red dashed line is the envelope of the transmission curve, L_1

A Taylor expantion around $k = \frac{n\pi}{L}$ will obtain

$$L_1 \approx a_1 \sum_{-\infty}^{\infty} \frac{\Delta_1^2}{(k - \frac{n\pi}{L})^2 + \Delta_1^2} = a_1 \frac{\Delta_1 L \sinh[\Delta_1 L]}{2\cosh[\Delta_1 L] - 2\cos[kL]}, \tag{D.7}$$

where

$$a_1 = \frac{\cos^2[\frac{\phi}{2}]}{1 - \frac{1-2t+2t^2}{2(1-t)^2}\sin^2[\frac{\phi}{2}]} \quad ; \quad \Delta_1 = \sqrt{\frac{1 - \frac{1-2t+2t^2}{2(1-t)^2}\sin^2[\frac{\phi}{2}]}{L^2\left(\left(\frac{1-2t+2t^2}{4t(1-t)}\right)^2 - \frac{1}{2}\right)}} \tag{D.8}$$

Denote by L_2 the subtraction of the transmission, T from the envelope curve, L_1 we obtain

$$L_2 = \frac{t^2\cos^2[\frac{\phi}{2}]}{4(1-t)^2\left(\left(\frac{1}{\sin^4[\frac{\phi}{2}]} - \frac{t^2}{4(1-t)^2}\right)\sin^2[\frac{kL}{2}] + \frac{t^2}{4(1-t)^2}\left(1 - \frac{(1-2t+2t^2)\sin^2[\frac{\phi}{2}]}{2(1-t)^2}\right)\right)}, \tag{D.9}$$

A Taylor expantion around $k = \frac{n\pi}{L}$ will obtain

$$L_2 \approx a_2\sum_{-\infty}^{\infty}\frac{\Delta_2^2}{(k-\frac{n\pi}{L})^2 + \Delta_2^2} = a_2\frac{\Delta_2 L\sinh[\Delta_2 L]}{2\cosh[\Delta_2 L] - 2\cos[kL]}, \tag{D.10}$$

where

$$a_2 = a_1 \quad ; \quad \Delta_2 = \sqrt{\frac{t^2\left(1 - \frac{1-2t+2t^2}{2(1-t)^2}\sin^2[\frac{\phi}{2}]\right)}{L^2(1-t)^2\left(\frac{1}{\sin^4[\frac{\phi}{2}]} - \frac{t^2}{4(1-t)^2}\right)}}. \tag{D.11}$$

Now we can express the transmission in terms of L_1 and L_2

$$T(k,\phi) \approx a1\left(\sum_{-\infty}^{\infty}\frac{\Delta_1^2}{(k-\frac{n\pi}{L})^2 + \Delta_1^2} - \sum_{-\infty}^{\infty}\frac{\Delta_2^2}{(k-\frac{n\pi}{L})^2 + \Delta_2^2}\right) = \sum_{-\infty}^{\infty}T_n(k,\phi)\ , \tag{D.12}$$

as shown in Fig.(62). Substituting Eq.(D.12) into Eq.(D.1) we obtain

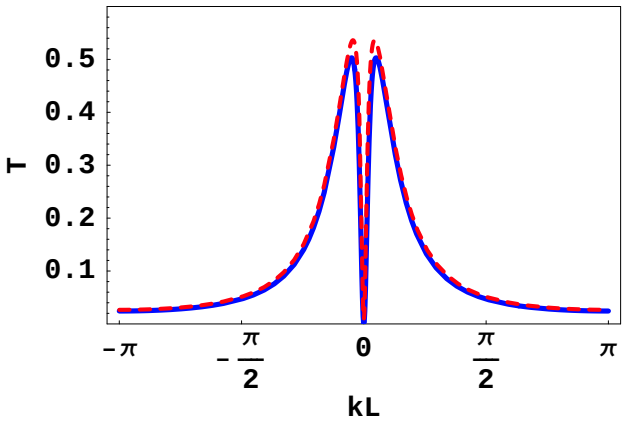

FIG. 62: Interferometer transmission for $\phi = \frac{\pi}{2}$ and $t = 0.1$. The red dashed line is the function subtraction $L_1 - L_2$

$$N_{out} \approx N_{in} \sum_{n=-\infty}^{\infty} \int_{-\infty}^{\infty} dk\ I_{in}(k)\ T_n(k,\phi)\ , \tag{D.13}$$

Since at this regime the width of the momentum distribution $\Delta_k \gg \frac{2\pi}{L}$ and $T_n(k)$ has a periodicity of $\frac{2\pi}{L}$, Eq.(D.13) becomes

$$N_{out} \approx N_{in} \sum_{n=-\infty}^{\infty} I_{in}(\frac{2n\pi}{L}) \int_{-\frac{\pi}{L}}^{\frac{\pi}{L}} dk\ T_0(k,\phi)\ . \tag{D.14}$$

Generally, the integral of a Lorentzian function over 2π period and Lorentzian width much smaller then π, converges into

$$\lim_{\Delta \ll \pi} \int_{-\pi}^{\pi} \frac{\Delta^2}{k^2 + \Delta^2} dk = \lim_{\Delta \ll \pi} 2\Delta \arctan[\frac{\pi}{\Delta}] \approx \pi\Delta\ . \tag{D.15}$$

Specificlly, $\Delta_{1,2} \lessapprox t\frac{\pi}{L}$, therefore for $t \ll 1$, N_{out} could be approximated by

$$N_{out} \approx N_{in} a_1 \pi(\Delta_1 - \Delta_2) \sum_{n=-\infty}^{\infty} I_{in}(\frac{2n\pi}{L})\ . \tag{D.16}$$

The sum $\sum_{n=-\infty}^{\infty} I_{in}(\frac{2n\pi}{L})$ could be converted ($\frac{2\pi}{L} \ll \Delta k$) into the integral $\frac{L}{2\pi}\int_{-\infty}^{\infty} G(x)dx$, where $G(x)$ is a normalized Gaussian, and finally N_{out} could by approximated by

$$N_{out} \approx N_{in} a_1 \pi(\Delta_1 - \Delta_2)\frac{L}{2\pi} = N_{in} a_1 \pi(\Delta_1 - \Delta_2) r \ . \tag{D.17}$$

[1] D.E. Pritchard *et al*, Phys. Rev. Lett. **66**, 2693 (1991).

[2] O. Carnal and J. Mlynek, Phys. Rev. Lett. **66**, 2689 (1991).

[3] M.A. Kasevich and S. Chu, Phys. Rev. Lett. **67**, 181 (1991).

[4] C.J. Borde *et al*, Phys. Rev. Lett. **67**, 177 (1991).

[5] K. Bongs *et al*, Phys. Rev. Lett. **83**, 3577 (1999).

[6] W. Ketterle *et al*, Phys. Rev. Lett. **92**, 050405 (2004).

[7] T. Schumm, S. Hofferberh, L.M. Andersson, S. Wildermuth, S. Groth, I. Bar-Joseph, J. Schmiedmayer, and P. Krüger, Nature **1**, 57 (2005).

[8] For a comprehensive review see, e.g., M. O Scully and M. S. Zubairy, *Quantum Optics*. Cambridge University Press (1997).

[9] G. B. Malykin, Phys. Usp. **43**, 1229 (2000).

[10] P. Storey and C. Cohen-Tannoudji, Journal de Physique II 4, 1999 (1994)

[11] R. Folman, P. Krüger, J. Schmiedmayer, J. Denschlag, and C. Henkel, Adv. At. Mol. Phys **48**, 263 (2002).

[12] P. Krüger, X. Luo, M.W. Klein, K. Bruger, A. Haase, S. Wildermuth, S. Groth, I. Bar-Joseph, R. Folman, and J. Schmiedmayer, Phys. Rev. Lett. **91**, 233201 (2003).

[13] R. Folman, P. Krüger, D. Cassettari, B. Hessmo, T. Maier and J. Schmiedmayer, Phys. Rev. Lett. **84**, 4749 (2000).

[14] D. Cassettari, B. Hessmo, R. Folman, T. Maier, and J. Schmiedmayer, Phys. Rev. Lett. **85**, 5483 (2000).

[15] G. Birkl, F.B.J. Buchkremer, R. Dumke and W. Ertmer, Opt. Com. **191**, 67 (2001).

[16] T. Müther, J. Nes, A. L. Gehrmann, M. Volk, W. Ertmer, G. Birkl, M. Gruber and J. Jahns, J. Phys.: Conf. ser **19**, 97 (2005).

[17] T. Fernholtz, R.Gerritsma, P. Kruger, and R.J.C. Spreeuw, arXiv: physics/0512017, unpublished.

[18] S. Gupta, K.W. Murch, K.L. Moore, T.P. Purdy, and D.M. Stamper-Kurn, Phys. Rev. Lett. **95**, 143201 (2005).

[19] O. Morizot, Y. Colombe, V. Lorent, B.M. Garraway and H. Perrin, arXiv: Physics/0512015, unpublished.

[20] Ph.W. Courteille, B. Deh, J. Fortágh, A. Günther, S. Kraft, C. Marzok, S. Slama, and C. Zimmermann, J. Phys. B. **39**, 1055 (2006)

[21] C. S. Garvie, E. Riis, and A. S. Arnold, Quant. El. Conf., p. 173-174 (2004)

[22] A. S. Arnold, C. S. Garvie, and E. Riis, Phys. Rev. A, 041606 (2006)

[23] Pritchard D. E., Phys. Rev. Lett. **51**, 1336 (1983).

[24] T.L. Gustavson, ,P. Bouyer, and M.A. Kasevich, Phys. Rev. Lett. **78**, 2046 (1997).

[25] T.L. Gustavson, ,A. Landragin, and M.A. Kasevich, Class. Quant. Grav. **17**, 2385 (2000).

[26] T.L. Gustavson, Ph.D. thesis, Stanford University (2000).

[27] C.J. Borde, Metrologia **39**, 435-463 (2002)

[28] Group webpage http://lne-syrte.obspm.fr/capteurs_ inertiels/index2.htm

[29] Group webpage: http://www.iqo.uni-hannover.de/ertmer/casiindex/

[30] J. J. Sakurai, Phys. Rev. D. **21**, 2993 (1980).

[31] Y. Aharonov and D. Bohm, Phys. Rev. **115**, 485 (1959).

[32] For a comprehensive review see, e.g., S. Datta, *Electronic Transport in Mesoscopic Systems*. Cambridge University Press (1995).

[33] M. Moskalets, and M. Büttiker, Phys. Rev. B. **68**, 161311 (2003)

[34] *Quantum Transport in Mesoscopic Systems*, P. A. Mello and N. Kumar, pp. 181, Oxford University Press (2004)

[35] *Atom Interferometry*, edited by P. R. Berman, Academic Press (1997)